2018

Solution phase synthesis and computational investigation of pnictide based Nowotny-Juza phases

Miles Arthur Burris White
Iowa State University

Solution phase synthesis and computational investigation of pnictide based Nowotny-Juza phases

by

Miles A. B. White

A dissertation submitted to the graduate faculty

in partial fulfillment of the requirements for the degree of

DOCTOR OF PHILOSOPHY

Major: Inorganic Chemistry

Program of Study Committee:
Javier Vela, Co-major Professor
Gordon Miller, Co-major Professor
Emily Smith
James Evans
Julia Zaikina

The student author, whose presentation of the scholarship herein was approved by the program of study committee, is solely responsible for the content of this dissertation. The Graduate College will ensure this dissertation is globally accessible and will not permit alterations after a degree is conferred.

Iowa State University

Ames, Iowa

2018

TABLE OF CONTENTS

NOMENCLATURE

PXRD	Powder X-Ray Diffraction
TEM	Transmission Electron Microscopy
XPS	X-ray Photoelectron Spectroscopy
EDX	Energy Dispersive X-ray Spectroscopy
TOP	Tri-n-octylphosphine
WANDA	Workstation for Automated Nanomaterials Discovery and Analysis
ssNMR	Solid-State Nuclear Magnetic Resonance

ACKNOWLEDGMENTS

I am extremely appreciative of the great network of friends, family, and colleagues who have made the completion of this thesis possible. Although having two major professors seemed like an odd concept when joining Iowa State four years ago, it is hard to imagine how differently my time here would have been without the guidance of both Javier Vela and Gordie Miller. Along with the plethora of technical skills that they have both instilled, I was able to observe two distinct mentoring styles which I hope I can make great use of in future endeavors.

I would like to thank Javier for always being extremely optimistic about grants, awards, publications, etc. There are countless accomplishments/recognitions that I would not be able to claim without him. Additionally, he has always pushed me to be the best researcher possible and always keeps his group's best interests at heart. I would like to thank Gordie for always providing great advice and frequently causing me to reassess the ways that I think about experimental and computation chemistry. Along with my research advisors, I would like to thank Joe Burnett who served as my Preparing Future Faculty mentor. Joe has been an invaluable resource for learning about pedagogy and receiving feedback about my teaching. In addition, I would like to thank the rest of my committee members both past and present, Professors Jim Evans, Wenyu Huang, Emily Smith, and Julia Zaikina, for their insights and guidance.

The Vela and Miller groups have been incredibly encouraging and supportive throughout my time in graduate school. I would like to thank Michelle Thompson who, along with being a fantastic friend, got me started in the lab. I would also like to thank Bryan Rosales for many enjoyable conversations about science, research, and life.

Furthermore, I would like to thank Alan Medina-Gonzalez for doing a painful amount of PXRD during our trip to the Molecular Foundry. Thank you to Himashi Andaraarachchi and Long Men who were fantastic senior lab mates that were always available to help. Many thanks to the current Vela group members; Carena Daniels, Lin Wei, Marquix Adamson, Yunhua Chen, and Phil Yox for being such great lab mates and colleagues. I am optimistic for the future of the group and excited to see how it develops in the years to come. Along with graduate students, I have been extremely fortunate to have worked with Kate Baumler who is an astounding undergraduate researcher. Chapter 4 of this thesis would not be possible without her contributions. I have learned a considerable amount from training her in the lab and am grateful for the mentoring experience.

Outside of the lab, I have been blessed with amazing friends to commiserate the struggles of graduate school. First, I would like to thank Kyle Woolcock for his help with various coding problems that are far below his pay grade and for his continued friendship. I would like to thank Brad Schmidt for coffee breaks, lunches, and general good companionship and conversations throughout graduate school. I would also like to thank Zak Weinstein for introducing me to the group of Dave Appy, Mark Juetten, Josh Peterson, Frank Qiu, Marcelino Varona-Ortiz, Kris Miller, and others to participate in activities outside the lab which has made my time here far more enjoyable. Additionally, I would like to thank Paige Hinners and Yan Yun Chu for not only being great friends to me, but also Mary.

Most importantly, I would like to thank Mary for constant encouragement, love, and support over the past four years. There are no words that do justice to her importance in this accomplishment. I truly couldn't have done this without her.

ABSTRACT

Filled tetrahedral semiconductors comprised of elements from group I, II, and V of the periodic table are of interest to the thermoelectric, photovoltaic, and battery fields due to their tunable electronic structures. However, until recently, the synthesis of these materials in a facile and scalable manner had remained elusive. In this thesis, we demonstrate the solution phase synthesis of three members of this class of compounds (LiZnP, LiCdP, and LiZnSb). Furthermore, we explore the presence of polytypism in these compounds and computationally investigate which additional phases would be expected to display polytypism. Finally, we closely investigate the phase space of Li-Zn-Sb made in solution to determine the relevant factors for phase and polytype selectivity.

We begin by demonstrating the first solution phase synthesis of a I-II-V semiconductor by utilizing lithium hydride, diethylzinc, and tri-*n*-octylphosphine as precursors to synthesize LiZnP. We generalized this synthesis to be successful with multiple Li (lithiumdiisopropylamide, phenyllithium, *n*-butyllithium, and lithium hydride), Zn (zinc stearate, zinc chloride, and diethylzinc), and P (triphenylphosphine and tri-*n*-octylposphine) precursors as well as substituting Cd for Zn by utilizing dimethylcadmium. Additionally, we were able to determine the mechanism of formation of these nanocrystals which agreed with prior literature reports for binary phosphides.

Following which, we further extended this synthetic method to yield LiZnSb in solution. Interestingly, despite all prior literature reports showing LiZnSb crystallizing in the hexagonal LiGaGe-type, LiZnSb prepared in solution was found to crystalline in the cubic MgAgAs-type. This report was the first example of polytypism within the ternary filled tetrahedral semiconductors. Given the promising thermoelectric properties of

hexagonal LiZnSb, we calculated transport properties and found cubic LiZnSb to be comparable to its hexagonal polytype but with the advantage of having high figure of merit in both *p* and *n*-type variants.

With the surprising observation of polytypism within LiZnSb, we sought to better map out the phase space of Li-Zn-Sb to see if we could selectively target both hexagonal and cubic LiZnSb. We utilized a high throughput synthetic robot to screen the effects of precursor concentration, injection order, nucleation and growth temperatures, and reaction time on reaction products. Surprisingly, we found another previously unreported ternary phase which adopts a variant of the hexagonal LiGaGe-type. Additionally, we were able to obtain 6 unique crystalline products dependent on the reaction parameters used.

The results of this work will open the door for increased application of I-II-V semiconductors. By synthesizing these phases in solution, their utility in thermoelectric devices is enhanced through a reduction in grain size and subsequent suppression of thermal conductivity. Furthermore, synthesizing these compounds by low temperature solution phase techniques significantly decreases the barrier for large-scale implementation. From a more fundamental perspective, the discovery of polytypism within this family of compounds offers a rich frontier to explore from a crystallographic perspective.

CHAPTER 1

INTRODUCTION

Sections adapted and reprinted with permission from *Chemistry – A European Journal*, **2017**, *24*, 3650-3658.

Miles A. White, Alan M. Medina-Gonzalez, and Javier Vela

General Introduction

This thesis describes the synthesis, characterization, and computational investigation of phases primarily belonging to the I-II-V family of filled tetrahedral semiconductors prepared through solution phase methods. This work reports the development of a synthesis for LiZnP that then is able to be generalized for other I-II-V semiconductors. This synthesis was then extended to LiZnSb which was found to adopt a previously unknown polytype. In light of this result, we systematically investigated the Li-Zn-Sb phase space to see the relevant reaction parameters for phase selectivity.

Filled Tetrahedral Semiconductors

Tetrahedral coordination is ubiquitous among crystalline materials, and many familiar inorganic semiconductors adopt the cubic zinc-blende/diamondoid (zb/d: II-VI, III-V, IV) or hexagonal wurtzite (w: II-VI, III-V) structure. Because the packing efficiency of these structures is less than half of that for hexagonal close-packing (hcp) (34% vs. 74% for perfect hcp),[1] they may fill in with extra atoms, creating a more close-packed network.

The addition of extra atoms to tetrahedral semiconductors gives rise to many unique filling patterns. For example, the zinc-blende unit cell has eight tetrahedral holes split between two Wyckoff positions. Filling one of these positions gives the half-Heusler, MgAgAs

structure type (Figure 1). Similarly stuffing of the wurtzite lattice gives the LiGaGe structure type, an ordered variant of the $CaIn_2$ structure.[2] A stuffed wurtzite lattice may flatten to form hexagonal sheets, generating the ZrBeSi-type structure. In total, over 40 filled tetrahedral semiconductor structures are known.[3] Interestingly, as with zinc-blende/wurtzite polytypism,[4] filled tetrahedral semiconductors are also expected to display polytypism, because the energy differences between possible structures are small.[5]

One way to rationalize bonding and electronic structure in filled tetrahedral semiconductors is to look at the commonly adopted half-Heusler prototype (a similar analysis could be made for any of the available crystal structures). Half-Heusler compounds have the general composition XYZ. Elements X and Z are the more electropositive and electronegative elements, respectively. Elements Y and Z make up a zinc-blende lattice. Element X fills or 'stuffs' this lattice to make a rock salt lattice with Y (Figure 1, MgAgAs-type).

Semiconducting half-Heusler compounds have valence electron counts that completely fill their valence shell with either 8 or 18 electrons.[6,7] For instance, half-Heusler compounds comprised of group I (X), III (Y), and IV (Z) elements closely resemble the elemental semiconductors such as silicon, featuring donation of s electrons from the group I element to the group III element.[8] This renders the group III fragment isoelectronic with group IV elements, whose ability to form covalent sp^3 bonds is responsible for the chemically robust zinc-blende $(III\text{-}IV)^-$ network.[8] This behavior is the basis for the high stability and semiconducting properties of 8 and 18 electron half-Heusler phases. Moving beyond 8 or 18 valence electrons results in a decrease in stability, due to the population of antibonding states. Nevertheless, one can still synthesize such compounds, which behave as half metals having

magnetic moments equal to the excess electron count.[9,10] For instance, 18 electron TiCoSb is semiconducting, while 20 electron CrCoSb is metallic with a magnetic moment of ~ 2 μ_B.[11]

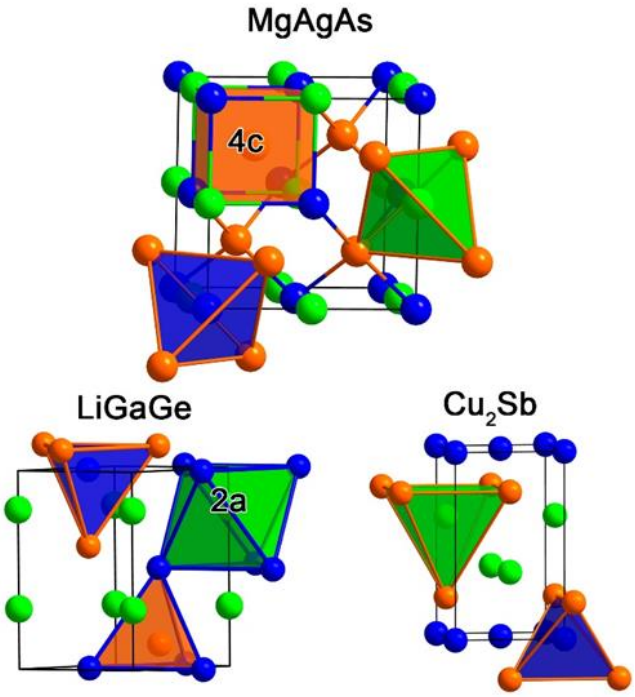

Figure 1. Crystal structure of three possible polytypes of filled tetrahedral semiconductors XYZ. Local coordination environment is shown using polyhedra to highlight the tetrahedral framework. Most common Wyckoff site preference is shown with X (green), Y (blue), and Z (orange).

Because states located around the Fermi level are comprised of a sp^3 network, the band gap of filled tetrahedral semiconductors can be tuned by changing the relative electronegativities of the elements making up the tetrahedral network.[12] In the case of I-II-V variants (Figure 2), calculations on both cubic and hexagonal polytypes show that band gaps narrow as the electronegativity differences between II and V elements decrease.[7] This trend is observed in both Li- and Na-based analogues. Specific band gap values are smaller for the larger Na cation, but the overall trend remains.

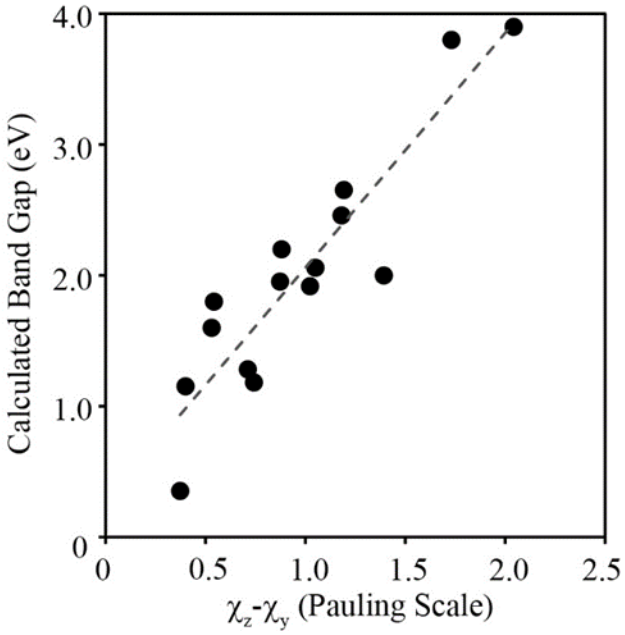

Figure 2. Band gap versus electronegativity difference for Li-based I-II-V eight electron filled tetrahedral semiconductors calculated using the TB-mBJ potential.

Lithium-Based Nowotny-Juza Phases

Nowotny-Juza compounds are filled tetrahedral semiconductors consisting of elements from groups I, II, and V (*e.g.*, LiZnP), where the stuffing atom is typically the most electropositive alkali metal.[13-15] The electronic structure of these compounds closely mimics that of classic binary semiconductors (IV-IV, III-V, or II-VI), with a tetrahedral $(II\text{-}V)^-$ network that is charge balanced with a stuffed I^+ monovalent cation. As mentioned above, tuning the electronegativity difference of the constituent elements in the tetrahedral framework allows one to control the band gap of these compounds (Figure 2).[12] However, due to the interstitial insertion rule,[16-18] these compounds have direct band gaps, which improves their functionality.

Li-based Nowotny-Juza phases typically adopt either the cubic MgAgAs-type or hexagonal LiGaGe-type crystal structures (Figure 1), which are most closely related to the zinc-blende and wurtzite frameworks, respectively. LiZnP is a particular interesting compound

due to its suggested application in thermoelectrics,[20] photovoltaics,[21,22] Li-ion batteries,[23] and as a neutron detector.[24] The band gap and lattice constant of LiZnP are in good agreement with CdS, making the former an ideal low toxicity substitute for the latter.[12] Aside from LiZnP, hexagonal LiGaGe-type LiZnSb was predicted to be a promising thermoelectric material.[35] Lightly doped *n*-type LiZnSb was calculated to have a zT of ~ 2 at 600 K. As such, attempts were made to synthesize *n*-type LiZnSb.[36] Nevertheless, all syntheses resulted in unintentionally *p*-type LiZnSb with minimal thermoelectric performance. Interestingly, the transport properties measured on *p*-type LiZnSb were in good agreement with calculation.

Polytypism and Coloring in the Nowotny-Juza Phases

The different reported crystal structures between LiZnP (cubic MgAgAs-type) and LiZnSb (hexagonal LiGaGe-type) highlights the possibility of different polytypes. Additionally, it is critical to consider the potential for alternative site preference (also referred to as coloring pattern),[5,37,38] compared to other similar phases.

Because structure strongly influences properties, both the specific polytype and coloring preference are extremely important in determining the utility of a particular phase. Fortunately, relatively simple *ab initio* calculations can correctly predict the preferred coloring patterns and lattice constants.[39] For instance, a low level treatment of exchange and correlation using the Perdew-Burke-Ernzerhof (PBE) and local density approximation (LDA) yield results that agree well with available experimental data.[40] Furthermore, accurate band gaps can then be calculated using the Tran-Blaha-modified Becke-Johnson (TB-mBJ) potential, which works quite well for these phases.[41-43] When analyzing I-II-V Nowotny-Juza phases (such as LiZnSb), both methods (PBE or LDA) correctly predict the preferred polytype and respective coloring pattern.

When considering the lowest energy structure for filled-tetrahedral phases, it is essential to consider not only the structure but also every possible coloring pattern. While a thorough analysis would require an immense amount of computational time, identifying common trends in site preferences can expedite the scanning of possible crystal structures. Here again, the half-Heusler (MgAgAs-type) serves as a good prototype because it is the most comprehensively studied among dozens of commonly adopted structure types.[44]

Within the MgAgAs crystal structure, there are multiple common structural motifs consistent with conflicting types of bonding. Using the XYZ notation discussed earlier, a highly ionic rock salt packing pattern is observed between X and Y atoms. Meanwhile, each of the XZ and YZ pairs form covalent zinc-blende frameworks. As such, there exist competing ionic and covalent interactions which dictate the correct coloring pattern. Elements X and Y are related by a translational shift of half a unit cell and, therefore, switching the elements occupying these positions has no impact on the total energy (*i.e.*, the total energy of XYZ with X, Y, and Z being Li, Zn, and P is equivalent to them being Zn, Li, and P, respectively). This simplifies scanning possible coloring patterns, because the relevant parameter for correct coloring is given by the identity of the element occupying the heterocubic Z site.

A recent bonding analysis in MgAgAs-type compounds analysed the difference between phases composed of either two early main group elements (AA') or two transition metals (TT') and one late main group element (E) (*e.g.*, LiMgP *vs.* TiNiSn).[45] In the AA'E compositions, E was found to always occupy the heterocubic site, whereas in the TT'E compositions, T' was found to occupy the heterocubic site. This is explained by the covalent interaction dominating when electronegativity differences are small, and ionic interactions dominating when the electronegativity differences are large.

Building off this observation, we found a change in 4c site occupancy preference for 8 electron phases containing high electronegativity elements such as those from group XI and XII. Table 1 includes calculations on all experimentally reported Nowotny-Juza phases in the ICSD.[65] As expected, the metal starts to occupy the heterocubic site in the LiZnPn family as the electronegativity difference between Zn and the pnictide becomes small (where Zn actually prefers the heterocubic site for LiZnSb and LiZnBi).[5] Additionally, when the monovalent cation is comprised of the coinage metals, these metals prefer the heterocubic site due to their extremely high electronegativity.

The impact that this minor change has on the properties of these materials is quite dramatic. For instance, in LiZnSb, the lattice parameter can change as much 0.21 Å. Furthermore, the heterocubic atom is a large portion of the states located directly around the Fermi level (conduction band minimum and valence band maximum) which are responsible for the nature and size of the bandgap. The change in 4c site occupancy from the anticipated Sb to the observed Zn results in a change in band gap from a direct band gap of 1.3 eV to an indirect band gap of 1.2 eV. Additionally, the bands change shape which significantly alters the transport properties. Ultimately, this results in over double the calculated zT for the observed solution phase polytype with Zn occupying the heterocubic site.[5]

Moving away from the cubic MgAgAs-type, the relevant coloring site will change but the competing ionic and covalent interactions remain. For instance, in the hexagonal LiGaGe-type, the two elements making up the wurtzite lattice are symmetry equivalent and will generally be the two elements with most similar electronegativity. As such, the element that stuffs into the lattice is the most electropositive element which favors the more ionic type interactions (*i.e.*, Li in LiGaGe).

Table 1. Coloring preference and calculated lattice constant for cubic Nowotny-Juza phases reported in the International Crystal Structure Database (ICSD).[65] The bolded element corresponds to the element occupying the 4c site that is lowest in energy.

Phase	4c occupancy	ΔE (meV/atom)	a_{exp} (Å)	A_{calc} (Å)	Phase	4c occupancy	ΔE (meV/atom)	a_{exp} (Å)	a_{calc} (Å)
LiZn**N**	Li	840.6	4.88	4.79	LiMg**Bi**	Li	146.5	6.74	6.39
	Zn	534.1		4.88		Mg	151.0		6.67
	N	**0**		4.80		**Bi**	**0**		**6.69**
LiZn**P**	Li	449.0	5.78	5.50	LiCd**P**	Li	326.8	6.09	5.79
	Zn	10.9		5.58		Cd	185.7		5.99
	P	**0**		5.61		**P**	**0**		**5.98**
LiZn**As**	Li	359.8	5.94	5.67	LiCd**As**	Li	257.8	6.26	5.95
	Zn	6.6		5.77		Cd	136.9		6.17
	As	**0**		**5.81**		**As**	**0**		**6.17**
Li**Zn**Sb	Li	225.3	6.23	6.02	**Cu**ZnAs	**Cu**	**0**	5.87	**5.68**
	Zn	**0**		**6.14**		Zn	177.4		5.73
	Sb	36.4		6.23		As	77.7		5.75
Li**Zn**Bi	Li	203.4	N/A	6.19	**Cu**MgSb	**Cu**	**0**	6.17	**6.09**
	Zn	**0**		**6.34**		Mg	471.0		6.27
	Bi	57.1		6.41		Sb	227.2		6.28
LiMg**N**	Li	686.1	4.97	4.75	**Cu**MgBi	**Cu**	**0**	6.27	**6.26**
	Mg	707.6		4.94		Mg	402.8		6.41
	N	**0**		**4.89**		Bi	257.4		6.45
LiMg**P**	Li	325.2	6.02	5.66	**Au**CaBi	**Au**	**0**	6.85	**6.77**
	Mg	340.4		5.92		Ca	559.2		6.88
	P	**0**		**5.90**		Bi	282.9		6.84
LiMg**As**	Li	287.3	6.19	5.84	AgZn**As**	Ag	42.5	5.91	6.02
	Mg	292.6		6.08		Zn	6.7		5.98
	As	**0**		**6.07**		**As**	**0**		**6.04**

ΔE is given as the difference in energy relative to the lowest energy coloring pattern. Calculations were performed using local density approximation as implemented in the Vienna Ab Initio Simulation Package (VASP). LDA has been shown to correctly predict the observed coloring pattern but generally underestimates the lattice constant by 1.4 ± 1.2 %.[5]

The LiZnPn series highlights the numerous permutations of stable polytypes and coloring patterns possible within the Nowotny-Juza compounds (Figure 3). Due to the similar small electronegativity difference between Zn and Pn, it is clear these elements would prefer to be a part of the sp^3 tetrahedral network in all cases. As such, Li will be the stuffing atom (2a site) for all hexagonal polytypes. However, as mentioned above, in the cubic case, Zn prefers the heterocubic site for the larger Pn elements. Although the difference in energy between the two coloring patterns for cubic LiZnP make them unlikely to coexist, polytypism between hexagonal and cubic LiZnP should be attainable. For As, Sb, and Bi, the two possible cubic 4c site occupancies and the hexagonal polytype are all close enough in energy to be attainable depending on reaction conditions.

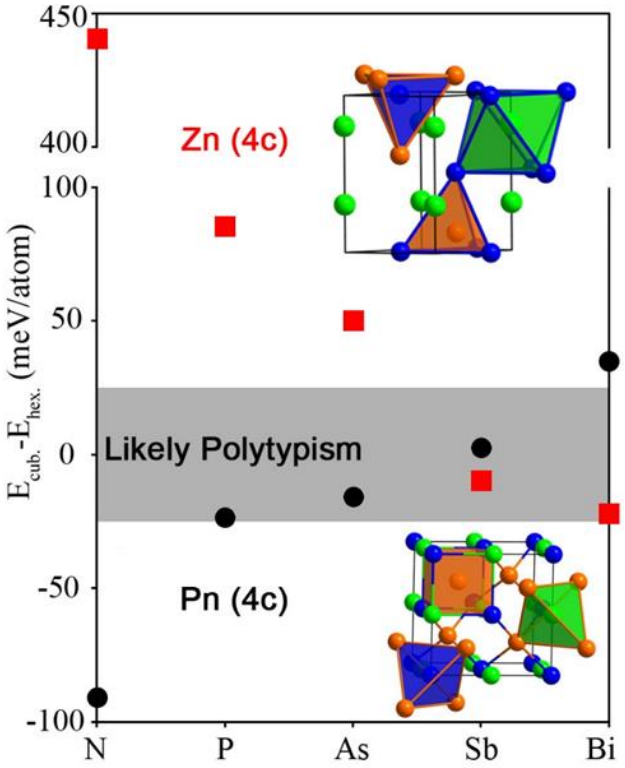

Figure 3. Comparison of the lowest energy structure for the LiZnPn series. Energy is given as the difference between one of two cubic MgAgAs-types and the hexagonal LiGaGe-type (positive values indicate hexagonal preferred). The area of the graph where polytypism is expected is shaded in grey. For the cubic phases, energies are given for both Zn (red square) and Pn (black circle) occupying the heterocubic (4c) site.

Nanostructuring and thermoelectrics

Half-Heusler phases have attracted considerable interest as potential thermoelectric phases due to their ease of synthesis, high melting points, and chemical stability.[46] However, due to their rather simple unit cell, they possess a high lattice thermal conductivity that inhibits their thermoelectric figure of merit ($zT=S^2\sigma T\kappa^{-1}$, where S is the Seebeck coefficient, σ is the electrical conductivity, T is the temperature, and κ is the thermal conductivity).[47,48] However, motivated by theoretical predictions, there has been considerable experimental work displaying that nanostructuring can decrease thermal conductivity and subsequently enhance

thermoelectric efficiency. To date, nanostructuring has primarily been achieved through grain size reduction *via* ball milling, doping, or the inclusion of alternate phases to induce grain boundaries between phases.[49,50] Along with a routine reduction in thermal conductivity with decreasing grain size, it is also possible to enhance Seebeck coefficient if crystallite sizes are small enough to exhibit quantum confinement.[51,52] In light of these experiments, filled tetrahedral semiconductors are once again being researched as an extremely promising class of thermoelectric phases. To date, the majority of focus has fallen on 18 e^- half-Heusler phases.[53]

Nanostructuring has been explored in numerous half-Heusler compositions but, of these, MNiSn (M = Ti, Zr, Hf) has been the most actively studied composition.[54,55] In bulk, these semiconductors have a band gap of 0.13–0.19 eV and typically achieve zT of ~ 0.2 at 700 K.[56] However, doping the M site with alternative group 4 elements leads to a substantial improvement, with a zT of up to 1.1 at 700 K (composition $Zr_{0.25}Hf_{0.75}NiSn$).[57] Furthermore, doping the Sn site with a minimal amount of Sb (< 2%) increased the zT to 1.09 at 800K (composition $Ti_{0.5}Hf_{0.5}NiSn_{0.98}Sb_{0.02}$).[58] These phases have the additional benefit of being efficient in both *n*-type and *p*-type compositions. For instance, a device consisting of *n*-type $Hf_{0.5}Zr_{0.5}NiSn_{0.995}Sb_{0.005}$ and *p*-type $Hf_{0.3}Zr_{0.7}CoSn_{0.3}Sb_{0.7}$ achieved a zT of 1.05 at 900 K and an efficiency of 8.7%.[59] Through doping of both sites, a zT of 1.5 at 700 K was obtained (composition $(Zr_{0.5}Hf_{0.5})_{0.5}Ti_{0.5}NiSn_{0.998}Sb_{0.002}$).[60]

The alternate 18 e^- MCoSb composition has also been nanostructured through the inclusion of full Heusler MCo_2Sb quantum dots within the nanocomposite.[61] This study once again found that thermal conductivity is reduced by increasing the number of grain boundaries. More importantly, it demonstrated that power factor ($PF = S^2\sigma$) can be substantially increased

through nanostructuring (140% increase with 5 mol% full Heusler inclusions). Despite promising advancement in modifying phonon and electron transport of these phases through top-down nanostructured methods, their commercial applicability is limited by the need for high temperature solid state reactions. A generally overlooked possibility to improve scalability and efficiency is through the generation of nanocomposites from solution processed, nanocrystal building blocks. Solution phase synthesis allows for complete control of size, composition, crystal phase, and surface chemistry that is not feasible through other methods.

Recently, one such example was demonstrated with PbS-Ag nanocomposites obtained by annealing a powder containing PbS and Ag nanocrystals.[62] While PbS has moderate thermoelectric performance by itself, the zT of the nanocomposite was increased three-fold. This was primarily due to a significant reduction in thermal conductivity, while at the same time retaining relatively high electrical conductivity. Colloidal synthesis optimization also showed a 30% increase over the highest figure of merit reported for PbS obtained by traditional doping. This study provides evidence that insulating can be readily removed from the surface of solution processed nanocrystals, without losing the benefit of numerous grain boundaries present in these materials. While widely applicable to filled tetrahedral semiconductors, only a limited number of these have been synthesized from solution.[5,19]

Balancing abundance, biocompatibility, and application

In the past 20 years, Cd, Pb, and As have been at the forefront of many semiconductor studies and applications. Examples include CdS, CdSe, PbS, GaAs, CdTe. Despite their attractive properties, a major drawback of these compounds is the presence of toxic heavy metals.[63] The toxicity of a material is often dependent on (i) the identity and abundance of the element, (ii) its oxidation state, (iii) and the physical state.[64] Typically, lighter elements tend

to be less toxic and more abundant than heavier elements with more d and f character. For example, Zn is about 200 times more abundant in the Earth's crust—and significantly more biocompatible—than Cd.[65] Similarly, Na is 1,115 times more abundant than Li which reduces application costs by 30 % making Na a more versatile element in Nowotny-Juza I-II-V phases.[66] As such, first row transition metals are attractive in Heusler materials. Elements with high oxidation states have enhanced chelating capabilities that can alter natural metabolic pathways. For example, Cr(VI) is toxic to many living organisms, while Cr(III) typically appears to have lower adverse effects.[67] Additionally, Tl^+ and K^+ are monovalent cations with similar radii, but Tl^+ has 10 times higher binding affinity than K^+ which substantially increases its toxicity.[68] The ability to fluctuate through multiple oxidation states and coordination environments further increases its toxicity.[69,70] Additionally, the physical state of a material (colloidal, crystalline, amorphous, solid, liquid) can also affect toxicity. For example, the toxicity of certain materials can be diminished if specific reactivity can be masked by passivation (ligands, epitaxial shell).[71,72] However, the rate of association and dissociation on the surface can determine toxicity. Taken together, colloidal Nowotny-Juza I-II-V phases appear an ideal alternative to many binary (III-V, IV-VI, etc.) semiconductors, based on both environmental and technological considerations.

Thesis Organization

Chapter 2 of this thesis describes the initial synthesis of phase pure LiZnP prepared from solution. The reaction proceeds through a zinc metal intermediate followed by intercalation of lithium and phosphorus. We show the extension of possible precursors to include *n*-butyllithium, diisopropylamide, phenyllithium, and lithium hydride for lithium; zinc stearate, zinc chloride, and diethylzinc for zinc; and *n*-trioctylphosphine and

triphenylphosphine for phosphorus. Additionally, the group II element is able to be exchanged for cadmium.

Chapter 3 extends the synthesis of LiZnP to include LiZnSb. Interestingly, LiZnSb prepared from solution adopted the cubic MgAgAs-type instead of the previously observed hexagonal LiGaGe-type. Along with the different crystal structure, this polytype also displayed a unique coloring pattern where the pnictide and zinc site are switched. Furthermore, through calculating the transport properties, we were able to identify this cubic polytype to be a promising thermoelectric material.

Chapter 4 conducts a thorough investigation of the effect of reaction parameters in the synthesis developed in Chapter 3. We utilize the high throughput facilities at Lawrence-Berkeley National Laboratory to screen the impact of precursor concentration, nucleation and growth temperature, reaction time, and injection order on the products. By doing so, we construct a phase space diagram to target either ternary, binary, or unary phases. One of the synthesized ternaries is a variant ($CaZn_2Sb_2$-type) of the previously observed hexagonal LiGaGe-type where the c-axis is considerably extended to create a 2D structure. Through monitoring the reaction with PXRD, TEM, and XPS, we were able to determine a mechanism for formation of this observed phase. Chapter 5 provides a conclusion for the thesis contents and provides an outlook for future work.

References

1. D. M., Wood, A. Zunger, R. Groot. *Phys. Rev. B*, **1985**, *31*, 2570-2573.
2. F. Casper, R. Seshadri, C. Felser, *C. Phys. Status Solidi A* **2009**, *206*, 1090-1095.
3. X. Zhang, L. Yu, A. Zakutayev, A. Zunger, *Adv. Funct. Mater.* **2012**, *22*, 1425–1435.
4. C.-Y Yeh, Z. W. Lu, S. Froyen, A. Zunger, *A. Phys. Rev. B* **1992**, *46*, 10086–10097.

5. M. A. White, J. G. Miller, J. Vela, *J. Am. Chem. Soc.* **2016**, *138*, 14574–14577.

6. J. Pierre, R. V. Skolozdra, J. Tobola, S. Kapryzk, C. Hordequin, M. A. Kouacou, I. Karla, R. Currat, E. Leliévre-Berna, *J. Alloys Compd.* **1997**, *262-263*, 101–107.

7. H. C. Kandpal, C. Felser, R. Seshadri, *J. Phys. D: Appl. Phys.* **2006**, *39*, 776–785.

8. E. N. Christensen, *Phys. Rev. B: Condens. Matter Mater. Phys.* **1985**, *32*, 6490–6497.

9. H. Luo, Z. Zhu, G. Liu, S. Xu, G. Wu, H. Liu, J. Qu, Y. Li, *Phys. Rev. B: Condens. Matter Mater. Phys.* **2008**, *403*, 200–206.

10. C. H. Kandpal, G. H. Fecher, C. Felser, *J. Phys. D: Appl. Phys.* **2007**, *40*, 1507–1523.

11. C. H. Kandpal, C. Felser, R. Seshadri, *J. Phys. D: Appl. Phys.* **2006**, *39*, 776–785.

12. D. Kieven, R. Klenk, S. Naghavi, C. Felser, T. Gruhn, *Phys. Rev. B* **2010**, *81*, 75208-75214.

13. A. Zakutayev, X. Zhang, A. Nagaraja, L. Yu, S. Lany, T. To. Mason, D. S. Ginley, A. Zunger, *J. Am. Chem. Soc.* **2013**, *135*, 10048–10054.

14. H. Nowotny, K. Backmayer, *Monatsh. Chem.* **1950**, *81*, 488-496.

15. R. Juza, F. Z. Hund, *Z. Anorg. Allg. Chem.* **1948**, *257*, 1-12.

16. K. Kushida, Y. Kaneko, K. Kuriyama, *Phys. Rev. B* **2004**, *70*, 233303-233306.

17. A. E. Carlsson, A. Zunger, D. M. Wood, *Phys. Rev. B* **1985**, *32*, 1386–1389.

18. Kalarasse, F.; Bennecer, B.; Mellouki, A.; Kalarasse, L. *Comput. Mater. Sci.* **2008**, *43*, 791–795.

19. A. M. White, M. J. Thompson, G. J. Miller, J. Vela, *Chem. Commun.* **2016**, *52*, 3497–3499.

20. M. K. Yadav, B. Sanyal, *J. Alloys Compd.* **2015**, *622*, 388–393.

21. F. Caper, T. Graf, S. Chadov, B. Balke, C. Felser, *Semicond. Sci. Technol.* **2012**, *27*, 063001-063008.

22. D. Kieven, A. Grimm, A. Beleanu, C. G. F. Blum, J. Schmidt, R. Rissom, I. Lauermann, T. Gruhn, C. Felser, R. Klenk, *Thin Solid Films* **2011**, *519*, 1866–1871.

23. A. Beleanu, M. Mondeshki, Q. Juan, F. Casper, C. Felser, F. Porcher, *J. Phys. D: Appl. Phys.* **2011**, *44*, 475302-475306.

24. B. W. Montag, M. A. Reichenberger, K. R. Arpin, M. Sunder, K. A. Nelson, P. B. Ugorowski, D. S. McGregor, *J. Cryst. Growth* **2015**, *412*, 103–108.

25. M. H. Mobarok, E. J. Luber, G. M. Bernard, L. Peng, R. E. Wasylishen, J. M. Buriak, *Chem. Mater.* **2014**, *26*, 1925–1935.

26. A. E. Henkes, R. E. Schaak, *Chem. Mater.* **2007**, *19*, 4234–4242.

27. A. E. Henkes, Y. Vasquez, R. E. Schaak, *J. Am. Chem. Soc.* **2007**, *129*, 1896–1897.

28. E. J. Popczun, J. R. McKone, C. G. Read, A. J. Biacchi, A. M. Wiltrout, N. S. Lewis, R. E. Schaak, *J. Am. Chem. Soc.* **2013**, *135*, 9267–9270.

29. S. Carenco, D. Portehault, C. Boissière, N. Mézailles, C. Sanchez, *Chem. Rev.* **2013**, *113*, 7981–8065.

30. R.-K. Chiang, R.-T. Chiang, *Inorg. Chem.* **2007**, *46*, 369–371.

31. E. Muthuswamy, P. R. Kharel, G. Lawes, S. L. Brock, *ACS Nano* **2009**, *3*, 2383–2393.

32. S. L. Brock, K. Senevirathne, *J. Solid State Chem.* **2008**, *181*, 1552–1559.

33. H. P. Andaraarachchi, M. J. Thompson, M. A. White, H.-J. Fan, J. Vela, *Chem. Mater.*, **2015**, *27*, 8021-8031.

34. R. A. Finnegan, H. W. Kutta, *J. Org. Chem.*, **1965**, *30*, 4138-4144.

35. G. K. H. Madsen, *J. Am. Chem. Soc.* **2006**, *128*, 12140–12146.

36. E. S. Toberer, A. F. May, C. J. Scanlon, G. J. Snyder, *J. Appl. Phys.* **2009**, *105*, 063701.

37. J. K. Burdett, S. Lee, T. J. McLarnan, *J. Am. Chem. Soc.* **1985**, *107*, 3083–3089.

38. G. J. Miller, *Eur. J. Inorg. Chem.* **1998**, *1998*, 523–536.

39. P. Haas, F. Tran, P. Blaha, *Phys. Rev. B* **2009**, *79*, 085104.

40. J. P. Perdew, K. Burke, M. Ernzerhof, *Phys. Rev. Lett.* **1996**, *77*, 3865–3868.

41. A. D. Becke, E. R. Johnson, *J. Chem. Phys.* **2006**, *124*, 221101.

42. F. Tran, P. Blaha, *Phys. Rev. Lett.* **2009**, *102*, 266401.

43. A. Bouhemadou, S. Bin-Omran, D. Allali, S. M. Al-Otaibi, R. Khenata, Y. Al-Douri, M. Chegaar, A. H. Reshak, *Mater. Res. Bull.* **2015**, *64*, 337–346.

44. D. Bende, Y. Grin, F. R. Wagner, *Chem. - Eur. J.* **2014**, *20*, 9702–9708.

45. B. Dunn, H. Kamath, J.-M. Tarascon, *Science* **2011**, *334*, 928–935.

46. J. R. Sootsman, D. Y. Chung, M. G. Kanatzidis, *Angew. Chem. Int. Ed.* **2009**, *48*, 8616–8639.

47. G. J. Snyder, E. S. Toberer, . *Nat. Mater.* **2008**, *7*, 105–114.

48. W. Xie, A. Weidenkaff, X. Tang, Q. Zhang, J. Poon, T. Tritt, *Nanomaterials* **2012**, *2*, 379–412.

49. R. Ovik, B. D. Long, M. C. Barma, M. Riaz, M. F. M. Sabri, S. M. Said, R. Saidur, *Renewable Sustainable Energy Rev.* **2016**, *64*, 635–659.

50. A. J. Minnich, M. S. Dresselhaus, Z. F. Ren, G. Chen, *Energy Environ. Sci*. **2009**, *2*, 466-479.

51. D. L. Medlin, G. J. Snyder, *Curr. Opin, Colloid Interface Sci.* **2009,** *14*, 226-235.

52. M. S. Dresselhaus, G. Chen, M. Y. Tang, R. G. Yang, H. Lee, D. Z. Wang, Z. F. Ren, J.-P. Fleurial, P. Gonga, *Adv. Mater.* **2007**, *19*, 1043–1053.

53. W. G. Zeier, J. Schmitt, G. Hautier, U. Aydemir, Z. M. Gibbs, C. Felser, G. J. Snyder, *Nat. Rev. Mater.* **2016**, *1*, 16032-16042.

54. J. R. Sootsman, D. Y. Chung, M. G. Kanatzidis, *Angew. Chem. Int. Ed.* **2009**, *48*, 8616–8639.

55. T. Graf, C. Felser. S. S. P. Parkin, *Prog. Solid State Chem.* **2011**, *39*, 1–50.

56. H. Hohl, A. P. Ramirez, W. Kaefer, K. Fess, C. Thurner, C. Kloc, E. Bucher, *MRS Online Proc. Libr.* **1997**, *478*, 109-114.

57. A. Bhardwag, D. K. Misra, J. J. Pulikkotil, S. Auluck, A. Dhar, R. C. Budhani, *Appl. Phys. Lett.* **2012**, *101*, 133103-133108.

58. K. S. Kim, Y.-M, Kim, H. Mun, J. Kim, J. Park, A. Y. Borisevich, K. H. Lee, S. W. Kim, *Adv. Mater.* **2017**, 1702091-1702102.

59. S. J. Poon, D. Wu, S. Zhu, W. Xie, T. M. Tritt, P. Thomas, R. Venkatasubramanian, *J. Mater. Res.* **2011**, *26*, 2795–2802.

60. S. Sakurada, N. Shutoh, *Appl. Phys. Lett.* **2005**, *86*, 082105-082107.

61. P. Sahoo, Y. Liu, J. P. A. Makongo, X.-L. Su, S. J. Kim, N. Takes, H. Chi, C. Uher, X. Pan, P. F. P. Poudeu, *Nanoscale* **2013**, *5*, 9419-9427.

62. M. Ibáñez, Z. Luo, A. Genç, L. Piveteau, S. Ortega, D. Cadavid, O. Dobrozhan, Y. Liu, M. Nachtegaal, M. Zebarjadi, J. Arboil, M. V. Kovalenko, A. Cabot, *Nat. Commun.* **2016**, *7*, 10766-10772.

63. G. Chen, I. Roy, C. Yang, P. N. Prasad, *Chem. Rev.* **2016**, *116*, 2826–2885.

64. G. E. Brown, A. L. Foster, J. D. Ostergren, *Proc. Natl. Acad. Sci.* **1999**, *96*, 3388-3395.

65. P. C. K. Vesborg, T. F. Jaramillo, *RSC Adv.* **2012**, *2*, 7933-7947.

66. D. Larcher, J-M. Tarascon, *Nat. Chem.* **2014**, *7*, 19–29.

67. K. H. Thompson, C. Orvig, *Science* **2003**, *300*, 936–939.

68. V. Zitko, *Sci. Total Environ.* **1975**, *4*, 185-192.

69. D. Caussy, M. Gochfeld, E. Gurzau, C. Neagu, H. Ruedel, *Ecotoxicol. Environ. Saf.* **2003**, *56*, 45-51.

70. J. M. Wood, *Environ. Sci. Technol.* **1983,** *17*, 582A-590A.

71. C.K. Jain, I. Ali, *Wat. Res.* **2000**, *17*, 4304-4312.

72. J. F. Banfield, H. Zhang, *Rev. Mineral. Geochem.* **2001**, *44*, 1-58.

CHAPTER 2

GOT LiZnP? SOLUTION PHASE SYNTHESIS OF FILLED TETRAHEDRAL SEMICONDUCTORS IN THE NANOREGIME

Reprinted with permission from *Chemical Communications*, **2016**, 52, 3497-3499

Miles A. White, Michelle J. Thompson, Gordon J. Miller, and Javier Vela

Abstract

We report the synthesis and characterization of nanocrystalline LiZnP. The reaction proceeds through a zinc metal intermediate followed by rapid incorporation of lithium and phosphorus. We demonstrate flexibility in the selection of Li, Zn, and P precursors, as well as extension of this method to other half-Heusler phases.

Introduction

Half-Heusler phases are an interesting class of compounds with the general formula XYZ. Their structure can be described as a zinc-blende lattice of Y and Z stuffed with an interpenetrating fcc lattice of X (Fig. 1). A special instance of these compounds is when X, Y, and Z are comprised of elements from group I, II, and V, respectively (for instance Li, Zn, and P). These compounds, known as Nowotny–Juza phases,[1–3] have attracted considerable attention due to their potential application in thermoelectric devices,[4] solar cells,[5,6] neutron detectors,[7] and anode materials for Li ion batteries.[8] The electronic structure of these compounds resembles classic group IV or III–V 8 e^- semiconductors because of the presence of the $(II–V)^-$ zinc-blende lattice.[9] Because of this, the band gap of Nowotny–Juza phases can be tuned based on the electronegativity difference of the elements comprising the zinc-blende network.[10]

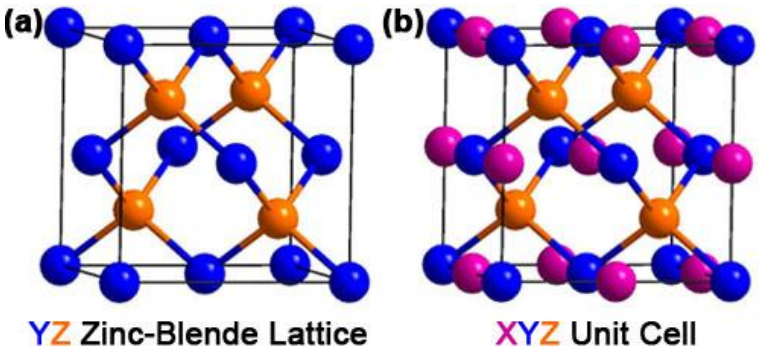

Fig. 1. (a) Partial unit cell of half-Heusler *XYZ* showing the covalent zinc-blende lattice of *Y* and *Z* (without *X*). (b) Full *XYZ* unit cell with *X* occupying the octahedral holes in the *YZ* lattice.

Heavier, n-type 18 e^- half-Heusler phases have already shown promise for thermoelectric devices. For instance, Ti doped (Zr,Hf)NiSn displayed a figure of merit (zT) of 1.5 at 700 K.[11,12] Similarly, a recent computational investigation of Nowotny–Juza phases showed high power conversion efficiencies and large carrier effective masses,[4] both of which are promising signs of their ability to be used in thermoelectric devices. For example, LiZnSb was suggested as a thermoelectric material with zT ≈ 2 at 600 K.[13,14] Nowotny–Juza phases have also attracted attention as a buffer layer in $CuIn_xGa_{1-x}Se_2$ (CIGS) solar cells. This layer should contain a material with a band gap of no less than 2.0 eV and a lattice constant of 5.9 Å.[10] Currently, CdS and other cadmium containing compounds are used to satisfy these criteria. However, an alternative material is desirable due to the toxicity of cadmium. LiZnP has a 2.0 eV band gap, as well as a similar unit cell and lattice parameter compared to CIGS, thus enabling epitaxy between these two materials.

Despite the potential use of LiZnP and other Nowotny–Juza phases in thermoelelectric and photovoltaic devices, their synthesis has been limited to the bulk, starting from the constituent elements, through the use of high temperature solid-state reactions.[7,15,16] A

reduction in particle size could lower thermal conductivity which, in turn, could increase thermoelectric efficiency. Additionally, lower temperature and solution phase preparations could be useful in fine-tuning the optical and electronic properties of these materials, decreasing lattice strain, and improving their processability and implementation into flexible devices.[17,18] Herein, we report the first solution phase synthesis of nanoscale LiZnP and LiCdP.

Results and Discussion

Nanocrystalline LiZnP was initially synthesized by reacting lithium hydride, diethyl zinc (injected at 250 °C), and an excess of tri-n-octylphosphine (TOP) at 330 °C (Scheme 1).

$$\text{LiH + xs TOP} \xrightarrow[\text{2) 330 °C, time}]{\text{1) } ZnEt_2\text{, 250 °C}} \text{LiZnP}$$

Scheme 1. Synthesis of nanocrystalline LiZnP.

TOP was chosen as a P source due to its ability to simultaneously act as both solvent and surface passivating ligand. The reaction was monitored by precipitating the solid products and analyzing them by powder X-ray diffraction (XRD) (Figure 2). Our data clearly show that metallic zinc forms immediately upon injection of diethyl zinc into the reaction mixture. This behavior is reminiscent of that reported during the colloidal synthesis of other metal phosphide nanoparticles that utilize TOP as the P source.[19–25] LiZnP begins to be observable after 10 min of reaction at 330 °C, and becomes the only crystalline phase observable by XRD within 20 min. Longer reaction times do not appear to have any detrimental effect on crystallinity or particle size (estimated from Scherrer equation). To test whether the reaction truly progresses through a Zn metal intermediate, Zn metal nanoparticles were synthesized ex situ and subsequently used as the injected Zn source (in lieu of $ZnEt_2$). As before, this reaction yielded a majority of nanocrystalline LiZnP (see Fig. S1).

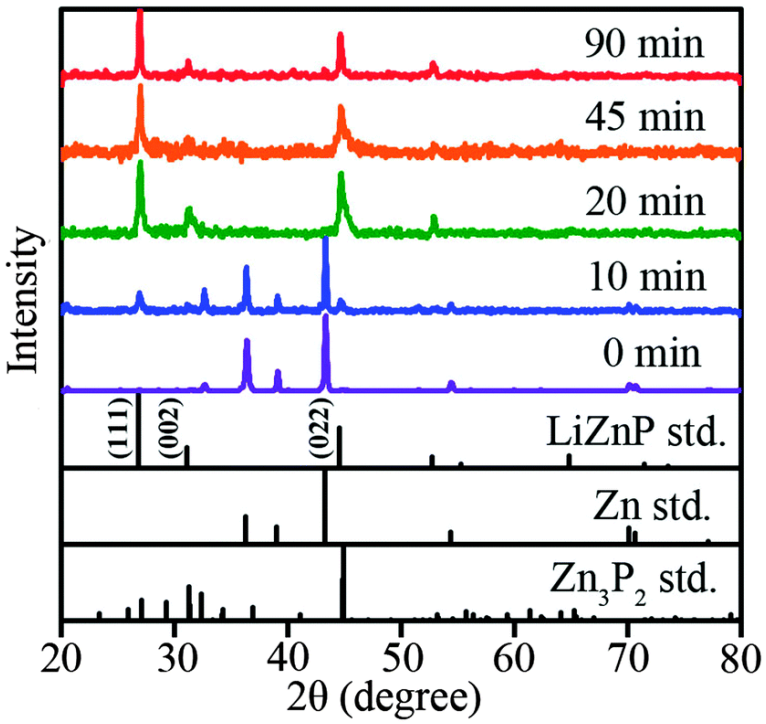

Fig. 2. Powder XRD of solids isolated after reacting LiH, Et_2Zn and TOP at different time and 330 °C. Std. patterns are in black.

Using a transmission electron microscope (TEM), energy-dispersive X-ray spectroscopy (EDX) (see Fig. S2 and S3) was employed to further characterize the LiZnP particles. While this technique is unable to detect the light (low *Z*) Li element, EDX allows gathering critical information about the relative Zn and P content. Representative data taken from several sample areas showed 36.3 ± 0.7 atom% Zn and 63.7 ± 0.4 atom% P. We attribute the deviation from the anticipated 1 : 1 Zn to P ratio to the presence of excess ligand (TOP) in the sample. This hypothesis is supported by TEM and XPS measurements, which show some amorphous material surrounding the nanocrystals (see Fig. S2 and S3).

Distinct powder rings without outlier reflections in the selected area electron diffraction (SAED) show the high level of crystallinity possessed by these particles as well as the absence of other identifiable crystalline phases (see Fig. S2). The observed reflections correspond well

to the lattice d-spacings expected for LiZnP. The most intense reflection (111) is located very near the beam stop and is difficult to discern. Instead, the second most intense reflection (022) is the first easily observed ring. As such, this ring is the most prominent in the SAED. All other observed reflections agree with LiZnP d-spacings.

The electronic and optical properties of LiZnP nanoparticles are important for their potential integration into energy conversion devices. The optical absorption spectrum of LiZnP is consistent with the direct forbidden band gap reported for this material.[15,26,27] The magnitude of this gap was found to be 2.0 eV using a Tauc plot (Fig. 3). A lack of sharp absorption features suggests the LiZnP particles are not quantum confined. This is understandable based on the large effective carrier masses of Nowotny–Juza phases,[4] which are nonetheless ideal for the development of more efficient thermoelectric materials.

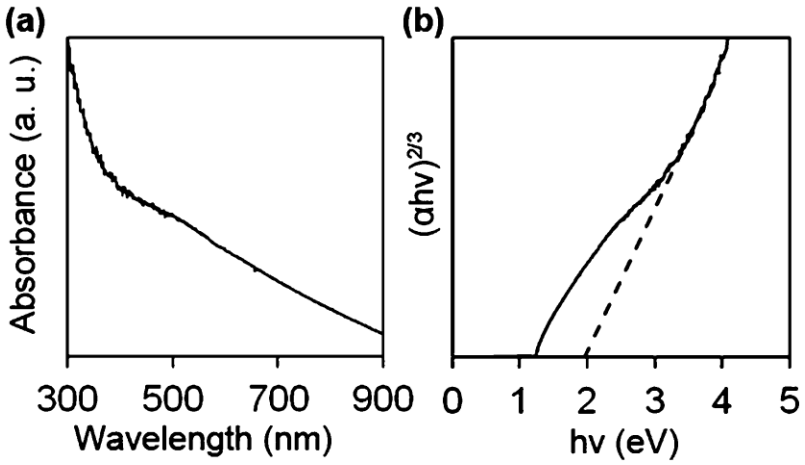

Fig. 3. (a) UV-Vis absorbance spectra for LiZnP and (b) Tauc plot displaying a band gap of 2.0 eV.

We have sought to probe the synthetic flexibility of our reaction by investigating the use of alternative precursors. We specifically looked to increase the homogeneity of the reaction through the use of soluble organolithium reagents, as well as to develop less reactive zinc reagents. Various organolithium reagents are widely accessible, and some are known to

undergo reductive elimination at elevated temperatures to yield LiH.[28] Repeating the parent reaction with *n*-butyllithium (*n*-BuLi), lithium diisopropylamide (LDA), or phenyllithium (PhLi) instead of LiH yielded phase pure LiZnP (see Fig. S5). Critically, the ability to better control the quantity of lithium added using one of these two soluble reagents allowed us to control the particle size by simply fine-tuning the reaction stoichiometry. Altering the Li to Zn from 1 : 1 to 5 : 1 changed the LiZnP particle size from 10 nm to 25 nm (estimated by the Scherrer equation, see Fig. S6).

In our search for non-pyrophoric, safer alternatives to Et_2Zn, we found that either zinc stearate ($ZnSt_2$) or zinc chloride ($ZnCl_2$) can be used to successfully generate LiZnP (see Fig. S7). The use of a zinc carboxylate, in particular, is not only greener, but also potentially beneficial for size control. In the case of Zn_3P_2, it has been demonstrated that passivation with a carboxylate ligand results in much smaller particle size than that observed with TOP.[29] Similarly, we found that other phosphines such as triphenylphosphine (Ph_3P, m.p. = 80.5 °C) can also be successfully used as a solvent and phosphorous source instead of TOP, although this required longer reaction times to form LiZnP (6 h, PPh_3 *vs.* 20 min, TOP).

Finally, based on our ability to synthesize LiZnP nanocrystals with a variety of reagents and conditions, we sought to generalize the scope of our approach to the synthesis of other Nowotny–Juza phases. To test this hypothesis, we replaced dimethyl cadmium with diethyl zinc in the parent reaction in an attempt to synthesize LiCdP. Powder XRD reveals the formation of majority phase LiCdP, accompanied by a Cd_3P_2 impurity phase (see Fig. S8). While some optimization is needed in order to remove excess ligand (from LiZnP) or impurity phases (from LiCdP), the ability to generate nanocrystals of both Nowotny–Juza phases through a simple, low temperature solution phase method with a variety of reagents is

encouraging. More generally, a broader survey of the solution-phase synthesis of other nanocrystalline Nowotny–Juza compounds is warranted, although this is beyond the scope of this communication.

Conclusions

In conclusion, nanocrystalline LiZnP and LiCdP were prepared at low temperature using solution phase synthesis. Our general approach relies on the use of a neat, high boiling phosphine such as TOP or PPh_3 as both phosphorus source and solvent, and proceeds through the *in situ* generation of an intermediate metallic phase (for example, Zn). Powder XRD and TEM data showcase the high crystallinity as well as the relative thermal stability of LiZnP. Further, the optical properties match those of the bulk. Because of its synthetic flexibility and generality, this synthetic approach has the potential to be useful in the preparation of other Nowotny–Juza phases. Future experiments will explore the effects of stoichiometry and precursor reactivity on the composition, size and shape control of these and other related nano phases.[30,31]

Acknowledgments

J. Vela thanks the US National Science Foundation for a CAREER grant from the Division of Chemistry, Macromolecular, Supramolecular and Nanochemistry program (1253058).

References

1. A. Zakutayev, X. Zhang, A. Nagaraja, L. Yu, S. Lany, T. O. Mason, D. S. Ginley and A. Zunger, *J. Am. Chem. Soc.*, **2013**, *135*, 10048.
2. H. Nowotny and K. Bachmayer, *Monatsh. Chem.*, **1950**, *81*, 488.
3. R. Juza and F. Hund, *Z. Anorg. Chem.*, **1948**, *257*, 1.
4. M. K. Yadav and B. Sanyal, *J. Alloys Compd.*, **2015**, *622*, 388.

5. F. Casper, T. Graf, S. Chadov, B. Balke and C. Felser, *Semicond. Sci. Technol.*, **2012**, *27*, 063001.

6. D. Kieven, A. Grimm, A. Beleanu, C. G. F. Blum, J. Schmidt, T. Rissom, I. Lauermann, T. Gruhn, C. Felser and R. Klenk, *Thin Solid Films*, **2011**, *519*, 1866.

7. B. W. Montag, M. A. Reichenberger, K. R. Arpin, M. Sunder, K. A. Nelson, P. B. Ugorowski and D. S. McGregor, *J. Cryst. Growth*, **2015**, *412*, 103.

8. A. Beleanu, M. Mondeshki, Q. Juan, F. Casper, C. Felser and F. Porcher, *J. Phys. D: Appl. Phys.*, **2011**, *44*, 475302.

9. K. Kuriyama, Y. Takahashi and K. Tomizawa, *Phys. Rev. B: Condens. Matter Mater. Phys.*, **1993**, *47*, 13861.

10. D. Kieven, R. Klenk, S. Naghavi, C. Felser and T. Gruhn, *Phys. Rev. B: Condens. Matter Mater. Phys.*, **2010**, *81*, 075208.

11. S. Sakurada and N. Shutoh, *Appl. Phys. Lett.*, **2005**, *86*, 082105.

12. R. A. Downie, D. A. MacLaren, R. I. Smith and J. W. G. Bos, *Chem. Commun.*, **2013**, *49*, 4184.

13. G. K. H. Madsen, *J. Am. Chem. Soc.*, **2006**, *128*, 12140.

14. E. S. Toberer, A. F. May, C. J. Scanlon and G. J. Snyder, *J. Appl. Phys.*, **2009**, *105*, 063701.

15. K. Kuriyama, T. Katoh and N. Mineo, *J. Cryst. Growth*, **1991**, *108*, 37.

16. R. Bacewicz and T. F. Ciszek, *Appl. Phys. Lett.*, **1988**, *52*, 1150.

17. E. J. Luber, M. H. Mobarok and J. M. Buriak, *ACS Nano*, **2013**, *7*, 8136.

18. S. K. Bux, J.-P. Fleurial and R. B. Kaner, *Chem. Commun.*, **2010**, *46*, 8311.

19. M. H. Mobarok, E. J. Luber, G. M. Bernard, L. Peng, R. E. Wasylishen and J. M. Buriak, *Chem. Mater.*, **2014**, *26*, 1925.

20. A. E. Henkes, Y. Vasquez and R. E. Schaak, *J. Am. Chem. Soc.*, **2007**, *129*, 1896.

21. A. E. Henkes and R. E. Schaak, *Chem. Mater.*, **2007**, *19*, 4234.

22. S. Carenco, D. Portehault, C. Boissière, N. Mézailles and C. Sanchez, *Chem. Rev.*, **2013**, *113*, 7981.

23. R.-K. Chiang and R.-T. Chiang, *Inorg. Chem.*, **2007**, *46*, 369.

24. E. Muthuswamy, P. R. Kharel, G. Lawes and S. L. Brock, *ACS Nano*, **2009**, *3*, 2383.

25. S. L. Brock and K. Senevirathne, *J. Solid State Chem.*, **2008**, *181*, 1552.

26. K. Kuriyama and T. Katoh, *Phys. Rev. B: Condens. Matter Mater. Phys.*, **1988**, *37*, 7140.

27. D. M. Wood, A. Zunger and R. de Groot, *Phys. Rev. B: Condens. Matter Mater. Phys.*, **1985**, *31*, 2570.

28. R. A. Finnegan and H. W. Kutta, *J. Org. Chem.*, **1965**, *30*, 4138

29. B. A. Glassy and B. M. Cossairt, *Chem. Commun.*, **2015**, *51*, 5283.

30. T. P. A. Ruberu, H. R. Albright, B. Callis, B. Ward, J. Cisneros, H.-J. Fan and J. Vela, *ACS Nano*, **2012**, *6*, 5348.

31. H. P. Andaraarachchi, M. J. Thompson, M. A. White, H.-J. Fan and J. Vela, *Chem. Mater.*, **2015**, *27*, 8021.

Appendix of supporting information

Synthesis: Tri-n-octylphosphine (5 mL, TOP, 97% Strem) and lithium hydride (10-20 mg, powder 97 % Alfa-Aesar) were added to a three-neck flask in dry N_2 filled glove box. The flask was then degassed for 30 min followed by refilling with Ar and heating to 250 °C. Diethyl zinc (56 wt. % Zn Sigma Aldrich), in the case of LiZnP, or dimethyl cadmium (97% Strem), for the synthesis of LiCdP (1 equiv), was then immediately injected. The reaction mixture was heated to 330 °C over the course of 10 min followed by continuous stirring over the period of time indicated. The crude product was washed with toluene (10 mL) followed by centrifugation at 5000 rpm for 10 min. The washed product was washed again after adding enough toluene to re-suspend the particles (roughly 3 mL). For alternative reagents, the following were also successfully used: (Li) n-Butyllithium (2.5M in hexane Sigma Aldrich), lithiumdiisopropylamine (10 wt. % in hexane Sigma Aldrich), and phenyllithium(1.6M in diethyl ether, Sigma Aldrich) ; (Zn) zinc stearate (tech. grade Sigma Aldrich), and zinc chloride (97% Anhydrous, Strem); (P) triphenylphosphine (99% Acros). *Caution:* On a few instances,

LiZnP prepared from n-BuLi ignited upon exposure to air. This is likely due to the presence of excess n-BuLi but needs further investigation.

Characterization: Powder X-ray diffraction data were measured using Cu Kα radiation on a Rigaku Ultima IV diffractometer. Transmission electron microscopy was conducted on carbon-coated nickel grids using a FEI Technai G2F20 field emission scanning transmission electron microscope (STEM) at 200 kV (point-to-point resolution <0.25 nm, line-to-line resolution <0.10 nm). Energy-dispersive X-ray spectroscopy was performed using area scans in STEM mode. Absorption spectra were measured with a photodiode array Agilent 8453 UV-Vis-NIR spectrophotometer. The XPS measurements were performed using a Kratos Amicus/ESCA 3400 instrument. The sample was irradiated with 240 W non-monochromated Mg *Kα* x-rays, and photoelectrons emitted at 0° from the surface normal were energy analyzed using a DuPont type analyzer. The pass energy was set at 75 eV. CasaXPS was used to process raw data files. Thermogravimetric analysis (TGA) and differential scanning calorimetry (DSC). Measurements were taken using a Netzsch STA449 F1 Jupiter® TGA/DSC instrument coupled to a Quadrupole Mass Spectrometer (QMS) and Bruker Tensor 27 FT-IR spectrometer. 10 mg sample in an alumina crucible was heated from 40 °C to 600 °C using Ar as the carrier gas and 10 °C /min for the ramp rate.

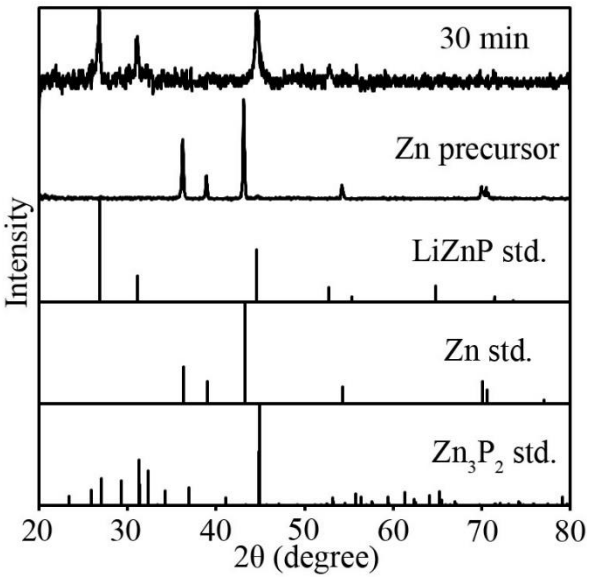

Figure S1. Experimental powder XRD patterns obtained for zinc metal generated *ex situ* and for nanocrystalline LiZnP using zinc metal as the Zn precursor after 30 min at 330 °C. Standard patterns of potential phases are shown for comparison.

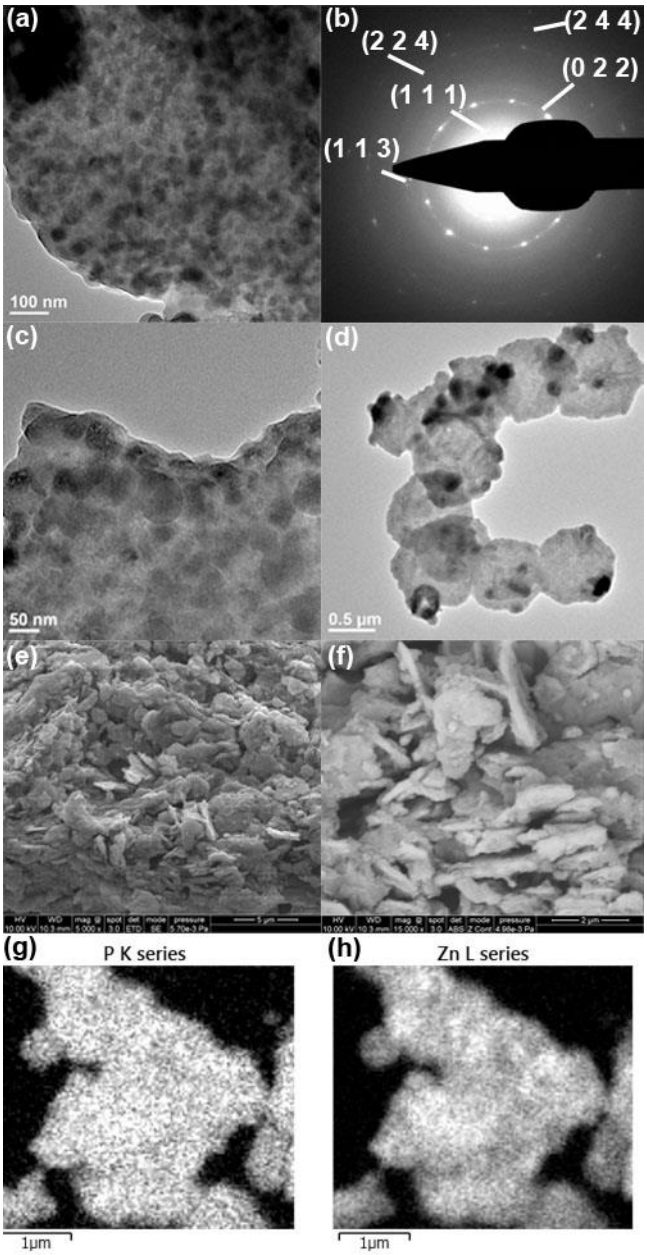

Figure S2. TEM image of nanocrystalline LiZnP particles (a, c, d). SAED of LiZnP from (a) with the visible reflections labelled with their corresponding lattice planes (b). SEM low magnification images of nanocrystalline LiZnP (e, f). Elemental mapping of phosphorus and zinc given in (g) and (h), respectively.

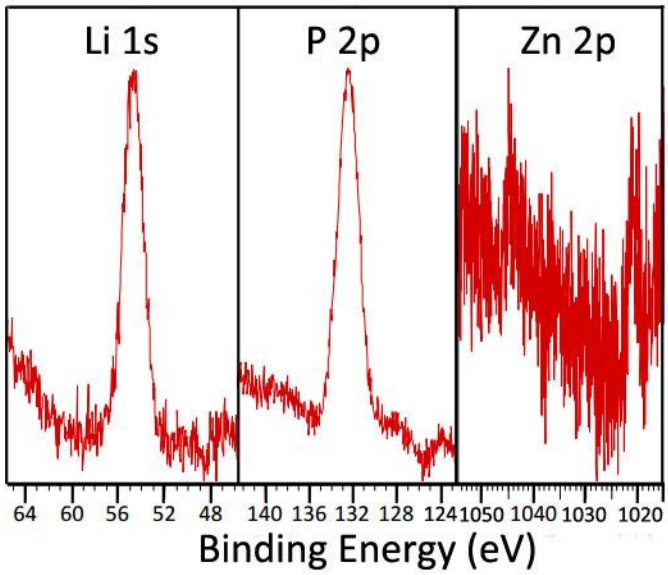

Figure S3. XPS of LiZnP nanocrystals prepared using TOP, LiH, and Et_2Zn at 330 °C for 30 min. Spectra contained two major peaks corresponding to Li^+ bound to oxygen (with a binding energy of 55 eV)[1] and P^{5+} bound to oxygen (with a binding energy of 133 eV).[2] XPS is a surface technique that only probes the first 5 nm with the majority of signal coming from the first 1-2 nm. For this reason, a large quantity of excess ligands bound to the particle surface could explain the lack of a Zn signal (see also TEM and thermal analysis). With knowledge that the nanocrystals were most likely not measured, it is feasible to assign the peaks corresponding to Li and P to excess LiOH and TOPO, respectively. This large excess of surface ligands is likely due to oligomerization of TOP which accounts for the aggregation and difficulty in discerning descrete particles by TEM imaging.

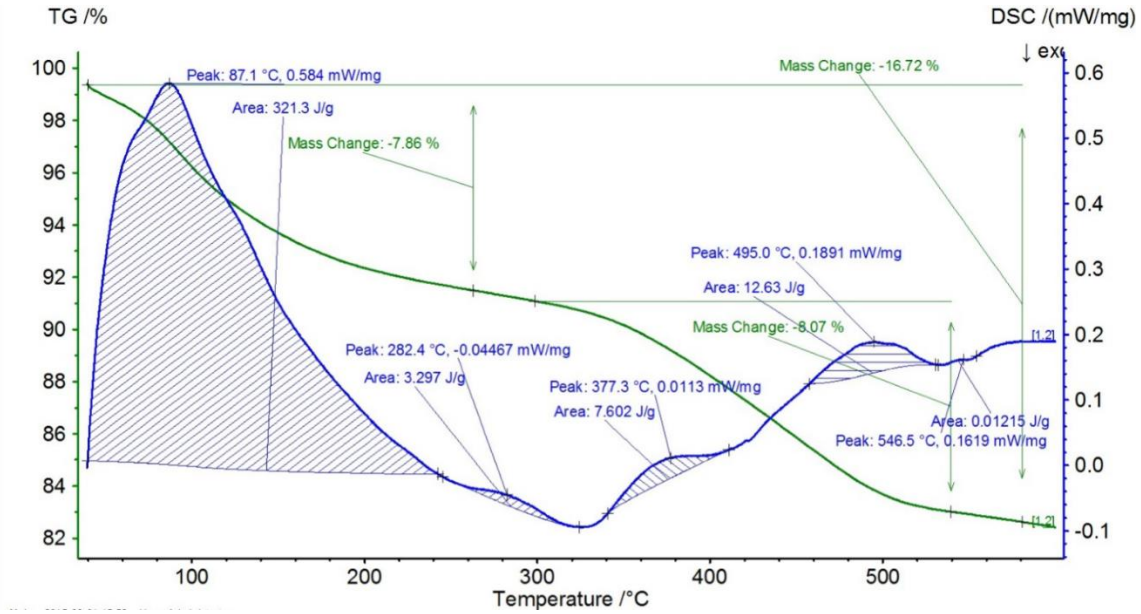

Figure S4. TGA/DSC data for LiZnP nanocrystals prepared using TOP, LiH, and Et_2Zn at 330 °C for 30 min. Broad mass loss from 250-500 °C is consistent with decomposition of TOPO ligands on the surface of the nanocrystals.

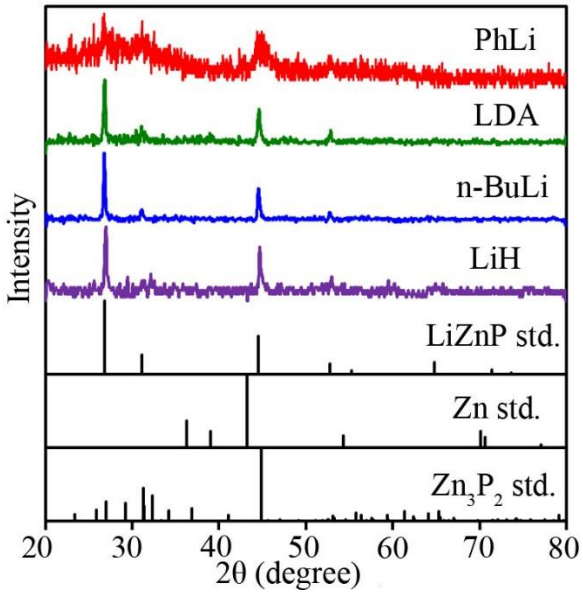

Figure S5. Experimental powder XRD patterns obtained for nanocrystalline LiZnP using LiH, n-BuLi, LDA and PhLi as the lithium source for 30 min at 330 °C. Standard patterns of potential phases are shown for comparison.

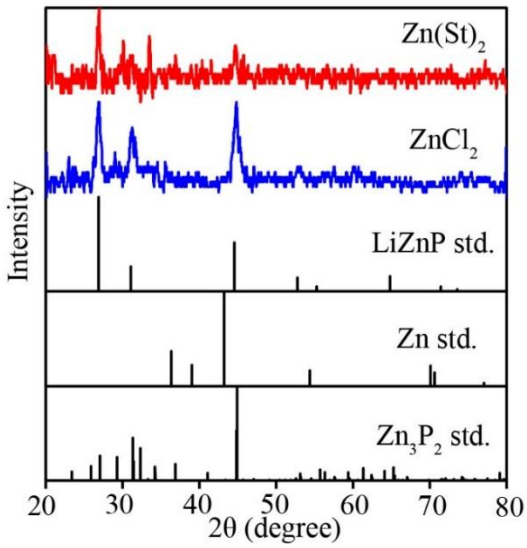

Figure S6. Experimental powder XRD patterns obtained using n-BuLi with $ZnCl_2$ (bottom exp. pattern) and LiH with $Zn(St)_2$ (top exp. pattern) for 30 min at 330 °C. Standard patterns of potential phases are shown for comparison.

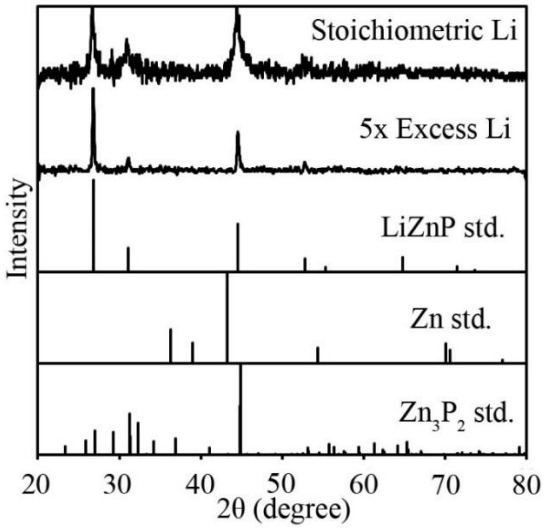

Figure S7. Experimental powder XRD patterns obtained using varying stoichiometry of n-BuLi relative to Et_2Zn for 30 min at 330 °C. Standard patterns of potential phases are shown for comparison. Particle size is found to be 25 nm in the case of excess n-BuLi and 10 nm for stoichiometric n-BuLi.

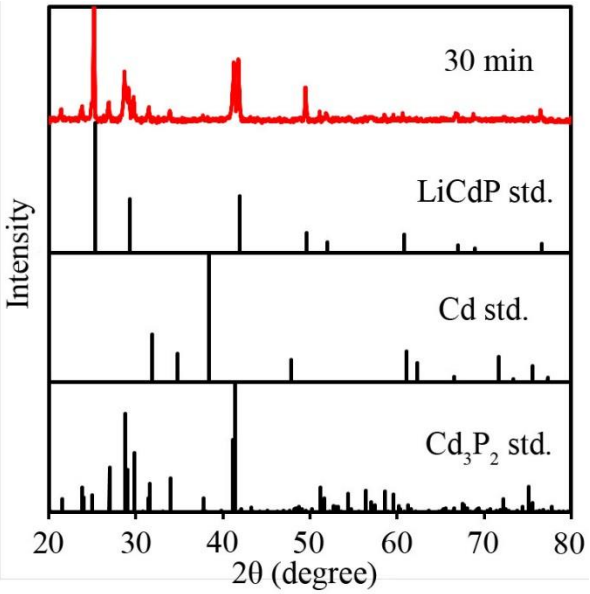

Figure S8. Experimental powder XRD pattern obtained for nanocrystalline LiCdP after 30 min at 330 °C. Standard patterns of potential phases are shown for comparison. The ratio of LiCdP to Cd_3P_2 was simulated to be 2:1.

Supplemental References

1. Suo, L.; Hu, Y.-S.; Li, H.; Armand, M.; Chen, L. *Nat. Commun*. **2013**, *4*, 1481.
2. Luber, E. J.; Mobarok, M. H.; Buriak, J. M. *ACS Nano* **2013**, *7*, 8136–8146.

CHAPTER 3

POLYTYPISM AND UNIQUE SITE PREFERENCE IN LIZNSB: A SUPERIOUR THERMOELECTRIC REVEALS ITS TRUE COLORS

Reprinted with permission from *Journal of the American Chemical Society*, **2016**, 138, 14574-14577

Miles A. White, Gordon J. Miller, and Javier Vela

Abstract

The first example of polytypism in the I− II−V semiconductors has been demonstrated with the synthesis of cubic LiZnSb by a low-temperature solutionphase method. This phase exhibits a unique coloring pattern that is novel for this class of compounds. The choice of site configuration has a considerable impact on the band structure of these materials, which in turn affects the transport properties. While the hexagonal polytype has been suggested as a promising n-type and extremely poor p-type thermoelectric material, the cubic analogue is calculated to have high efficiencies for both the n- and p-type derivatives (1.64 and 1.43, respectively, at 600 K). Furthermore, the cubic phase is found to be the energetically favored polytype. This surprising result provides a rationale for the lack of success in synthesizing the hexagonal polytype in either stoichiometric or n-type compositions.

Introduction

Thermoelectric materials offer an attractive means of generating electricity from heat that would otherwise be wasted. However, thermoelectrics have failed to reach largescale commercialization because of their relatively high cost and low device efficiency. The challenge with enhancing thermoelectric performance (given by the figure of merit, zT) arises from having to optimize three concordant properties (Seebeck coefficient S, electrical

conductivity σ, and thermal conductivity κ), all of which are dependent on the carrier concentration.[1] While this problem makes it difficult to intuitively increase the zT value, recent computational work shows promise in predicting new thermoelectric materials.[2] Among those suggested, lightly doped n-type (0.01 electron/unit cell) LiZnSb was calculated to have zT ~ 2 at 600 K.[3] However, the syntheses of n-type LiZnSb attempted to date resulted in unintentionally doped p-type LiZnSb with zT < 0.1.[4] Nevertheless, the experimental transport properties measured for this material were in good agreement with ab initio calculations, increasing the likelihood that the n-type analogue will have a high zT. In order to synthesize n-type LiZnSb, an alternative method is necessary to avoid unintentionally doped compositions at the commonly used annealing temperatures.

A potentially promising approach to synthesize LiZnSb is to use solution-phase techniques. The advantages of this method would be twofold. First, hot injection is likely to result in reduced particle size, which has been shown to lower the thermal conductivity and, with it, to increase the thermoelectric efficiency. Second, precursor manipulation can provide better synthetic control compared with traditional solid-state synthesis.[5]

Results and Discussion

Building upon the recent solution-phase synthesis of a related I−II−V semiconductor (collectively termed Nowotny−Juza phases),[6] we report the solution-phase synthesis of LiZnSb (Figure 1 and Scheme S1). Briefly, diethylzinc (0.2 mmol) and n-butyllithium (0.2 mmol) were injected in quick succession into a flask containing triphenylstibine (2.0 mmol) in 1-octadecene (5 mL) at 250 °C, after which the mixture was heated to 300 °C for 4 h. Despite prior literature reports that bulk LiZnSb made by solid-state synthesis exhibits a hexagonal structure, LiZnSb synthesized by this solution-phase method exhibits a previously unknown

cubic structure (a = 6.23 Å from Rietveld refinement), making it the first example of polytypism within the Nowotny−Juza phases. Furthermore, when lightly doped (<0.02 carriers/unit cell), n-type and p-type forms of this material are calculated to exhibit exceptional zT values of 1.64 and 1.43, respectively, at 600 K.

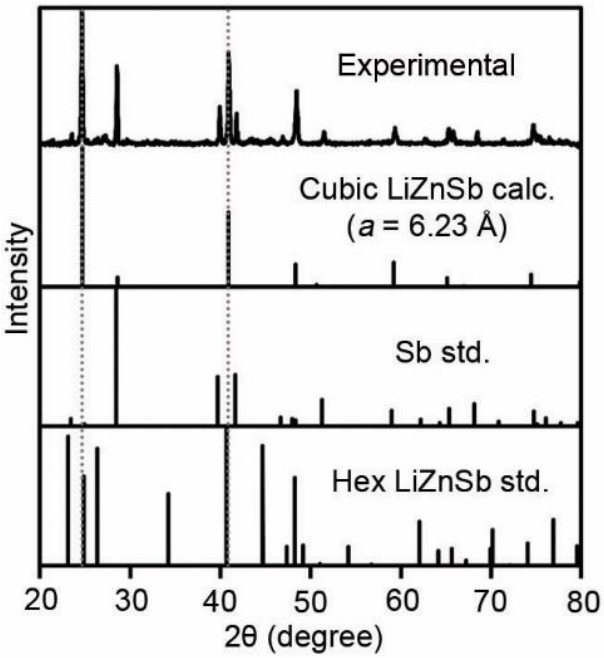

Figure 1. Experimental powder X-ray diffraction pattern containing cubic LiZnSb (first from top). Also shown are the calculated pattern of cubic LiZnSb (majority, *a* = 6.23 Å), the reference patterns of antimony metal (by-product), and the previously known hexagonal LiZnSb (unobserved). More information pertaining to the observed and calculated reflections can be found in Table S1.

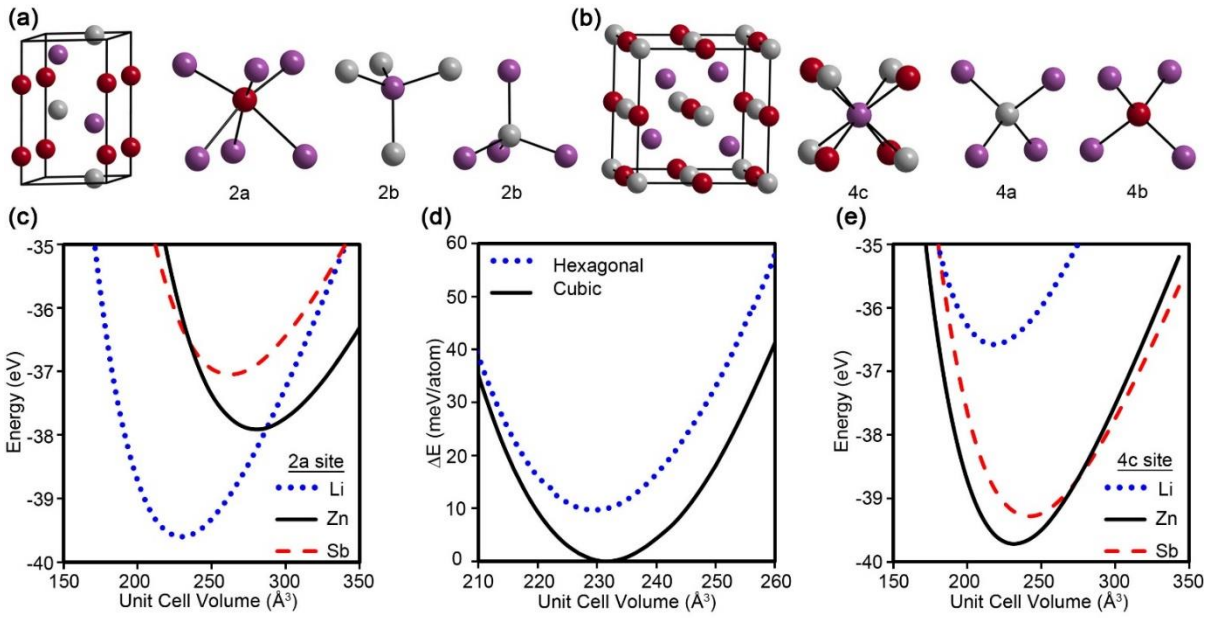

Figure 2. Unit cell, local environment, and energy *vs*. volume curves for hexagonal (a) and cubic (b) LiZnSb polytypes. The unique crystallographic sites that impact total energy with coloring are the 2a and 4c in the hexagonal and cubic unit cells, respectively (a,b). Energy *vs*. volume, *E*(V) curves for each of the constituent elements occupying the coloring site for both the hexagonal (c) and cubic (e) phases. A comparison between the lowest energy coloring patterns for hexagonal and cubic phases is given as a difference relative to the energy of the optimized cubic geometry (d).

Although previously unreported, the existence of polytypism in Nowotny-Juza phases is not entirely surprising. These phases are usually described as comprised of a wurtzite or zinc-blende substructure of groups II and V elements stuffed with a monovalent closed shell group I cation. Because these tetrahedral nets are isostructural and isoelectronic with classic 8-electron semiconductors, one could expect a low energy barrier for rearrangement of this structural component.[7] To probe the energy difference between the hexagonal and cubic polytypes, the Vienna *ab initio* simulation package (VASP) was used.[8,9]

VASP calculations used projected augmented-wave (PAW) pseudopotentials[10]. A conjugated algorithm was applied to the structural optimization with an 11 x 11 x 11 Monkhorst-pack k-points grid.[11] During structural optimizations, atomic coordinates as well as cell volumes were allowed to relax except for $E(V)$ curves, during which the cell volume was fixed. Total energies were calculated using the tetrahedron method with Blöchl corrections applied.[12] VASP calculations treated exchange and correlation by either the local density approximation (LDA) or the Perdew-Burke-Ernzerhof (PBE)[13] generalized gradient functional in the case of total energy calculations. To estimate accurate gaps from the band structures, the Tran-Blaha modified Becke-Johnson (TB-mBJ) potential was utilized.[14,15] Transport properties were calculated using the rigid-band approximation and constant scattering time approximation as implemented by the BoltzTraP code.[16] For these calculations, a much denser 41 x 41 x 41 k-point grid was used with the TB-mBJ potential due to the importance of an accurate band gap for transport property calculations. Denser k-meshes were used but found to yield similar results.

The experimentally reported hexagonal crystal structure of LiZnSb is comprised of a (ZnSb) wurtzite-type net stuffed with lithium. The analogous cubic polytype would be comprised of a (ZnSb) zinc blende framework stuffed with lithium. However, unlike in the hexagonal case, where the two wurtzite network positions have similar coordination environments, these two sites are inequivalent in the zinc blende substructure (Figure 2): One site, 4c has a heterocubic coordination environment formed by two tetrahedral surroundings to the other two constituent elements; the other site, 4b has tetrahedral coordination to the 4c site and octahedral coordination to the Li 4a site. Because of this, the choice of coloring pattern,[17,18] *i.e.* the distribution of elements among possible crystallographic sites, greatly impacts total

energy. To examine this question, total energy *vs.* volume curves were plotted for the cubic and hexagonal polytypes while retaining stoichiometry and symmetry (Figure 2).

The lowest energy coloring pattern for hexagonal LiZnSb agrees with experimental observations from prior solid-state synthesis of the bulk material. Having either Zn or Sb occupying the 2a site in a Li-based wurtzite structure is found to be highest in energy (Figure 2c). Similarly, in the cubic case, having lithium occupy the 4c site and being involved in the polar-covalent zinc blende network is not preferred (Figure 2e). Although not as unfavorable as Li, Sb occupying the 4c site is also energetically unfavorable. This is contrary to other cubic LiZnPn (Pn = N, P, As) Nowotny-Juza phases known in the bulk, which show a preference for the pnictide occupying the heterocubic site.[19,20] In fact, cubic LiZnSb is the first instance of a Nowotny-Juza phase with the group II element occupying the 4c site (see below).

To ensure the validity of this coloring approach, energy *vs.* volume, $E(V)$ curves were generated for a larger, comprehensive family of pnictide-containing cubic Nowotny-Juza phases (see Table S2). In all cases for which an experimental bulk cubic crystal structure is known, this agrees with the lowest energy calculated coloring pattern. The transition in cubic site preference occurs upon moving to the heavier pnictides (Sb and Bi). However, only the hexagonal phases of both LiZnSb and LiZnBi have previously been reported.

Along with a considerable energy difference, noticeable changes in lattice parameter are expected between coloring patterns. The theoretical *a* lattice parameter for cubic LiZnSb, calculated using the local density approximation (LDA) is 6.14 Å (Figure 1), slightly (1.4%) smaller than the experimental lattice constant of 6.23 Å obtained from Rietveld refinement. This agrees with the extent (1.4±1.2%) to which LDA underestimates the known experimental lattice parameters of other previously reported pnictide-containing cubic Nowotny-Juza phases

(see Table S1). LDA also underestimates (by 2.03%) the lattice parameters of hexagonal LiZnSb. In other words, the slightly low estimate of the lattice parameter for Zn occupying the 4c site is consistent with the limitations of this method, and in line with similar low estimates obtained by LDA in other classes of compounds.[21] Based on this comparison between the calculated cubic lattice parameter and powder XRD data, along with the energy difference between coloring patterns, we can assign Zn to the 4c site, despite prior LiZnPn structures having always preferred the pnictide on the 4c site. This site preference is not trivial, because the lattice constant and the band structure (see Fig. S1) are affected. In particular, the value and nature of the band gap, as well as the lowest energy conduction bands change with coloring. With Zn in the 4c site, cubic LiZnSb has an indirect band gap of 1.2 eV, whereas with Sb in this site, the material has a direct band gap of 1.3 eV. These differences significantly alter transport properties (below).

Having determined its crystal structure and most favorable site preference allows comparing the energy of the new cubic LiZnSb phase to the hexagonal polytype. As shown in Figure 1b, cubic LiZnSb is energetically preferred across all unit cell volumes. This result is surprising because it suggests that the thermodynamically less stable hexagonal phase forms at high temperature (in the bulk). However, all of the calculations were performed on stoichiometric phases whereas, based on past experiments, bulk hexagonal LiZnSb is known to be an unintentionally *p*-type doped and, likely, non-stoichiometric semiconductor.[4] These computational results provide a rationale for the extreme difficulty researchers have faced while trying to synthesize stoichiometric or *n*-type compositions of LiZnSb using high-temperature synthesis.

The calculated transport properties and thermoelectric efficiencies of cubic LiZnSb at 600 K with either Zn or Sb occupying the heterocubic 4c site are shown in Figure 3. In both cases, the large Seebeck coefficients give rise to impressive power factors of over 110 $\mu W/cmK^2s$. However, when Sb occupies the 4c site, the peak in power factor occurs at a doping level that is too high to be useful (even at 0.3 e^-/u.c. the power factor is still below 80 $\mu W/cmK^2s$). In contrast, when Zn occupies this site, the power factor increases much more abruptly with doping. As a result, despite Sb coloring having a slightly higher power factor, the thermal conductivity becomes too large and yields a smaller zT value. By treating the electronic thermal conductivity according to the Wiedemann-Franz law, in which the Lorentz number is determined by the Seebeck coefficient,[22] zT can be calculated without knowing the electronic component to the thermal conductivity. The benefit of this approach is that every variable, with the exception of κ_l/τ, can be obtained directly from the band structure.

The large zT found for *n*-type cubic LiZnSb is on a similar scale to the hexagonal polytype (see supporting information for additional operating temperatures and the calculations repeated using PBE for direct comparison with past hexagonal LiZnSb calculations). However, as has been demonstrated for the hexagonal case and other Sb-based Zintl phases, synthesis of these compounds generally yields the *p*-type analogues (likely due to vacancies, as discussed before).[4] This makes the large zT for p-type cubic LiZnSb especially promising.

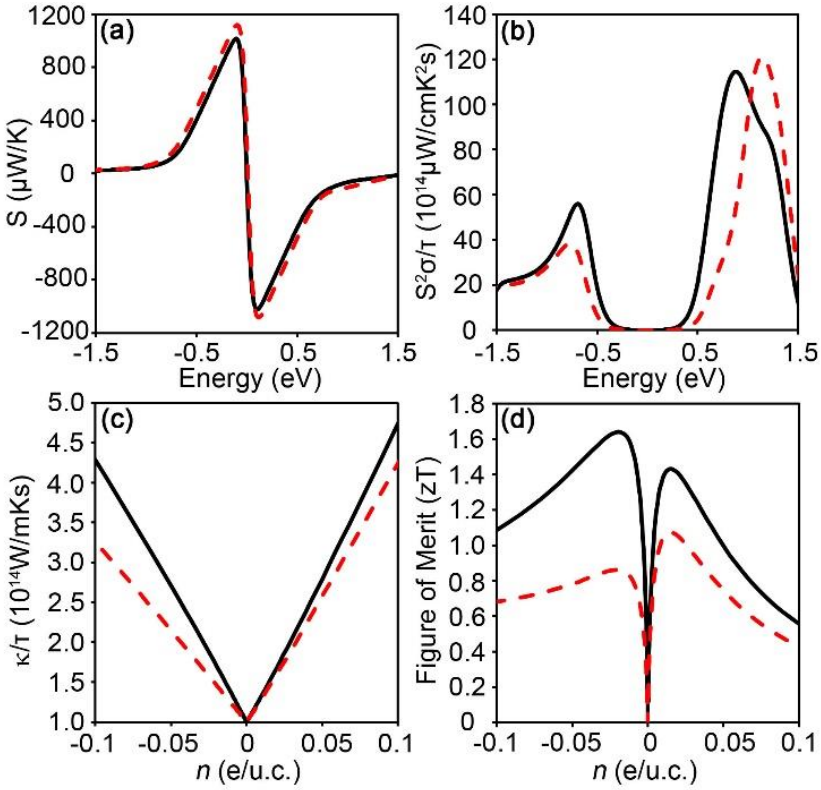

Figure 3. Thermoelectric properties at 600K of cubic LiZnSb calculated using TB-mBJ with both Zn (black, solid) and Sb (red, dashed) occupying the 4c site. Seebeck coefficient (a) and thermopower (b) versus Fermi level have the Fermi level placed directly in the middle of the band gap. Thermal conductivity (c) and zT (d) versus doping are given so that –ve and +ve doping levels correspond to *n*- and *p*-type, respectively.

To calculate zT, a common value of 1×10^{14} W/Kms was assumed for κ_l/τ, which makes a comparison with prior calculations on the hexagonal polytype more straightforward.[3] This assumption agrees well with experimental measurements on *p*-type hexagonal LiZnSb.[4] An added benefit of the solution phase preparation of cubic LiZnSb is the tendency for hot injection methods to give reduced grain size, which causes a reduction in lattice thermal conductivity. This lowering of the lattice thermal conductivity by nanostructuring makes the assumption of $\kappa_l/\tau = 1\times10^{14}$ W/Kms relatively conservative and not overly optimistic.[1] Thus,

combining solution phase synthesis and nanostructuring to reduce the thermal conductivity could keep the extremely high power factor and place cubic LiZnSb among the most efficient thermoelectric materials for both *n*- and *p*- type compositions. Furthermore, its constituent elements and low-temperature synthesis makes LiZnSb promising from both a cost and a toxicity perspective.

Conclusions

In summary, our results address the difficulty in synthesizing *n*-type or even stoichiometric compositions of the suggested hexagonal LiZnSb for thermolelectric applications. Furthermore, by using low-temperature solution phase methods, the first instance of polytypism within Nowotny-Juza phases has been demonstrated. This cubic polytype shows the first example of a group II element occupying the heterocubic site, which has important implications for its band structure and, ultimately, its transport properties. The extremely high power factor of cubic LiZnSb at 600K results in promising zT values for both *n*- and *p*- type doping of over 1.6 and 1.4, respectively. This result uses a conservative estimate for the lattice thermal conductivity, an estimate which can likely be reduced by nanostructuring. We hope that this report sparks additional investigation into the development of cubic LiZnSb for thermoelectric applications.

Acknowledgments

J.V. thanks the U.S. National Science Foundation for a CAREER Grant from the Division of Chemistry, Macromolecular, Supramolecular, and Nanochemistry Program (1253058). Computations were performed on cluster funded by the College of Liberal Arts and Sciences Computational Advisory Committee (LASCAC) at Iowa State University (202- 04-36-03-1000), with additional support from the Chemistry Department.

References

1. Snyder, G. J.; Toberer, E. S. *Nat. Mater.* **2008**, *7*, 105–114.
2. Jain, A.; Shin, Y.; Persson, K. A. *Nat. Rev. Mater.* **2016**, *1*, 15004.
3. Madsen, G. K. H. *J. Am. Chem. Soc.* **2006**, *128*, 12140–12146.
4. Toberer, E. S.; May, A. F.; Scanlon, C. J.; Snyder, G. J. *J. Appl. Phys.* **2009**, *105*, 063701.
5. Andaraarachchi, H. P.; Thompson, M. J.; White, M. A.; Fan, H.-J.; Vela, J. *Chem. Mater.* **2015**, *27*, 8021-8031.
6. White, M. A.; Thompson, M. J.; Miller, G. J.; Vela, J. *Chem. Commun.* **2016**, *52*, 3497–3499.
7. Yeh, C.-Y.; Lu, Z. W.; Froyen, S.; Zunger, A. *Phys. Rev. B* **1992**, *46*, 10086–10097.
8. Kresse, G.; Furthmüller, J. *Comput. Mater. Sci.* **1996**, *6*, 15–50.
9. Kresse, G. *Phys. Rev. B* **1996**, *54*, 11169–11186.
10. Kresse, G. *Phys. Rev. B* **1999**, *59*, 1758–1775.
11. Monkhorst, H. J.; Pack, J. D. *Phys. Rev. B* **1976**, *13*, 5188–5192.
12. Blöchl, P. E. *Phys. Rev. B* **1994**, *50*, 17953–17979.
13. Perdew, J. P.; Burke, K.; Ernzerhof, M. *Phys. Rev. Lett.* **1996**, *77*, 3865–3868.
14. Becke, A. D.; Johnson, E. R. *J. Chem. Phys.* **2006**, *124*, 221101.
15. Tran, F.; Blaha, P. *Phys. Rev. Lett.* **2009**, *102*.
16. Madsen, G. K. H.; Singh, D. J. *Comput. Phys. Commun.* **2006**, *175*, 67–71.
17. Burdett, J. K.; Lee, S.; McLarnan, T. J. *J. Am. Chem. Soc.* **1985**, *107*, 3083–3089.
18. Miller, G. J. *Eur. J. Inorg. Chem.* **1998**, *1998*, 523–536.
19. Bende, D.; Grin, Y.; Wagner, F. R. *Chem. - Eur. J.* **2014**, *20*, 9702–9708.
20. Bende, D.; Wagner, F. R.; Grin, Y. *Inorg. Chem.* **2015**, *54*, 3970–3978.
21. Haas, P.; Tran, F.; Blaha, P. *Phys. Rev. B* **2009**, *79*.
22. Kim, H.-S.; Gibbs, Z. M.; Tang, Y.; Wang, H.; Snyder, G. J. *APL Mater.* **2015**, *3*, 041506.

Appendix of supporting information

Synthesis. Triphenylantimony (Ph_3Sb, 700-750 mg, 2.0 mmol, 97%, Strem) and 1-octadecene (5 mL, 90%/technical grade, Sigma Aldrich) were added to a three-neck flask. The flask was then degassed for 30 min followed by refilling with Ar and heating to 250 °C. *n*-butyllithium (0.125 mL, 0.2 mmol, 1.6 M in hexane, Sigma Aldrich) and diethyl zinc (0.02 mL, 0.2 mmol, 56 wt.% Zn, Sigma Aldrich) were then immediately injected in quick succession. The reaction mixture was heated to 300 °C over the course of 10 min followed by continuous stirring over a 4 h period. The crude product was washed twice with toluene (3-10 mL) and ethanol (5 mL) followed by centrifugation at 5000 rpm for 10 min. *Characterization*. Powder X-ray diffraction (XRD) data were measured using Cu Kα radiation on a Rigaku Ultima IV diffractometer.

$$10\ Ph_3Sb \xrightarrow[\text{ODE}]{\substack{\text{1) n-BuLi, 250 °C} \\ \text{2) } Et_2Zn\text{, 250 °C} \\ \text{3) 300 °C, 4 h}}} LiZnSb + Sb\ \text{(by-product)}$$

Scheme S1. Solution phase synthesis of cubic LiZnSb.

Computational: All VASP calculations used projected augmented-wave (PAW) pseudopotentials with a cutoff energy of 500 eV and a convergence energy of $1x10^{-6}$ eV.[1] A conjugated algorithm was applied to the structural optimization with an 11 x 11 x 11 Monkhorst-pack k-points grid.[2] During structural optimizations, atomic coordinates as well as cell volumes were allowed to relax except for *E*(*V*) curves, during which the cell volume was fixed. For hexagonal volumes, a *c/a* ratio was established based on geometry optimization and then used for *E*(*V*) curves. In the cubic case, this step was not required due to the symmetric lattice parameters. Total energies were calculated using the tetrahedron method with Blöchl corrections applied.[3] VASP calculations treated exchange and correlation by either the local

density approximation (LDA) or the Perdew-Burke-Ernzerhof (PBE)[4] generalized gradient functional in the case of total energy calculations. To estimate accurate gaps from the band structures, the Tran-Blaha modified Becke-Johnson (TB-mBJ) potential was utilized.[5,6] Transport properties were calculated using the rigid-band approximation and constant scattering time approximation as implemented by the BoltzTraP code.[7] For these calculations, a much denser 41 x 41 x 41 k-point grid was used with the TB-mBJ potential due to the importance of an accurate band gap for transport property calculations. Denser k-meshes were used but found to yield similar results.

Table S1. Observed and calculated powder X-ray diffraction reflections for cubic LiZnSb with a lattice parameter of a = 6.23 Å.

Reflection	$2\theta_{meas}$	Measured Relative Intensity (%)	$2\theta_{calc}$	Calculated Relative Intensity (%)
(1 1 1)	24.66	100	24.73	100
(0 2 2)	40.92	68.3	40.94	80.2
(1 1 3)	48.46	40.1	48.42	47.7
(0 0 4)	59.34	13.9	59.28	13.1
(1 3 3)	65.34	13.1	65.22	19.0
(2 2 4)	74.70	16.2	74.56	25.9

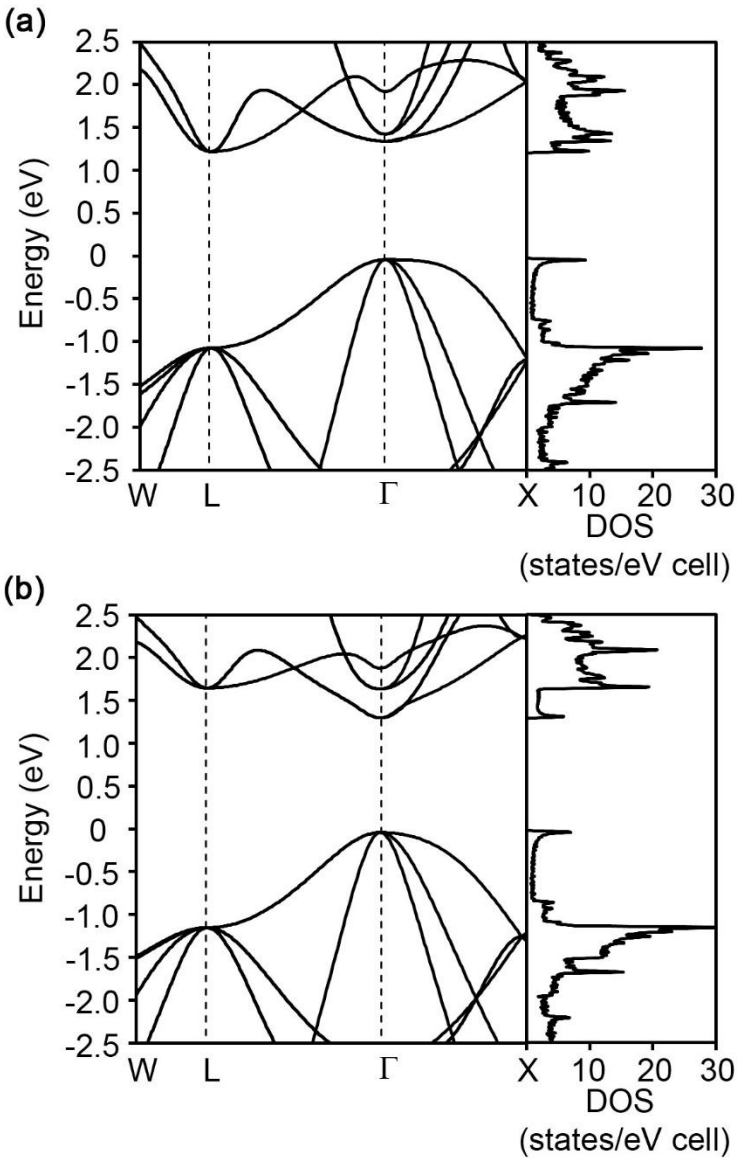

Figure S1. Band structure and density of states of cubic LiZnSb calculated using TB-mBJ with Zn (a) and Sb (b) filling the 4c site (see Figure 2). The site occupancy most notably changes the nature of the band gap from indirect to direct between Zn and Sb, respectively. The maximum valence band also becomes much broader with Zn occupancy.

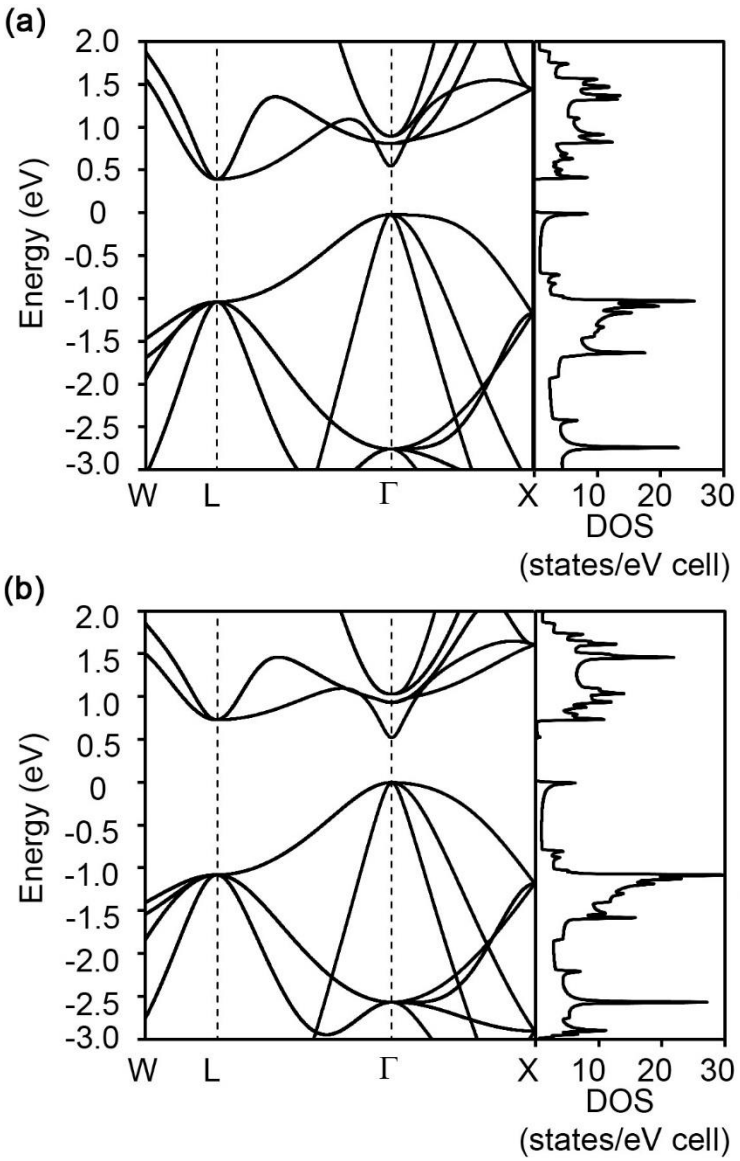

Figure S2. Band structure and density of states of cubic LiZnSb calculated using PBE-GGA with Zn (a) and Sb (b) filling the 4c site. The change in the nature of band gap is the same as with TB-mBJ as is the nature of the maximum valence band.

Table S2. Coloring preference and calculated lattice constant for the cubic Nowotny-Juza phases using local density approximation (LDA). The bolded element in each phase corresponds to the lowest energy coloring pattern. The grey shaded phases (LiZnSb and LiZnBi) remain unreported in the cubic polytype. LDA underestimates the lattice constant by an average of 1.41%, but it accurately predicts the experimentally observed coloring pattern.

Phase	4c site occupancy	ΔE (meV/atom)	a_{exp} (Å)	a_{calc} (Å)	Phase	4c site occupancy	ΔE (meV/atom)	a_{exp} (Å)	a_{calc} (Å)
LiZn**N**	Li Zn **N**	840.6 531.4 **0**	4.88	4.79 4.88 **4.80**	LiCd**P**	Li Cd **P**	326.8 185.7 **0**	6.09	5.79 5.99 **5.98**
LiZn**P**	Li Zn **P**	449.0 10.9 **0**	5.78	5.50 5.58 **5.61**	LiCd**As**	Li Cd **As**	257.8 136.9 **0**	6.26	5.95 6.17 **6.17**
LiZn**As**	Li Zn **As**	359.8 6.6 **0**	5.94	5.67 5.77 **5.81**	**Cu**ZnAs	**Cu** Zn As	**0** 177.4 77.7	5.87	**5.68** 5.73 5.75
LiMg**N**	Li Mg **N**	686.1 707.6 **0**	4.97	4.75 4.94 **4.89**	**Cu**MgSb	**Cu** Mg Sb	**0** 471.0 227.2	6.17	**6.09** 6.27 6.28
LiMg**P**	Li Mg **P**	325.2 340.4 **0**	6.02	5.66 5.92 **5.90**	**Cu**MgBi	**Cu** Mg Bi	**0** 402.8 257.4	6.27	**6.26** 6.41 6.45
LiMg**As**	Li Mg **As**	287.3 292.6 **0**	6.19	5.84 6.08 **6.07**	**Au**CaBi	**Au** Ca Bi	**0** 559.2 282.9	6.85	**6.77** 6.88 6.84
LiMg**Bi**	Li Mg **Bi**	146.5 151.0 **0**	6.74	6.39 6.67 **6.69**	AgZn**As**	Ag Zn **As**	42.5 6.7 **0**	5.91	6.02 5.98 **6.04**
Li**Zn**Sb	Li **Zn** Sb	225.3 **0** 36.4	6.23	6.02 **6.14** 6.23	Li**Zn**Bi	Li **Zn** Bi	203.4 **0** 57.1		6.19 **6.34** 6.41

Table S3. Coloring preference and calculated lattice constant for hexagonal LiZnSb. In this instance, LDA underestimates the lattice constant by 2.03%.						
Phase	2a site occupancy	ΔE (meV/atom)	a_{exp} (Å)	a_{calc} (Å)	c/a_{exp} (Å)	c/a_{calc} (Å)
LiZnSb	**Li** Zn Sb	**0** 213.5 142.2	4.43	**4.34** 4.30 4.39	1.62	**1.62** 1.90 1.91

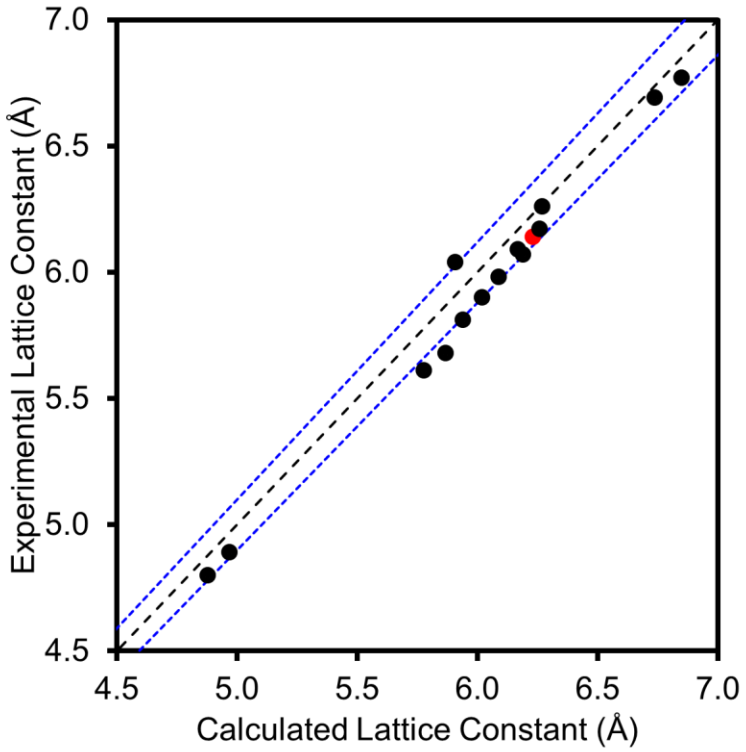

Figure S3. Experimental *vs.* calculated lattice constant (*a*) for cubic Nowotny-Juza phases. Dashed black line corresponds to a perfect match between experiment and computation with the blue lines indicating an under/overestimation of 2%. Previously reported phases are indicated with black markers and cubic LiZnSb is shown in red.

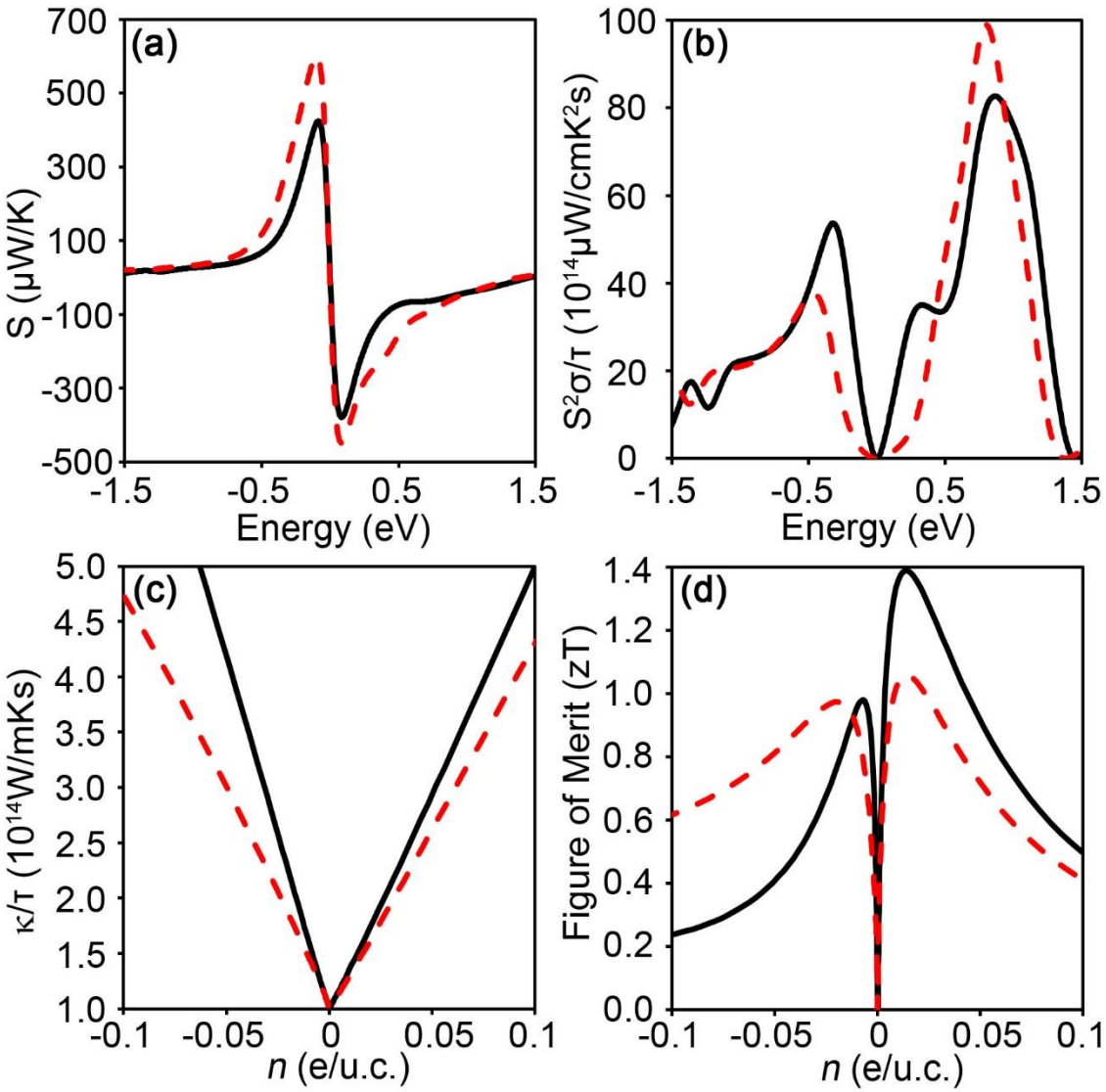

Figure S4. Thermoelectric properties at 600K of cubic LiZnSb calculated using GGA-PBE with both Zn (black) and Sb (red) occupying the 4c site. Seebeck coefficient (a) and thermopower (b) versus Fermi level have the Fermi level placed directly in the middle of the band gap. Thermal conductivity (c) and zT (d) versus doping are given so that –ve and +ve doping levels correspond to *n*- and *p*-type, respectively.

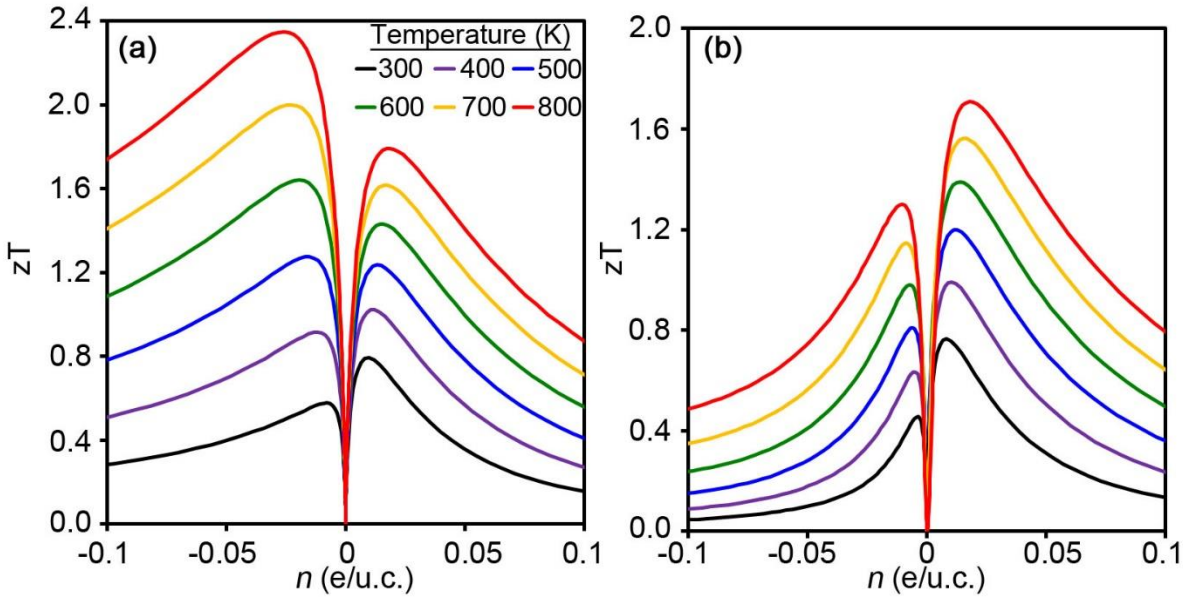

Figure S5. Figure of merit *vs.* carrier concentration as a function of temperature for TB-mBJ (a) and PBE (b).

Supplemental References

1. Kresse, G. *Phys. Rev. B* **1999**, *59*, 1758–1775.
2. Monkhorst, H. J.; Pack, J. D. *Phys. Rev. B* **1976**, *13*, 5188–5192.
3. Blöchl, P. E. *Phys. Rev. B* **1994**, *50*, 17953–17979.
4. Perdew, J. P.; Burke, K.; Ernzerhof, M. *Phys. Rev. Lett.* **1996**, *77*, 3865–3868.
5. Becke, A. D.; Johnson, E. R. *J. Chem. Phys.* **2006**, *124*, 221101.
6. Tran, F.; Blaha, P. *Phys. Rev. Lett.* **2009**, *102*.
7. Madsen, G. K. H.; Singh, D. J. *Comput. Phys. Commun.* **2006**, *175*, 67–71.

CHAPTER 4

EXPANDING THE I-II-V PHASE SPACE: SOFT SYNTHESIS INVESTIGATION OF POLYTYPIC TERNARY AND BINARY ZINC ANTIMONIDES

Manuscript submitted to *Journal of the American Chemical Society*

Miles A. White, Katelyn J. Baumler, Yunhua Chen, Amrit Venkatesh, Alan M. Medina-Gonzalez, Aaron J. Rossini, Julia V. Zaikina, Emory M. Chan, and Javier Vela

Abstract

Soft chemistry methods offer the possibility of synthesizing metastable and kinetic products that are unobtainable through thermodynamically-controlled, high-temperature reactions. A recent solution-phase exploration of Li-Zn-Sb phase space revealed a previously unknown cubic half-Heusler MgAgAs-type LiZnSb. Interestingly, this new cubic phase was calculated to be the most thermodynamically stable, despite prior literature reporting only two other ternary phases (the hexagonal half-Heusler LiGaGe-type LiZnSb, and the full-Heusler Li_2ZnSb). This surprising discovery, coupled with the intriguing optoelectronic and transport properties of many antimony containing Zintl phases, mandates a thorough exploration of synthetic parameters. Here, we systematically study the effects that different precursor concentrations, injection order, nucleation and growth temperatures, and reaction time have on the solution-phase synthesis of these materials. By doing so, we identify conditions that selectively yield six unique ternary (c-LiZnSb, h*-LiZnSb), binary (ZnSb, Zn_8Sb_7), and metallic (Zn, Sb) products. Further, we find one of the ternary phases adopts a variant of the previously observed hexagonal LiZnSb structure. Our results demonstrate the utility of low temperature solution phase—soft synthesis—methods in accessing and mining a rich phase space. We anticipate that this work will motivate further exploration of multinary I-II-V

compounds, as well as encourage other thorough investigations of related Zintl systems by solution phase methods.

Introduction

Classical Zintl phases are valence precise compounds comprised of electropositive and electronegative elements, where the former donate their electrons to the latter, and electronegative elements use these electrons to satisfy octet rule by forming covalent bonds and lone pairs of electrons.[1-3] The electropositive element is either an alkali/alkali earth or rare-earth metal, while the electronegative element is a non-metal, metalloid with the possible incorporation of transition metal.[4] Zintl compounds typically display a covalent anionic sublattice that is permeated by electropositive cations, resulting in a complex crystal structure.[5] For instance, in the 8 electron half-Heusler LiZnSb, Li donates its valence electron to stabilize a covalent zinc-blende $(ZnSb)^-$ network (Figure 1).[6,7] As would be expected due to the similar 8 electron semiconductor network, the same stabilization occurs in a hexagonal LiGaGe-type structure, where Li^+ charge balances the wurtzite $(ZnSb)^-$ sublattice.[8]

Zintl compounds often exhibit complex crystal structures that enable the precise tuning of transport properties by manipulating stoichiometry.[9] The strong correlation between structural and electronic properties have garnered substantial interest from the thermoelectric community.[10-12] Of particular interest are Zintl phases containing Sb and Zn due to their structural diversity and stoichiometric tolerance. For instance, compounds belonging to the AZn_2Sb_2 (A = Ca, Sr, Ba, Eu, Yb) family are stable to both vacancies and substitutions on each crystallographic site.[13,14] In addition to showing potential in thermoelectric applications, these materials often contain elements that are more biocompatible than other state-of-the-art materials that rely on the use of toxic and heavily regulated elements such as Pb as well as more abundant compared to thermoelectric tellurides.[15] However, with many possible

compositions and structures, it becomes challenging to reliably synthesize a target compound in a phase pure manner. Solution phase methods offer increased synthetic control and an avenue to accessing metastable and kinetic products.[11]

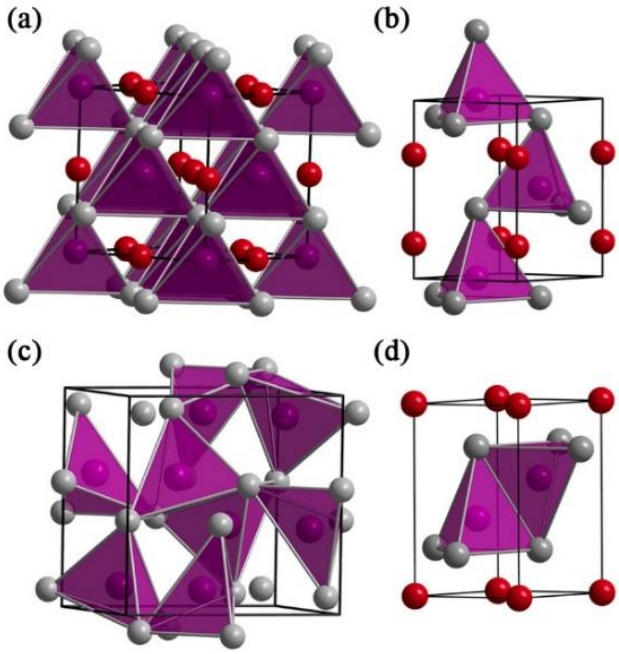

Figure 1. Unit cells and Zn polyhedra highlighting the tetrahedral coordination environments in cubic MgAgAs-type LiZnSb (zinc blende, a), hexagonal LiGaGe-type (wurtzite, b) $CaZn_2Sb_2$-type LiZnSb (extended hexagonal, c) and binary ZnSb (d). Sb is shown in grey, Zn in purple, and Li in red.

A majority of newly discovered crystalline phases are synthesized under thermodynamic control through the use of high-temperature solid-state reactions. However, a vast phase space exists of metastable compounds that are accessible through soft chemistry techniques.[16-19] In particular, low-temperature solution-phase reactions under kinetic control can be tuned to form new phases that are difficult or impossible to target utilizing traditional solid-state chemistry. In this way, metastable polytypes of crystal structures have been successfully synthesized.[20] Until recently, these efforts have been focused primarily on the

control of zinc-blende/wurtzite polytypism within the II-VI and III-V binary semiconductors.[21-26] However, our group successfully expanded this approach to I-II-V ternary semiconductors, where a new cubic half-Heusler structure of LiZnSb was synthesized instead of the previously observed hexagonal structure.[6] As such, the binary and more complex ternary Zintl phases formed from Li, Zn, and Sb are a particularly interesting family of compounds to explore utilizing kinetic control due to their tendency to form complex crystal structures and their large number of potential crystalline products.

Apart from their intriguing structural chemistry, interest in Zn-Sb phases has resurged by the successful synthesis and promising thermoelectric characterization of numerous binaries including Zn_4Sb_3, ZnSb, and Zn_8Sb_7.[27-33] A computationally derived convex hull of formation enthalpies for various binary zinc antimonides predicts ZnSb to have the most negative formation enthalpy.[34] Low-temperature, soft chemistry techniques may provide a reproducible means to observe and isolate many of these phases. Additionally, computational surveys of antimony-based Zintl phases have revealed intriguing ternary compositions such as LiZnSb, $KAlSb_4$, and KSnSb.[35-37] While this class of compounds has already demonstrated incredible structural diversity, very few solution phase syntheses have been reported to date for the binary zinc antimonides.[38-41] Furthermore, there is only one report of a ternary LiZnSb phase prepared from solution.[6] As such, the synthesis of kinetically mediated products is an exciting frontier that remains underexplored. Here, we demonstrate the exploration of this phase space and recognize critical reaction parameters for the control of phase dimensionality. These efforts allow us to identify a previously unreported variant of the ternary LiZnSb structure.

Results and Discussion

Recent exploration of the solution phase synthesis of Zintl zinc antimonides enabled the surprising discovery of cubic LiZnSb (c-LiZnSb). This previously unreported phase is the

first documented example of polytypism in the family of I-II-V half Heusler compounds commonly referred to as Nowotny-Juza phases.[Error! Bookmark not defined.] The synthesis utilized two subsequent hot injections of *n*-butyllithium and diethylzinc into a 1-octadecene solution containing triphenylstibine (Scheme 1). Interestingly, despite prior literature reports of LiZnSb crystallizing in the hexagonal LiGaGe-type (wurtzite) structure (h-LiZnSb), LiZnSb prepared in this manner adopts a cubic, MgAgAs-type (zinc blende) structure (Figure 1). Unfortunately, the first samples prepared by this method contained a significant amount of antimony by-product (Figure 2).[6] To be able to isolate and study the new cubic LiZnSb, and to facilitate its comparison to the better known hexagonal polytype, a more thorough study of the Li-Zn-Sb phase space was warranted. Critically, the large number of possible synthetic parameters—individual precursor concentrations, nucleation (injection) temperature (T_{inj}), growth temperature (T_{grow}), and reaction time (t)—made a traditional 'one-reaction-at-a-time' approach to conditions optimization prohibitively time consuming.

Scheme 1. Soft chemistry exploration of Li-Zn-Sb phase space.

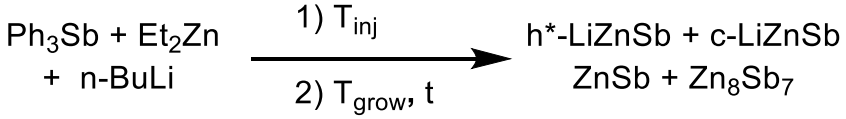

Parallel screening: Optimizing multivariate parameter space. To overcome the task of meticulously exploring a vast number of possible experimental conditions, and to expedite the screening of Li-Zn-Sb phase space, we leveraged the high throughput facilities available in the Molecular Foundry at Lawrence-Berkeley National Laboratory.[42-44] We specifically used the Workstation for Automated Nanomaterials Discovery and Analysis (WANDA), a robot

capable of heating 8 reactors from 30 to 325 °C while providing consistent magnetic stirring. WANDA features two liquid handling robotic arms, which are capable of doing injections as well as withdrawing aliquots during a synthetic operation. Samples prepared using WANDA can then be analyzed by powder X-ray diffraction. In this manner, WANDA offers the combined benefits of greatly accelerated reaction condition screening and an extremely high level of synthetic reproducibility that far exceeds traditional Schlenk techniques.

Selected results from this screening are summarized in Table 1 and Figure 2. The general reaction in Scheme 1 fails to generate any solid products when performed at growth temperatures of 200 °C or lower. Only amorphous solids are isolated after for 4 h at 200 °C, as evidenced by the lack of any clear reflections observable by powder X-ray diffraction. At temperatures above 230 °C, an extended hexagonal $CaZn_2Sb_2$-type LiZnSb (h*-LiZnSb) ternary phase (see discussion below) is observed, which then decomposes into binary ZnSb upon continued heating for longer reaction times (> 2 h). Heating at or above 300 °C quickly results in the formation of metallic antimony, and continued heating for longer reaction times fails to produce additional crystalline products (Table 1).

Table 1. Selected results from parallel synthetic screening.

[Li] (mM)	[Zn] (mM)	[Sb] (mM)	T_{Grow} (°C)	T_{Inj} (°C)	t (h)	Product(s)[a]
40	40	320	260	150	0.5	No rxn.
40	40	320	260	150	1.0	h*-LiZnSb
40	40	320	260	150	4.0	h*-LiZnSb, c-LiZnSb, and ZnSb
40	40	40	260	200	4.0	h*-LiZnSb and Sb
40	40	80	240	200	2.0	h*-LiZnSb
40	40	320	300	200	4.0	Sb
80	40	320	260	150	1.0	Sb
40	80	320	260	150	1.0	h*-LiZnSb
40	80	320	260	150	2.0	h*-LiZnSb and ZnSb
40	40	400	300	250	4.0	c-LiZnSb and Sb

[a]Determined by powder XRD.

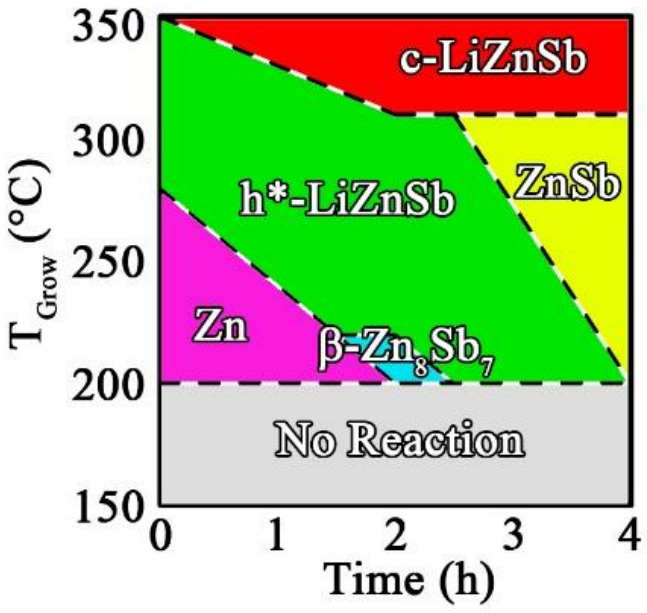

Figure 2. Li-Zn-Sb phase space diagram using the generalized synthesis presented in Scheme 2 with T_{inj} = 150 °C, [Li] = [Zn] = 40 mM, and [Sb] = 160 mM.

We next examined what effects the concentrations of Li, Zn, and Sb precursors would have in dictating the rate as well as the final synthetic outcome of the reaction. Interestingly, varying the Sb precursor concentration appears to be the most useful strategy for determining phase selectivity. At a fixed growth temperature of 260 °C, the use of identical precursor concentrations of [Li] = [Zn] = [Sb] = 40 mM results in no reaction prior to 2h, where the primary product is amorphous antimony. Further heating at 260 °C results in a mixture of elemental Sb and h*-LiZnSb (Table 1). However, increasing the Sb concentration to [Sb] = 80 mM, while keeping other conditions constant results in the formation of the h*-LiZnSb after 2 h followed by the decomposition into ZnSb after 4 h. Further increasing the Sb precursor concentration to either [Sb] = 160 mM or 360 mM causes more rapid formation of h*-LiZnSb, but also eventual decomposition into binary ZnSb. Using [Zn] = 80 mM, [Sb] = 320 mM, and [Li] = 40 mM at 260 °C results in h*-LiZnSb formation after 1 h, and a majority ZnSb phase after 2 h. Increasing the concentration of Li to [Li] = 80 mM causes rapid reduction of triphenylstibine and yields exclusively metallic antimony (Table 1).

Along with growth temperature, reaction time, and precursor concentrations, injection parameters can have a profound effect on resultant products. We find that the order of injection (addition) of precursors does not have any noticeable impact on the reaction. Additionally, the time delay between the injections of *n*-butyllithium and diethylzinc does not change the identity or relative yield of products when a concentration of [Sb] = 80 mM. However, with a higher concentration of [Sb] = 320 mM, a longer delay causes the formation of Sb metal, which is otherwise only observed at higher reaction growth temperatures or higher concentrations of Li. Interestingly, even in this situation, metallic Sb only becomes observable after 4 h reaction. Finally, we also studied the effect of injection temperature. For both T_{inj} = 150 °C and 200 °C,

the same products and relative compositions were observed. Using [Li] = [Zn] = 40 mM, [Sb] = 160 mM, and T_{inj} = 150 °C, a phase space diagram can be constructed (Figure 2).

Selectivity for cubic- *vs.* hexagonal-LiZnSb. Armed with this information, we successfully prepared h*-LiZnSb (see description below and Figure 3). Using [Li], [Zn], and [Sb] concentrations of 40 mM, 40 mM, and 80 mM, respectively, h*-LiZnSb is generated at growth temperatures in the range of 220–310 °C. At low growth temperatures (220 °C), phase pure h*-LiZnSb requires reaction times in excess of 2 h. However, higher growth temperatures (310 °C) result in the formation of this phase in under 10 min.

Through increasing the concentration of Sb above 300 mM, we successfully synthesized c-LiZnSb as well. This phase is always found to form in the presence of an elemental Sb impurity, which is likely caused by the reduction of the unreacted Sb precursor. Phase evolution studies followed by powder XRD show decomposition of h*-LiZnSb into c-LiZnSb (see SI). Interestingly, although c-LiZnSb was not observed when using an injection temperature of 150 °C, the same conditions with an injection temperature of 200 °C caused cubic LiZnSb to form at reaction times longer than 2 h. Therefore, despite a lack of evidence of the cubic phase at early reaction times, the injection temperature still plays a critical role in this reaction at longer reaction times. This result indicates the importance of nucleation kinetics in the Li-Zn-Sb phase space.

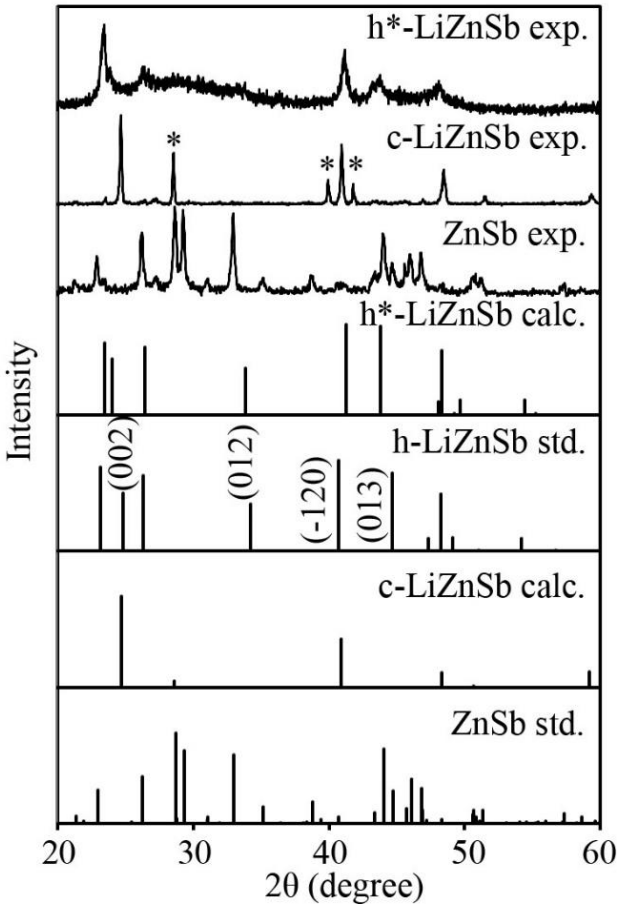

Figure 3. Powder X-ray diffraction patterns of h*-LiZnSb, c-LiZnSb (* = Sb metal impurity), and binary ZnSb. Also shown are the calculated (h*-LiZnSb and c-LiZnSb) and reported (h-LiZnSb and ZnSb) standard patterns (ICSD collection codes 42064 and 43653).

Extended hexagonal LiZnSb. Despite the powder X-ray diffraction pattern of h*-LiZnSb closely resembling the known LiGaGe-type h-LiZnSb, there are some inconsistencies that indicate a deviation from this structure type (Figure 3). Notably, the reflections corresponding to the 002 and 012 planes are substantially suppressed. Additionally, the peak position of the -120 and 013 planes have poor agreement with the experimental pattern and are shifted in opposite directions (-120 is shifted to higher 2θ while 013 is shifted to lower 2θ). These differences can be accounted for by slight changes in lattice parameters; specifically, a 1.4%

suppression in *a* and *b* along with a 3.4% expansion along *c*. A literature survey of compounds that possess a similar *a/c* ratio reveals a large class of ternary zinc antimonides that crystallize in the $CaZn_2Sb_2$-type structure (Figure 4).

The $CaZn_2Sb_2$ structure is a layered variant of the LiGaGe structure type where slabs of tetrahedrally coordinated $[Zn_2Sb_2]^{2-}$ are separated by layers of Ca^{2+}. The structure of this Zintl phase has been thoroughly investigated as a promising thermoelectric material.[45,46] Further, there is ample precedent for all of the crystallographic positions having substantial mixing and disorder. In the case of a ternary phase forming from Li, Zn, and Sb, the most likely site preferences would be Li^+ replacing Ca^{2+} to form the cationic layer while Zn and Sb continue to form the tetrahedral anionic slab.

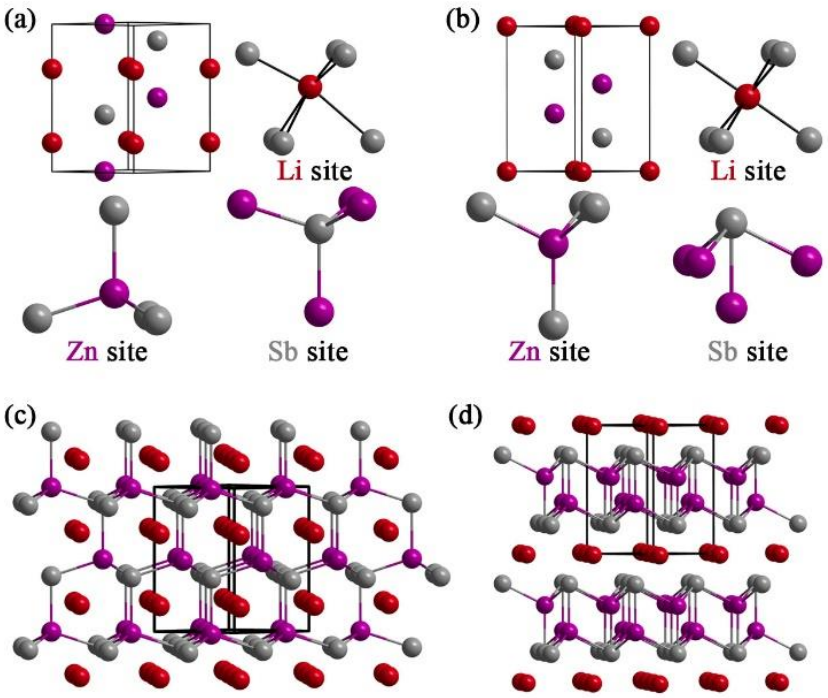

Figure 4. Unit cell and local environments for (a) previously reported h-LiZnSb and (b) h*-LiZnSb. Extended supercell of the two ternary hexagonal structures highlighting the 3D (c) and 2D (d) nature of the tetrahedral [ZnSb] anionic layer.

The $CaZn_2Sb_2$-type has three unique crystallographic sites, one for each element (Figure 4). To properly charge balance, the anionic slab needs to have an overall charge of -1 per unit cell to be compensated by the one Li^+ per unit cell. This can either be achieved through a slightly zinc rich tetrahedral layer of $[Zn_{2.2}Sb_{1.8}]^-$, or through vacancies in the Sb position to give a composition of $[Zn_2Sb_{1.66}]^-$. Additionally, the cationic layer could dope Zn^{2+} into Li^+ sites due to their nearly identical ionic radii (76 pm and 74 pm effective ionic radii for Li^+ and Zn^{2+}, respectively), as in the case of Li_2ZnSb.[47] Likely, these three possibilities could occur in tandem to create a relatively disordered structure.

To probe possible structure, the Vienna Ab Initio Simulation Package (VASP) was used.[48,49] A conjugated algorithm was applied to the structural optimization with an 11×11×11 Monkhorst-Pack *k*-point grid.[50] The theoretical lattice parameters of $LiZn_2Sb_2$, calculated using the LDA, are a = 4.11 Å and c = 7.20. This is slightly smaller (by only 3.0 %) than the experimentally observed lattice constants of a = 4.43 Å and c = 7.40 Å, which agrees well with the typical level of underestimation obtained with LDA for similar systems.[51] Aside from the changes in lattice parameters, no further changes occurred in the local site environments or structure.

Phase evolution: From Zn unary seeds to LiZnSb ternary. To further probe the ternary formation mechanism at a microscopic level, we followed the phase evolution of h*-LiZnSb over time. More specifically, we injected triphenylstibine to a solution of 40 mM Li and 40 mM Zn in ODE/TOP at 240 °C, took small aliquots out of the reaction at different times, and isolated and analyzed the solids produced by XRD, X-ray photoelectron spectroscopy (XPS), and TEM. It is worth noting that this injection of triphenylstibine into a solution of *n*-butyllithium and diethylzinc is opposite what was utilized in the prior synthesis of cubic

MgAgAs-type LiZnSb. We made this modification to increase the reproducibility of the formation of h*-LiZnSb. This is due to the importance of Zn metal as an intermediate in the formation of this phase (see below).

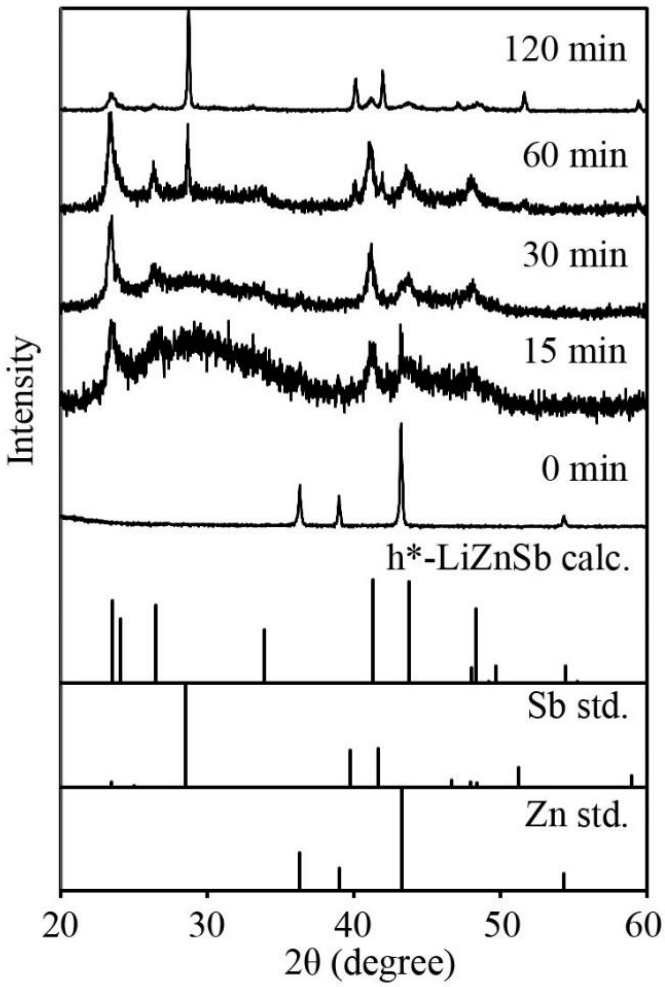

Figure 5. Powder X-ray diffraction of solids isolated after reacting *n*-butyllithium, diethylzinc, and triphenylstibine for different times at 280 °C.

Immediately upon injection, the only crystalline phase present is Zn metal formed from the reduction of diethylzinc by *n*-butyllithium (Figure 5). Over the 15 min after injection, the relative intensity of the reflections corresponding to Zn are reduced until the peaks are no longer visible by 30 min. A large amorphous peak evolves in the first 15 min of the reaction

but is absent at longer time steps. This amorphous phase has a maximum intensity corresponding to the most intense reflection of elemental Sb (2θ = 28.48 degrees). After 12 min reaction, XPS shows the coexistence of three peaks in the Sb $3d_{5/2}$ and $3d_{3/2}$ regions (Figure 6). The most intense peak is located at 528.3 eV and 537.8 eV for $3d_{5/2}$ and $3d_{3/2}$, respectively. This is in good agreement with literature reports of zerovalent Sb and reinforces the assignment of Sb metal as the amorphous product.[52] The additional XPS peaks at higher binding energies correspond to higher oxidation states of +3 and +5. These oxidized phases are likely to be free (unreacted) or surface-bound triphenylstibine (Scheme 3).

While powder XRD and XPS show the presence of amorphous antimony metal, these techniques do not provide information about its spatial proximity or relationship to the initially formed Zn seeds. To investigate this further, we used transmission electron microscopy (TEM) with elemental dispersive X-ray spectroscopy (EDX) (Figure 7). Interestingly, the Zn and Sb are colocalized across particles produced after 12 min instead of phase segregated. The average elemental composition of these particles is 48.4% and 51.6% for Zn and Sb, respectively, which closely matches the anticipated composition of 1:1. Observed lattice fringes correspond to the most intense reflection (011) of Zn (see SI). Further, the rings in the selected area electron diffraction (SAED) of these particles show sharp crystalline peaks that agree with Zn and much more diffuse rings that have a maximum intensity in agreement with the most intense reflection (012) of Sb (see SI).

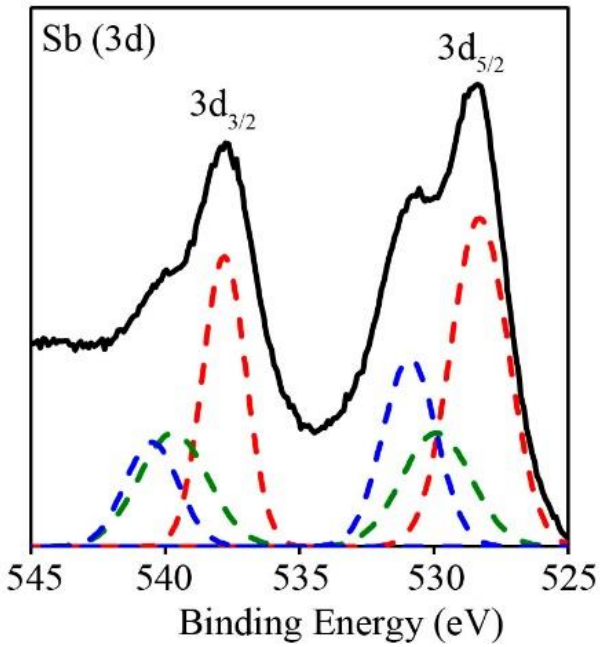

Figure 6. X-ray photoemission spectroscopy at early reaction times (12 min) during the synthesis of h*-LiZnSb at 280 °C. Typical peak positions of Sb^{5+}, Sb^{3+}, and Sb^{0} are given by the dashed blue, green, and red curves, respectively.

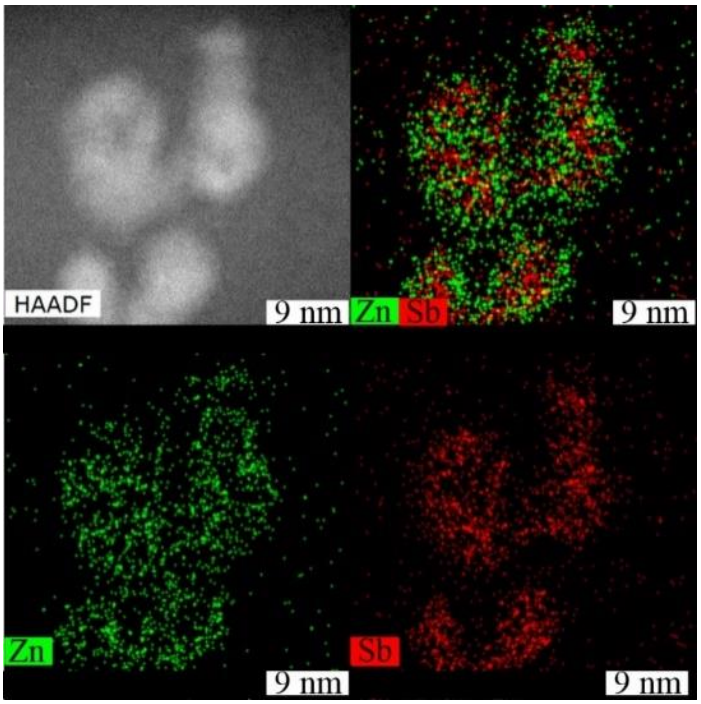

Figure 7. Representative EDX elemental mapping of h*-LiZnSb after 12 min at 280 °C.

These data, coupled with the XRD and XPS above, supports a mechanism that progresses in three steps (Scheme 3). First, Zn seeds are formed by the rapid reduction of diethylzinc from *n*-butyllithium. Second, amorphous Sb surrounds the Zn seeds and, finally, interfacial solid-state diffusion occurs between these domains and results in crystalline h*-LiZnSb. Unfortunately, due to the atomic number threshold of EDX, it is not possible to track the position of the light Li throughout the reaction using this technique. Li is likely either intercalated into the Zn seeds or amorphous Sb. Powder XRD data of the '0 min' sample (removed and isolated immediately upon injection) doesn't show any evidence of a change in lattice constant and the peaks are not substantially broadened, which makes the intercalation of Li into the Zn seeds unlikely. This mechanism is extremely similar to what was observed previously for LiZnP, as well as binary phosphides.[53-60]

Scheme 3. Mechanism of formation h*-LiZnSb.

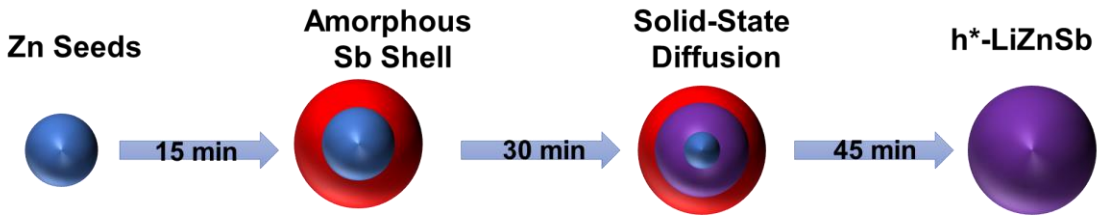

Probing hexagonal- *vs.* cubic-LiZnSb stability. Previous calculations indicated that c-LiZnSb is more thermodynamically stable than its better known hexagonal polytype.[6] Given that solution phase synthesis allowed us to isolate an extended hexagonal (h*-LiZnSb) version of LiZnSb, we sought to determine whether h*-LiZnSb could transform into c-LiZnSb through thermal annealing.

In situ XRD experiments performed on the 17-BM beamline at Argonne National Laboratory's Advanced Photon Source (APS) show similar decomposition pathways for h*-LiZnSb and c-LiZnSb. As expected from the strong 3D covalent $(ZnSb)^-$ zinc-blende sublattice within c-LiZnSb, the thermal stability of this phase is higher than that of the 2D h*-LiZnSb. We observe decomposition of c-LiZnSb at 360 °C *vs.* 240 °C for h*-LiZnSb. Interestingly, a high thermoelectric figure of merit calculated for c-LiZnSb assumed a hot-side temperature in the range of 230-330 °C.[6] Our results indicate that this phase should be stable in this temperature range. Following ternary decomposition, metallic antimony is observed with a minority phase ZnO. Upon reaching 632 °C, Sb melts and ZnO is the only crystalline phase observed. While the major decomposition products of h*-LiZnSb were also Sb and ZnO, a small peak that corresponds to the most intense (111) reflection of c-LiZnSb begins to evolve at 335 °C. This peak becomes more intense with further heating to 632 °C but remains the minority phase with Sb metal being the majority.

In agreement with the beamline study, variable temperature or 'hot-stage' XRD and thermogravimetric analysis (TGA) / differential thermal analysis (DTA) show that heating h*-LiZnSb from room temperature up to 150 °C results in no significant changes (see SI). However, upon reaching 200 °C, amorphous Sb begins to crystallize. This corresponds well to an exothermic transition observed by DTA at 204 °C. Additionally, h*-LiZnSb decomposes by 250 °C. Further heating does not evolve any more phases. Elemental antimony is observed until its melting point, which coincides with a large endothermic transition in the DTA at 633 °C.

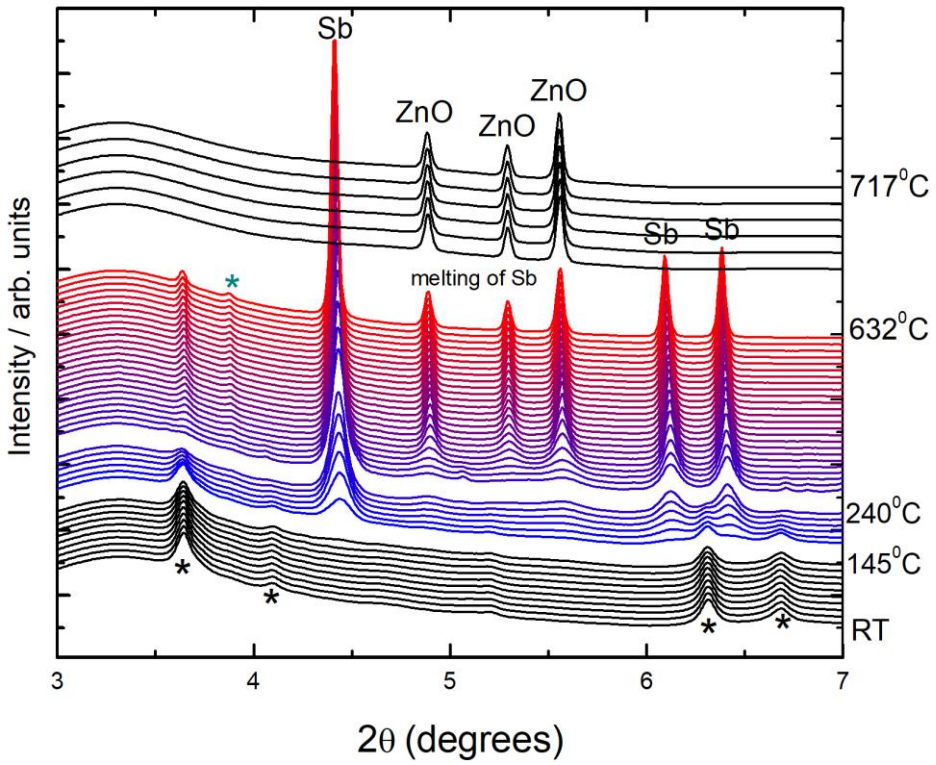

Figure 8. Variable temperature powder X-ray diffraction of h*-LiZnSb collected with a heating rate of 15 °C/min on 17-BM at APS from room temperature up to 717 °C. Only h*-LiZnSb (peak positions is labeled with black *) is observed until 145 °C, where Sb begins to crystallize. h*-LiZnSb (black *) has completely decomposed by 240 °C where Sb and ZnO are the primary crystalline components. After the melting of Sb at 632 °C, only ZnO is observed. The single peak attributed to c-LiZnSb is denoted a s green *.

Synthetic control of phase dimensionality: Ternary *vs.* binary (Li)-Zn-Sb. Upon exploring longer reaction times and higher antimony concentrations, we have successfully synthesized ZnSb from solution (Figure 3). The evolution of ZnSb appears at times greater than 2 hours for samples of h*-LiZnSb. This result is consistent with the observation of low thermal stability (see above) of h*-LiZnSb. While ZnSb begins to be seen as a decomposition product when [Sb] = 80 mM and [Zn] = [Li] = 40 mM, when [Sb] > 160 mM, it becomes the majority

crystalline phase. Furthermore, extending reaction times beyond four hours results in phase pure ZnSb.

While ZnSb is commonly observed as the decomposition product, the concentration of Zn and Li dictates whether ZnSb or cubic LiZnSb forms. When [Zn] = [Li] = 40 mM, cubic LiZnSb begins to be visible by PXRD after 4 hours at 260 °C. While for [Zn] = 80 mM and [Li] = 40 mM, no cubic LiZnSb is observed at any time step and instead the majority phase present is ZnSb. This observation provides additional evidence for the existence of h*-LiZnSb which possesses layered tetrahedral slabs.

ZnSb adopts an orthorhombic crystal structure with one unique crystallographic position for both Zn and Sb (Figure 1). The coordination around Zn is a distorted tetrahedron of Sb, whereas, the Sb local environment is a square pyramid comprised of four Zn and one Sb. These local environments and composition mimic the 2D tetrahedral layers contained within h*-LiZnSb that we observe. As such, it appears that longer reaction times lead to leaching of the cationic Li layers which results in the formation of ZnSb. This leaching can be inhibited through the presence of excess lithium in solution which is consistent with the observation that the decomposition product at higher Li concentrations is c-LiZnSb.

All the binary zinc antimonides show high thermoelectric figure of merit; however, the thermoelectric performance of ZnSb is limited by its high thermal conductivity which is consistent with its relatively simple crystal structure.[61,62] This low temperature facile synthesis of ZnSb is useful as a means of reducing the thermal conductivity. By utilizing solution phase methods there is a high propensity for a reduction in grain size or nanostructuring to occur, which has been shown to effectively reduce thermal conductivity.[63-65] Furthermore, for large scale applications, a fast and facile synthesis using non-toxic elements is required.[66]

When lower reaction times are utilized (215 °C), an unidentified crystalline product forms (see SI). The most intense reflections correspond to β-Zn_8Sb_7. However, relative intensities of the reflections are not in good agreement with the standard pattern. This could be due to anisotropic growth, varying composition, or a crystallographic difference. Further exploration will be necessary to characterize this compound.

Characterization of LiZnSb using solid state NMR. MAS ^{1}H spin echo NMR spectra show distinct peaks which could be assigned to triphenylstibine (Ph_3Sb) and 1-octadecene (ODE) (see SI). This result is further confirmed by ^{1}H-^{13}C cross polarization (CP) spectra, which show the presence of two carbonaceous species: Ph_3Sb and ODE (see SI). In order to get a better understanding of the relative spatial proximity of Ph_3Sb and ODE, we acquired ^{1}H double quantum – single quantum (DQ-SQ) 2D spectra (Figure 9 and Figure S18). The presence of a peak in the DQ-SQ spectrum indicates that two ^{1}H nuclei are in close spatial proximity. The chemical shift in the indirect DQ dimension (δ_{DQ}) is determined by the sum of the two SQ chemical shifts (δ_{SQ}) that generate the DQ coherence. Therefore, the signals along the diagonal are due to aggregation of similar species, while off-diagonal intensities indicate that some Ph_3Sb and ODE are in close spatial proximity. For example, the 1-octadecene peak at *ca.* δ_{SQ} = 0.9 ppm and the Ph_3Sb peak at *ca.* δ_{SQ} = 7.3 ppm show a cross-peak at *ca.* δ_{DQ} = 8.2 ppm (highlighted by the horizontal red line in Figure 9), indicating the close spatial proximity of some of these species on the surface.

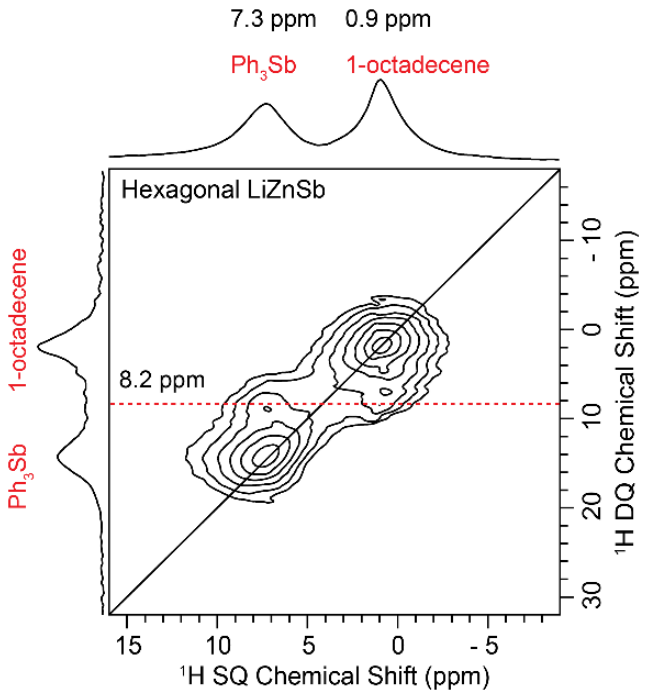

Figure 9. 2D dipolar double quantum–single quantum (DQ-SQ) correlation spectrum of h*-LiZnSb obtained using BABA dipolar recoupling.

Proton detected dipolar – refocused insensitive nuclei enhanced by polarization transfer (D-RINEPT) solid-state NMR experiments can selectively observe half-integer quadrupolar nuclei that are in close spatial proximity (dipolar coupled) to protons. For h*-LiZnSb, there are unlikely to be protons in the bulk of the material Therefore, the 2D ^{7}Li→^{1}H D-RINEPT spectra are surface-selective and show spatially proximate surface ^{7}Li sites and ^{1}H of both Ph_3Sb and ODE(Figure 10). A comparison between the positive projections of the 2D D-RINEPT HETCOR spectra along the ^{7}Li dimension and ^{7}Li spin echo spectra show identical line shapes and linewidths for both spectra. However, surface ^{7}Li nuclei show longer longitudinal relaxation times compared to bulk ^{7}Li (Figure 11). This may be attributed to the presence of a highly passivated surface with perfectly coordinated ligands, while the inside of the particles may contain defects, leading to slightly shorter T_1 (see below).

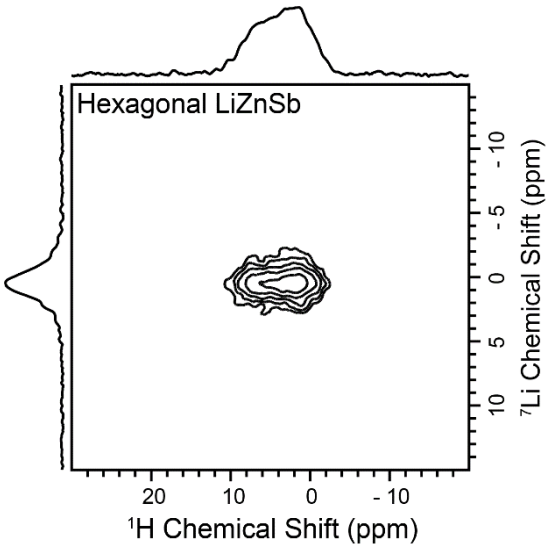

Figure 10. Surface-selective ^{1}H detected 2D ^{7}Li→^{1}H D-RINEPT of h*-LiZnSb. The appearance of through space cross-correlation peaks between Li and H indicates the surface environment of LiZnSb.

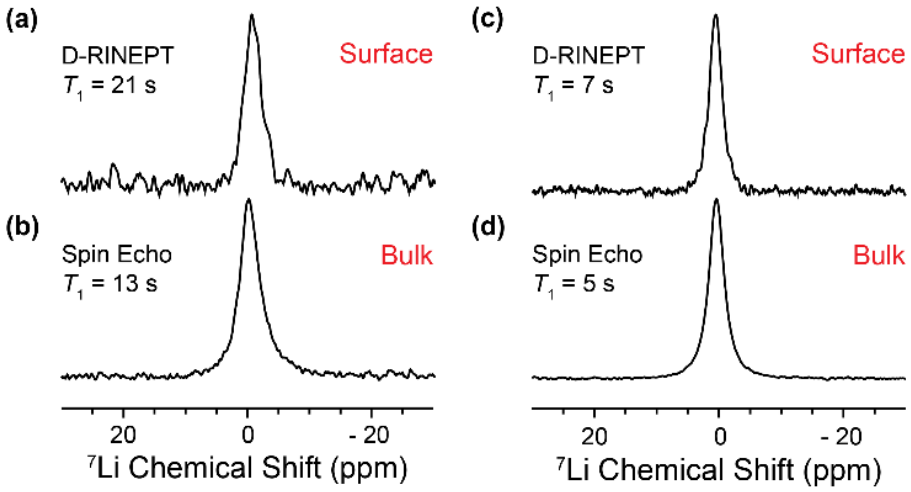

Figure 11. Comparison of the ^{7}Li spin echo spectra and positive projections of the ^{7}Li dimension from the 2D ^{7}Li→^{1}H D-RINEPT spectra for cubic MgAgAs-type LiZnSb (a, b) and h*-LiZnSb (c, d). ^{7}Li spin echo spectra show all Li chemical environments. ^{7}Li-^{1}H D-RINEPT involve magnetization transfer between ^{7}Li and ^{1}H, which only involves surface lithium sites.

Finally, we sought to use ssNMR to probe the local coordination environment around Sb. Antimony has two NMR active isotopes: ^{121}Sb and ^{123}Sb. Based on its higher natural abundance (57.2%) and smaller nuclear quadrupole moment (-54.3±1.1 fm^2), the former is more amenable to ssNMR. For example, the ^{121}Sb ssNMR spectrum of $KSb(OH)_6$ at 21.14 T using the WURST-QCPMG and quadrupolar echo pulse sequences was reported, with an overall central transition linewidth of *ca.* 450 kHz.[2] However, even compounds with high, near-tetrahedral or octahedral symmetry can show broad ^{121}Sb ssNMR spectra. In fact, electric field gradient (EFG) parameters of various antimony-based compounds calculated using CASTEP[67] predict very large ^{121}Sb quadrupole coupling constants (C_Q). A large C_Q results in very broad ^{121}Sb ssNMR spectra, and often hampers both acquisition and interpretation. The calculated C_Q of cubic LiZnSb is zero, as expected for a perfect, spherically symmetric charge distribution in a cubic space group. However, the static ^{121}Sb ssNMR spectrum of cubic LiZnSb at 9.4 T shows a single site with an unexpectedly large C_Q of 74 MHz. The substantial difference between the calculated and experimental C_Q values implies that there must be homogenously distributed impurities or defects, likely arising from multiple coloring patterns or superstructures, that must be present and result in a sizable electric field gradient and C_Q for ^{121}Sb.[6,68]

Conclusion

In summary, we have explored the diverse phase space generated from the solution-phase reaction between triphenylstibine, *n*-butyllithium, and diethylzinc. Depending on reaction time and temperature, we are able to selectively synthesize six different crystalline phases: Zn, Sb, ZnSb, Zn_8Sb_7, extended h-LiZnSb, and c-LiZnSb. A previously unreported $CaZn_2Sb_2$-type ternary, extended hexagonal LiZnSb is a layered variant of the hexagonal LiGaGe-type LiZnSb seen from high temperature reactions. Antimony concentration and

temperature are the main factors affecting the selectivity between hexagonal $CaZn_2Sb_2$-type and cubic MgAgAs-type LiZnSb (the latter is formed at higher Sb concentrations and higher growth temperatures). Using a combination of powder XRD, XPS, and EDX, we studied the phase evolution of $CaZn_2Sb_2$-type LiZnSb, and identified a mechanism for its formation. Using high temperature diffraction experiments, we find that cubic MgAgAs-type LiZnSb is more thermodynamically stable than $CaZn_2Sb_2$-type LiZnSb. Further, the latter appears to transition to MgAgAs-type c-LiZnSb upon heating.

A staple of crystalline semiconductors prepared by low-temperature solution-phase or soft chemistry methods is the presence of surface passivating ligands. Using solid state (ss) NMR, we have identified the presence of ODE and Ph_3Sb on the surface of both cubic MgAgAs-type and $CaZn_2Sb_2$-type LiZnSb particles. Additionally, ssNMR confirms the presence of Li within these crystals. Finally, ssNMR supports multiple coloring patterns or superstructures are present in the cubic MgAgAs-type structure. In conclusion, the Li-Zn-Sb phase space appears to be extremely rich with many promising thermoelectric materials already revealed. We hope that this report sparks additional investigation into the solution phase synthesis and optimization of binary and ternary zinc antimonides.

Experimental

Materials. 1-octadecene (ODE, technical grade, 90%), diethylzinc (Et_2Zn, 56 wt. % Zn), and *n*-butyllithium (*n*-BuLi, 1.6 M in hexane) were purchased from Sigma; triphenylstibine (Ph_3Sb, 97%) and tri-*n*-octylphosphine (TOP, 97%) were purchased from Strem. All chemicals were used as received. Stock solutions were made with ODE as the solvent with concentrations of 0.8 M, 0.4 M, and 0.4 M for Ph_3Sb, *n*-BuLi, and Et_2Zn, respectively.

Synthesis. In a general synthesis, x mL 0.4 M *n*-BuLi in ODE (x = 0.5–2) and y mL 0.4 M Et_2Zn in ODE (y = 0.5 -2) were added to a three-neck flask containing (7 – x – y – z) mL ODE

and 3 mL tri-n-octylphosphine (TOP, 97% Strem) at 120 °C which had been degassed for 30 min. The flask was then heated to 240 °C and held for 15 min to crystallize zinc seeds. Next, z mL 0.8 M Ph_3Sb in ODE (z = 0.5 – 4) was injected and the reaction mixture was heated to the reaction temperature and held for the reaction time. The crude product was washed twice with toluene (3-10 mL) and ethanol (5 mL) followed by centrifugation at 5000 rpm for 10 min. *Synthesis of h*-LiZnSb ternary.* 3 mL TOP and 4 mL ODE were heated to 120 °C under Ar followed by injection of a mixture of 1 mL 0.4 M *n*-BuLi and 1 mL 0.4 M Et_2Zn in ODE. The reaction was then heated and held at 240 °C for 15 min. Next, 1 mL 0.8 M was injected and the reaction mixture was heated to 280 °C and held for 30 min. *Synthesis of c-LiZnSb ternary*. A mixture of 1 mL 0.4 M *n*-BuLi and 1 mL 0.4 M Et_2Zn in ODE was injected into a three-neck flash containing 3 mL TOP and 4 mL ODE at 120 °C. The reaction was heated to 240 °C and held for 15 min followed by heating to 310 °C. 0.5 mL 0.8 M Ph_3Sb in ODE was injected into the flask and the reaction was held at 310 °C for 2 h. *Synthesis of ZnSb binary.* 5 mL 0.8 M Ph_3Sb in ODE and 3 mL TOP were heated to 185 °C followed by the injection of a mixture of 1 mL 0.4 M Et_2Zn and 1 mL 0.4 M *n*-BuLi in ODE. This reaction mixture was then heated to 220 °C and held for 4 h.

Characterization. Powder X-ray diffraction (PXRD) data were measured using Cu Kα radiation on a Rigaku Ultima IV diffractometer. Transmission electron microscopy (TEM) and energy dispersive spectroscopy (EDX) were conducted on carbon-coated copper grids using a FEI Titan Themis Cubed Aberration Corrected Scanning Transmission Electron Microscope.

XPS. The X-ray photoemission spectroscopy (XPS) measurements were performed using a Kratos Amicus/ESCA 3400 instrument. The sample was irradiated with 240 W non-monochromated Mg Kα x-rays, and photoelectrons emitted at 0° from the surface normal were

energy analyzed using a DuPont type analyzer. The pass energy was set at 75 eV. CasaXPS was used to process raw data files.

Hot-Stage XRD. Variable temperature PXRD was conducted using a Panalytical X'Pert Pro MPD system fitted with an Anton Paar HTK1200N furnace and an X'Celerator detector. Diffraction measurements with Cu-K_α radiation were taken at temperature steps from 25°C to 550 °C. The sample was heated to the specified temperature and held during the measurement under flowing helium.

Variable temperature synchrotron powder XRD data were collected at the synchrotron beamline: 17-BM at the Advanced Photon Source (APS) at Argonne National Lab (ANL). The samples of LiZnSb were loaded into silica capillaries (0.5 mm inner diameter; 0.7 mm outer diameter) and sealed under vacuum. The sealed silica capillaries were placed inside a secondary shield capillary in the flow furnace, with a thermocouple set as close as possible to the end of the inner silica capillary.[69] The data were collected with $\lambda = 0.24128$ Å on heating from room temperature to ~700°C and on cooling; with the heating rate of 10-15 deg. C/min, and 20 deg .C /min for cooling. Diffraction data were collected continuously with 1-min collection times. The temperature calibration was applied by comparing the tabulated melting points of the elemental Sn, Sb, Ge with the temperatures, when the diffraction peaks of elemental Sn, Sb, Ge disappear (e.g. melting).

TGA-DTA. Thermal analysis was conducted using a TA Instruments SDT 2960 (simultaneous DTA-TGA). The apparatus has a micro-balance sensitivity of 0.1 micro-grams and temperature sensitivity (for DTA) of 0.001^0C. The apparatus can be used to study material transformations over a temperature range from ambient to 1500^0C. The experiments were conducted in a nitrogen atmosphere (dynamic, flow rate = 100ml/min), from ambient to 690^0C

at a scanning rate of 5^0C/minute. The experiments were conducted with alumina sample pans (size = 90 micro-liter). Calcined alumina was used in the reference pan. A nominal sample size of 20 mg was used for this study.

Solid-state NMR. All moderate-field [B_0 = 9.4 T, $\nu_0(^1H)$ = 400.5 MHz, $\nu_0(^7Li)$ = 155.6 MHz, $\nu_0(^{13}C)$ = 100.7 MHz, $\nu_0(^{121}Sb)$ = 95.8 MHz] solid-state (ss) NMR experiments were performed on a Bruker Avance III HD spectrometer with a wide-bore magnet. A Bruker 1.3 mm HX double resonance MAS probe was used to perform all fast-MAS experiments at a spinning rate (ν_{rot}) of 45 kHz. ^{1}H NMR shifts were referenced to neat Tetramethylsilane using adamantane ($\delta_{iso}(^1H)$ = 1.82 ppm) as a secondary chemical shift standard. Previously published relative NMR frequencies[70] were used to indirectly reference ^{7}Li, ^{13}C and ^{121}Sb chemical shifts. All experiments were performed using optimum recycle delays of 1.3 × T_1; the recycle delays and number of scans of all experiments are listed in the SI. All the NMR spectra were processed in Topspin 4.0.

^{1}H ssNMR. ^{1}H MAS NMR spectra were acquired using a Hahn echo sequence; all NMR experiments were performed with 2.5 μs and 5 μs π/2 and π pulses respectively on the ^{1}H channel. ^{1}H radiofrequency (RF) fields were calibrated directly on each sample using a π/2-spin-lock pulse sequence to find the 2nd order rotary resonance recoupling (R^3) conditions (2 × π_{rot}).[71] ^{1}H DQ-SQ 2D spectra were acquired using the BABA recoupling method[72] with a one rotor cycle duration each for DQ excitation and reconversion, and π/2 pulse lengths of 2.5 μs.

^{7}Li ssNMR. ^{7}Li MAS NMR spectra were acquired using a Hahn-echo sequence with central transition (CT) selective π/2 and π pulses lengths of 1.5 μs and 3 μs respectively. ^{1}H detected ^{7}Li→^{1}H D-RINEPT spectra were obtained with a short recoupling time of 6 rotor cycles per recoupling block for near-surface characterization. The T_1 of the surface ^{7}Li sites

were obtained using the ^{1}H detected ^{7}Li→^{1}H D-RINEPT pulse sequence with an additional saturation recovery block before the D-RINEPT transfer block.[73]

^{13}C ssNMR. ^{1}H detected ^{1}H{^{13}C} CP-HETCOR and direct detected ^{1}H→^{13}C CP spectra were acquired using spin-lock RF fields of *ca.* 125 kHz and 80 kHz on the ^{1}H and ^{13}C channels respectively, and a ^{13}C $\pi/2$ pulse length of 2.5 μs. The ^{1}H spin-lock RF fields were optimized directly on the samples with a fixed ^{13}C spin-lock RF field to meet the Hartmann-Hahn CP match conditions. 80%-100% amplitude ramped spin-lock pulses were employed for the ^{1}H spin-lock during all CP experiments. Heteronuclear ^{1}H decoupling was applied at a RF field of 22.5 kHz ($0.5 \times \nu_{rot}$) for the ^{7}Li and ^{13}C experiments.

^{121}Sb ssNMR. The ^{121}Sb static NMR spectrum was acquired using the QCPMG pulse sequence by the piece-wise frequency-stepped acquisition technique with a step-size of 250 kHz, spanning a total spectral width of *ca.* 14 MHz.[74] Each QCPMG spectrum was acquired with a spectral window of 2 MHz and an echo train comprising of 20 echoes of 20 □s duration each. The simulated ^{121}Sb spectrum was generated using QUEST[75] with the EFG parameters showed in the SI. The CASTEP[76] program was used to calculate ^{121}Sb electric field gradient (EFG) tensor parameters of a list of antimony-based compounds according to the previous reported calculation procedure, using the Materials Studio 2017 R2 environment (see SI).[77] All calculations used the Perdew-Burke-Ernzerhof (PBE)[78] generalized gradient approximation functional with the Tkatchenko-Scheffler dispersion correction[79] and ultra-soft pseudopotentials generated *on-the-fly*. All atomic positions were optimized and P_1 symmetry was imposed on the unit cell prior to performing the NMR calculations. The NMR calculations were performed using the GIPAW method implemented in CASTEP.[80,81]

Calculations. All VASP calculations used projected augmented-wave (PAW) pseudopotentials with a cutoff energy of 500 eV and a convergence energy of $1x10^{-6}$ eV.[82] A conjugated algorithm was applied to the structural optimization with an 11 x 11 x 11 Monkhorst-pack k-points grid.[50] During structural optimizations, atomic coordinates as well as cell volumes were allowed to relax. Total energies were calculated using the tetrahedron method with Blöchl corrections applied.[83] VASP calculations treated exchange and correlation by either the local density approximation (LDA) or the Perdew-Burke-Ernzerhof (PBE) generalized gradient functional in the case of total energy calculations. Denser k-meshes were used but found to yield similar results.

Acknowledgement

J. V. thanks the U.S. National Science Foundation for a CAREER grant from the Division of Chemistry, Macromolecular, Supramolecular, and Nanochemistry Program (1253058). Y.C., A.V. and A.J.R. were supported by the U.S. Department of Energy (DOE), Office of Science, Basic Energy Sciences, Materials Science and Engineering Division. Electron microscopy was performed at the Sensitive Instrument Facility of Ames Laboratory. The Ames Laboratory is operated for the U.S. DOE by Iowa State University under contract # DE-AC02-07CH11358. The authors thank the Molecular Foundry at Lawrence-Berkeley National Laboratory for access to the robotic synthesis user facility (4398). Work at the Molecular Foundry was supported by the Office of Science, Office of Basic Energy Sciences, of the U.S. Department of Energy under Contract No. DE-AC02-05CH11231. Use of the Advanced Photon Source at Argonne National Laboratory was supported by the U. S. Department of Energy, Office of Science, Office of Basic Energy Sciences, under Contract No. DE-AC02-06CH11357. The authors thank Gordie Miller for insightful discussions.

References

1. Kauzlarich, S. M.; Brown, S. R.; Snyder, G. J. *Dalton Trans.* **2007**, 2099-2107.

2. *Chemistry, Structure, and Bonding of Zintl Phases and Ions*; Kauzlarich, S. M., Ed.; VCH Publishers Inc., New York, 1996

3. *Zintl Phases: Principles and Recent Developments*, Book Series: *Structure and Bonding*; Fässler, T. F., Ed.; Volume 139, Springer, Heidelberg, 2011.

4. Nesper, R. Prog. Solid. State Chem. **1990**, 20, 1-45.

5. Zevalkink, A.; Zeier, W. G.; Pomrehn, G.; Schechtel, E.; Tremel, W.; Snyder, G. J. *Energy Environ. Sci.* **2012**, *5*, 9121-9128.

6. White, M. A.; Miller, G. J.; Vela, J. *J. Am Chem. Soc.* **2016**, *138*, 14574-14577.

7. Zeier, W. G; Schmitt, J.; Hautier, G.; Aydemir, U.; Gibbs, Z. M.; Felser, C.; Snyder, G. J. *Nat. Rev. Mater.* **2016**, *1*, 16032.

8. White, M. A.; Medina-Gonzalez, A. M.; Vela, J. *Chem. Eur. J* **2017**, *24*, 3650-3658.

9. Gascoin, F.; Ottensmann, S.; Stark, D.; Haile, S. M.; Snyder, G. J. *Adv. Funct. Mater.* **2005**, *15*, 1860-1864.

10. Toberer, E. S.; May, A. F.; Snyder, G. J. *Chem. Mater.* **2010**, *22*, 624-634.

11. Biswas, K.; He, J.; Blum, I. D.; Wu, C.-I.; Hogan, T. P.; Seidman, D. N.; Dravid, V. P.; Kanatzidis, M. G. *Nature* **2012**, *489*, 414-418.

12. Brown, S. R.; Kauzlarich, S. M.; Gascoin, F.; Snyder, G. J. *Chem. Mater.* **2006**, *18*, 1873-1877.

13. Zevalkink, A.; Zeier, W. G.; Cheng, E.; Snyder, J.; Fleurial, J.-P.; Bux, S. *Chem. Mater.* **2014**, *26*, 5710-5717.

14. Wang, X.-J. *Appl. Phys. Lett.* **2007**, *90*, 232107.

15. Bjerg, L.; Madsen, G. K. H.; Iversen, B. B. *Chem. Mater.* **2011**, *23*, 3907-3914.

16. Men, L.; White, M. A.; Andaraarachchi, H.; Rosales, B. A.; Vela, J. *Chem. Mater.* **2017**, *29*, 168-175.

17. Uppuluri, R.; Gupta, A. S.; Rosas, A. S.; Mallouk, T. E. *Chem. Soc. Rev.* **2018**, *47*, 2401-2430.

18. Seisenbaeva, G. A.; Kessler, V. G. *Nanoscale* **2014**, *6*, 6229-6244.

19. Schaak, R. E.; Mallouk, T. E. *Chem. Mater.* **2002**, *14*, 1455-1471.

20. Martinolich, A. J.; Kurzman, J. A.; Neilson, J. R. *J. Am. Chem. Soc.* **2015**, *137*, 3827-3833.

21. Assali, S.; Gagliano, L.; Oliveira, D. S.; Verheijen, M. A.; Plissard, S. R; Feiner, L. F.; Bakkers, E. P. A. M. *Nano Lett.* **2015**, *15*, 8062-8069.

22. Mahler, B.; Lequeux, N.; Dubertret, B. *J. Am. Chem. Soc.* **2010**, *132*, 953-959.

23. Nan, W.; Niu, Y.; Qin, H.; Cui, F.; Yang, Y.; Lai, R.; Lin, W.; Peng, X. *J. Am. Chem. Soc.* **2012**, *134*, 19685-19693.

24. Johansson, J.; Dick, K. A.; Caroff, P.; Messing, M. E.; Bolinsson, J.; Deppert, D.; Samuelson, L. *J. Phys. Chem. C.* **2010**, *114*, 3837-3842.

25. Joyce, H. J.; Wong-Leung, J.; Gao, Q.; Tan, H. H.; Jagadish, C. *Nano Lett.* **2010**, *10*, 908-915.

26. Karan, N. S.; Sarkar, S.; Sarma, D. D.; Kundu, P.; Ravishankar, N.; Pradhan, N. *J. Am. Chem. Soc.* **2011**, *133*, 1666-1669.

27. Caillat, T.; Fleurial, J. P; Borshchevsky, A. *J. Phys. Chem. Solids* **1997**, *58*, 1119-1125.

28. Zhang, L. T.; Tsutsui, M.; Ito, K.; Yamaguchi, M. *J. Alloy Compd.* **2003**, *358*, 252-256.

29. Pothin, R.; Ayral, R. M.; Berche, A.; Dranier, D.; Rouessac, F.; Jund, P. *Chem. Eng. J.* **2016**, *299*, 126-134.

30. Wang, J.; Kovnir, K. *J. Am. Chem. Soc.* **2015**, *137*, 12474-12477.

31. Lin, J.; Li, X.; Qiao, G.; Wang, Z.; Carrete, J.; Ren, Y.; Ma, L.; Fei, Y.; Yang, B.; Lei, L.; Li, J. *J. Am. Chem. Soc.* **2014**, *136*, 1497-1504.

32. Mozharivskyj, Y.; Janssen, Y.; Harringa, J. L.; Kracher, A.; Tsokol, A. O.; Miller, G. J. *Chem. Mater.* **2006**, *18*, 822-831.

33. Snyder, G. J.; Christensen, M.; Nishibori, E.; Caillat, T.; Brummerstedt, I. *Nat. Mater.* **2004**, *3*, 458-463.

34. He, X.; Fu, Y.; Singh, D. J.; Zhang, L. *J. Mater. Chem. C.* **2016**, *4*, 11305-11312.

35. Madsen, G. K. H. *J. Am. Chem. Soc.* **2006**, *128*, 12140-12146.

36. Ortiz, B. R.; Gorai, P.; Krishna, L.; Mow, R.; Lopez, A.; McKinney, R.; Stevanovic, V.; Toberer, E. S. *J. Mater. Chem. A* **2017**, *5*, 4036-4046.

37. Huang, S.; Liu, H. J.; Fan, D. D.; Jiang, P. H.; Liang, J. H.; Cao, G. H.; Liang, R. Z.; Shi, J. *J. Phys. Chem. C* **2018**, *8*, 4217-4223.

38. Kieslich, G.; Birkel, C. S.; Stewart, A.; Kolb, U.; Tremel, W. *Inorg. Chem.* **2011**, *50*, 6938-6943.

39. Denoix, A.; Solaiappan, A.; Ayral, R. M.; Rouessac, F.; Tedenac, J. C. *J. Solid State Chem.* **2010**, *183*, 1090-1094.

40. Birkel, C. S.; Mugnaioli, E.; Gorelik, T.; Kolb, U. Panthofer, M.; Tremel, W. *J. Am. Chem. Soc.* **2010**, *132*, 9881-9889.

41. Mai, N. T.; Mott, D. M.; Higashimine, K.; Maenosono, S. *Chem. Lett.* **2012**, *41*, 1529-1531.

42. Owen, J. S.; Chan, E. M.; Liu, H.; Alvisatos, A. P. *J. Am. Chem. Soc.* **2010**, *132*, 18206-18213.

43. Chan, E. M.; Xu, C.; Mao, A. W.; Han, G.; Owen, J. S.; Cohen, B. E.; Milliron, D. J. *Nano Lett.* **2010**, *10*, 1874-1885.

44. Chan, E. M.; Han, G.; Goldberg, J. D.; Gargas, D. J.; Ostrowski, A. D.; Schuck, P. J.; Cohen, B. E.; Milliron, D. J. *Nano Lett.* **2012**, *12*, 3839-3845.

45. Zhu, T. J.; Yu, C.; He, J.; Zhang, S. N.; Zhao, X. B.; Tritt, T. M. *J. Electron. Mater.* **2009**, *38*, 1068-1071.

46. Zhang, X.; Peng, K.; Guo, L.; Yan, Y.; Zhan, H.; Lu, X.; Gu, H.; Zhou, X. *J. Electron. Mater.* **2017**, *46*, 2611-2615.

47. Shannon, R. D. *Acta Cryst.* **1976**, *32*, 751-767.

48. Kresse, G.; Furthmuller, J. *J. Comput. Mater. Sci.* **1996**, *6*, 15-50.

49. Kresse, G.; Furthmuller, J. *Phys. Rev. B*: *Condens. Matter Mater. Phys.* **1996**, *54*, 11169-11186.

50. Monkhorst, H. J.; Pack, J. D. *Phys. Rev. B* **1976**, *13*, 5188-5192.

51. Haas, P.; Tran, F.; Blaha, P. *Phys. Rev. B* **2009**, *79*, 085104.

52. Moulder, J. F.; Stickle, W. F.; Sobol, P. E.; Bomben, K. D. *Handbook of X-ray Photoelectron Spectroscopy: A Reference Book of Standard Spectra for Identification and Interpretation of XPS Data*; Chastain, J., King, R. C. Jr., Eds.; ULVAC-PHI: Japan, 1995.

53. White, M. A.; Thompson, M. J.; Miller, G. J.; Vela, J. *Chem. Commun.* **2016**, *52*, 3497-3499.

54. Mobarok, M. H.; Luber, E. J.; Bernard, G. M.; Peng, L.; Wasylishen, R. E.; Buriak, J. M. *Chem. Mater.* **2014**, *26*, 1925-1935.

55. Henkes, A. E.; Vasquez, Y.; Schaak, R. E. *J. Am. Chem. Soc.* **2007**, *129*, 1896-1897.

56. Henkes, A. E.; Schaak, R. E. *Chem. Mater.* **2007**, *19*, 4234-4242.

57. Carenco, S.; Portehault, D.; Boissiere, C.; Mezailles, N.; Sanchez, C. *Chem. Rev.* **2013**, *113*, 7981-8065.

58. Chiang, R.-K.; Chiang, R.-T. *Inorg. Chem.* **2007**, *46*, 369-371.

59. Muthuswamy, E.; Kharel, P. R.; Lawes, G.; Brock, S. L. *ACS Nano* **2009**, *3*, 2383-2393.

60. Brock, S. L.; Senevirathne, K. *J. Solid State Chem.* **2008**, *181*, 1552-1559.

61. Toberer, E. S.; Rauwel, P.; Gariel, S.; Tafto, J.; Snyder, G. J. *J. Mater. Chem.* **2010**, *20*, 9877-9885.

62. Xiong, D.-B.; Okamoto, N. L.; Inui, H. *Scripta Mater.* **2013**, *69*, 397-400.

63. Heremans, J. P.; Dresselhaus, M. S.; Bell, L. E.; Morelli, D. T. *Nat. Nanotech.* **2013**, *8*, 471-473.

64. Dresselhaus, M. S.; Chen, G.; Tang, M. Y.; Yang, R. G.; Lee, H.; Wang, D. Z.; Ren, Z. F.; Fleurial, J.-P.; Gogna, P. *Adv. Mater.* **2007**, *19*, 1043-1053.

65. Ibanez, M.; Luo, Z.; Genc, A.; Piveteau, L.; Ortega, S.; Cadavid, D.; Dobrozhan, O.; Liu, Y.; Nachtegaal, M.; Zebarjadi, M.; Arbiol, J.; Kovalenko, M. V.; Cabot, A. *Nat. Commun.* **2016**, *7*, 10766.

66. Blichfeld, A. B.; Iversen, B. B. *J. Mater. Chem. C.* **2015**, *3*, 10543-10553.

67. Clark, S. J.; Segall, M. D.; Pickard, C. J.; Hasnip, P. J.; Probert, M. J.; Refson, K.; Payne, M. C. *Z. Kristallogr. - Cryst. Mater.* **2005**, *220 (5−6),* 567−570.

68. Rosales, B. A.; White, M. A.; Vela, J. *J. Am. Chem. Soc.* **2018**, *140*, 3736-3742.

69. Chupas, P. J.; Chapman, K.W.; Kurtz, C.; Hanson, J.C.; Lee, P.L.; Grey, C.P. *J. Appl. Cryst.* **2008**, *41*, 822-824.

70. Harris, R. K.; Becker, E. D.; De Menezes, S. M. C.; Goodfellow, R.; Granger, P. *Pure Appl Chem* **2001**, *73*, 1795–1818.

71. Oas, T. G.; Griffin, R. G.; Levitt, M. H. *J. Chem. Phys.* **1988**, 89 (2), 692−695.

72. Schnell, I. *Prog. Nucl. Magn. Reson. Spectrosc.* **2004**, *45*, 145-207.

73. Venkatesh, A.; Hanrahan, M. P.; Rossini, A. J. *Solid State Nucl. Magn. Reson.* **2017**, *84*, 171-181.

74. Hung, I.; Schurko, R.W. *J. Phys. Chem. B* **2004**, *108*, 9060-9069.

75. Perras, F. A.; Widdifield, C. M.; Bryce, D. L. *Solid State Nucl. Magn. Reson.* **2012**, *45-46*, 36-44.

76. Clark, S. J.; Segall, M. D.; Pickard, C. J.; Hasnip, P. J.; Probert, M. J.; Refson, K.; Payne, M. C. Z. Kristallogr. - Cryst. Mater. 2005, 220 (5−6), 567−570.

77. Faucher, A.; Terskikh, V. V.; Wasylishen, R. E. *Solid State Nucl. Magn. Reson.* **2014**, *61–62*, 54–61.

78. Perdew, J. P.; Burke, K.; Ernzerhof, M. Phys. Rev. Lett. 1996, 77 (18), 3865−3868.

79. Tkatchenko, A.; Scheffler, M. Phys. Rev. Lett. 2009, 102 (7), 073005.

80. Yates, J. R.; Pickard, C. J.; Mauri, F. Phys. Rev. B: Condens. Matter Mater. Phys. 2007, 76 (2), 024401.

81. Pickard, C. J.; Mauri, F. Phys. Rev. B: Condens. Matter Mater. Phys. 2001, 63 (24), 245101.

82. Kresse, G. *Phys. Rev. B* **1999**, *59*, 1758–1775.

83. Blöchl, P. E. *Phys. Rev. B* **1994**, *50*, 17953–17979.

Appendix of Supporting Information

Scheme S1. Solution phase general screening of reaction parameters (x, y, z, injection temp, growth temp, and reaction time) on WANDA.

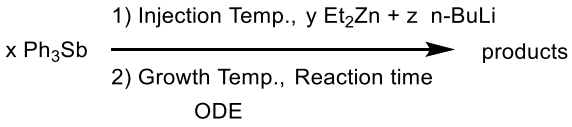

Scheme S2. Solution phase synthesis of hexagonal LiZnSb.

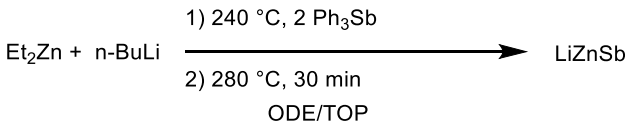

Scheme S3. Solution phase synthesis of binary ZnSb.

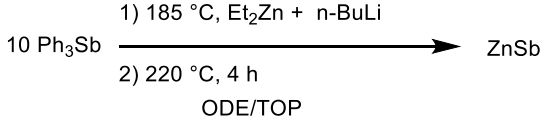

Scheme S4. Solution phase synthesis of binary β-Zn_8Sb_7.

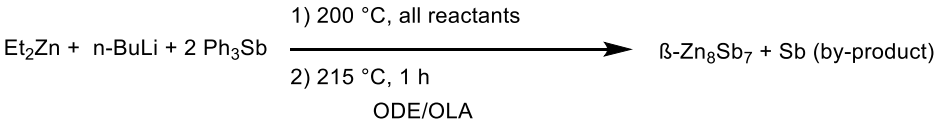

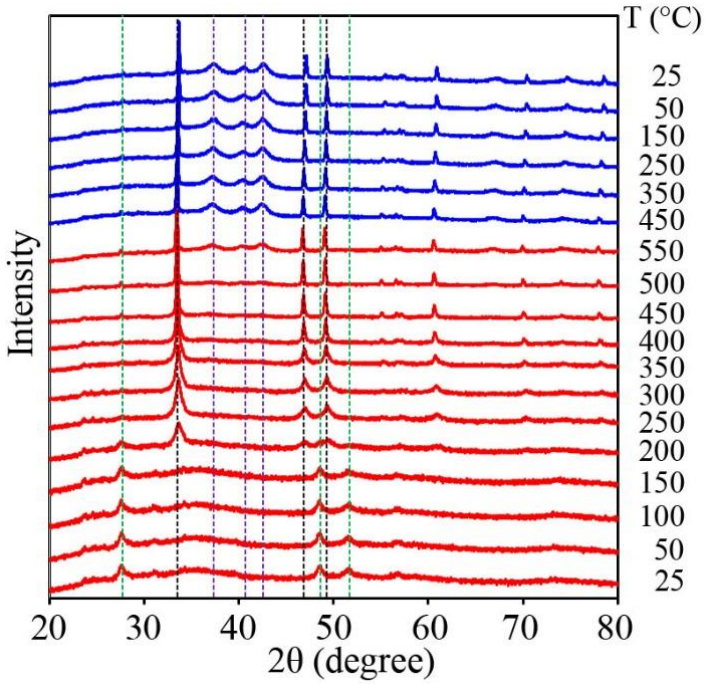

Figure S1. Hot-stage powder X-ray diffraction of h*-LiZnSb prepared from reacting precursors at 250 °C for 2 h. Data was collected every 50 °C while heating (red) with no temperature increase occurring during data collection. Data was collected every 100 °C while cooling (blue) with no temperature change occurring during data collection. Guidelines are given to show the location of the three most intense reflections for hexagonal $CaZn_2Sb_2$-type (green), Sb (black), and ZnO (purple).

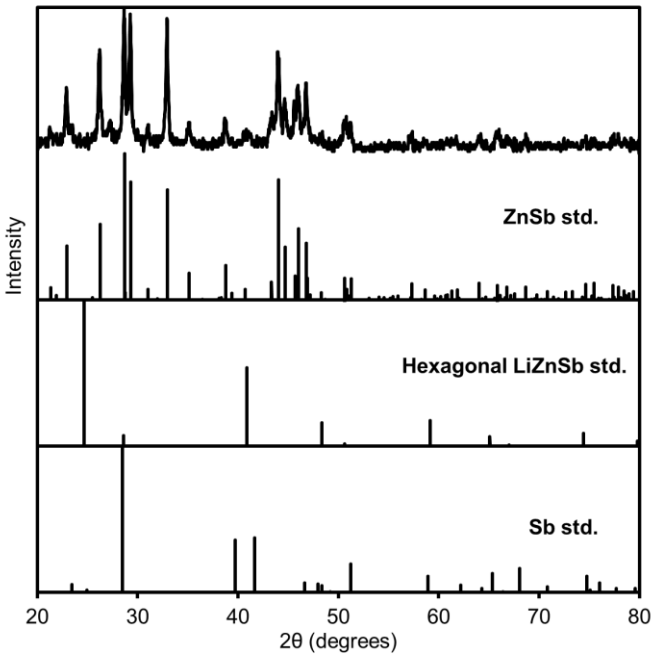

Figure S6. PXRD binary ZnSb obtained for long reaction times (4h) after decomposition of hexagonal LiZnSb. Standard patterns of potential phases are shown for comparison.

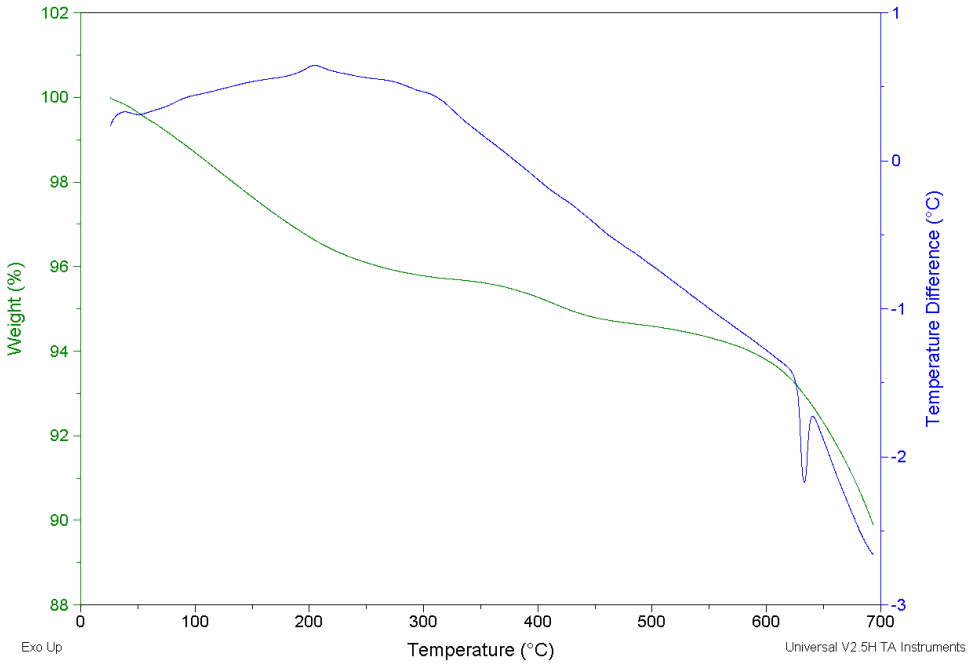

Figure S2. TGA-DTA of h*-LiZnSb sample heated from ambient to 690 °C at a rate of 5°C/min. Nitrogen gas was consistently flushed through the system at a rate of 100 mL/min.

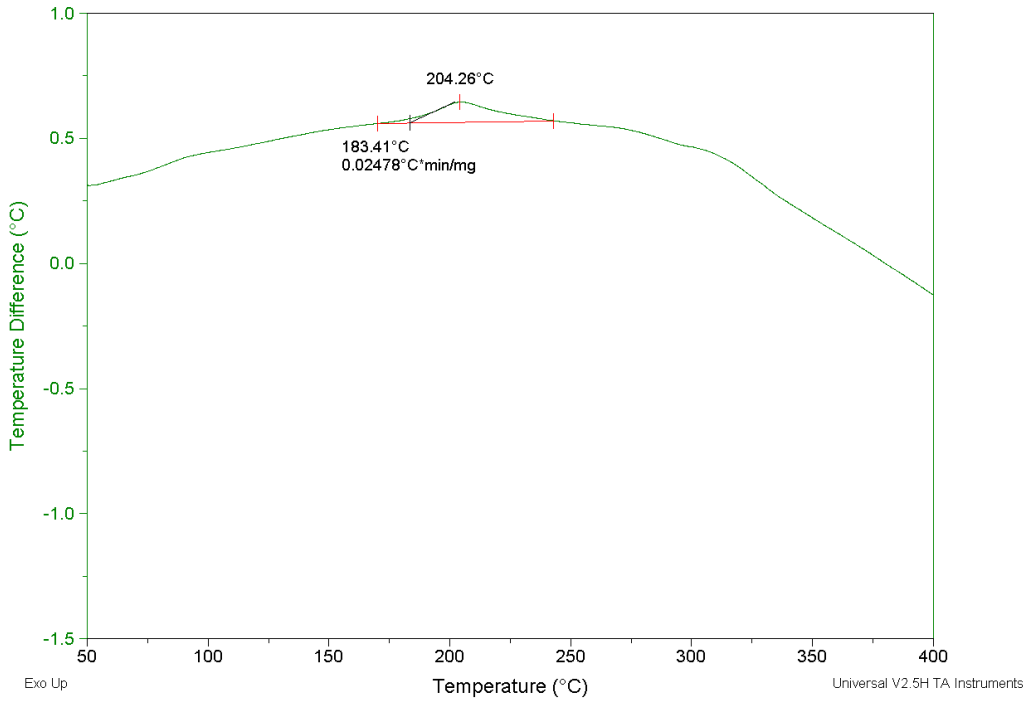

Figure S3. TGA-DTA of h*-LiZnSb sample heated from ambient to 690 °C at a rate of 5°C/min zoomed into the first significant exothermic transition at 204 °C showing the crystallization of amorphous antimony. Nitrogen gas was consistently flushed through the system at a rate of 100 mL/min.

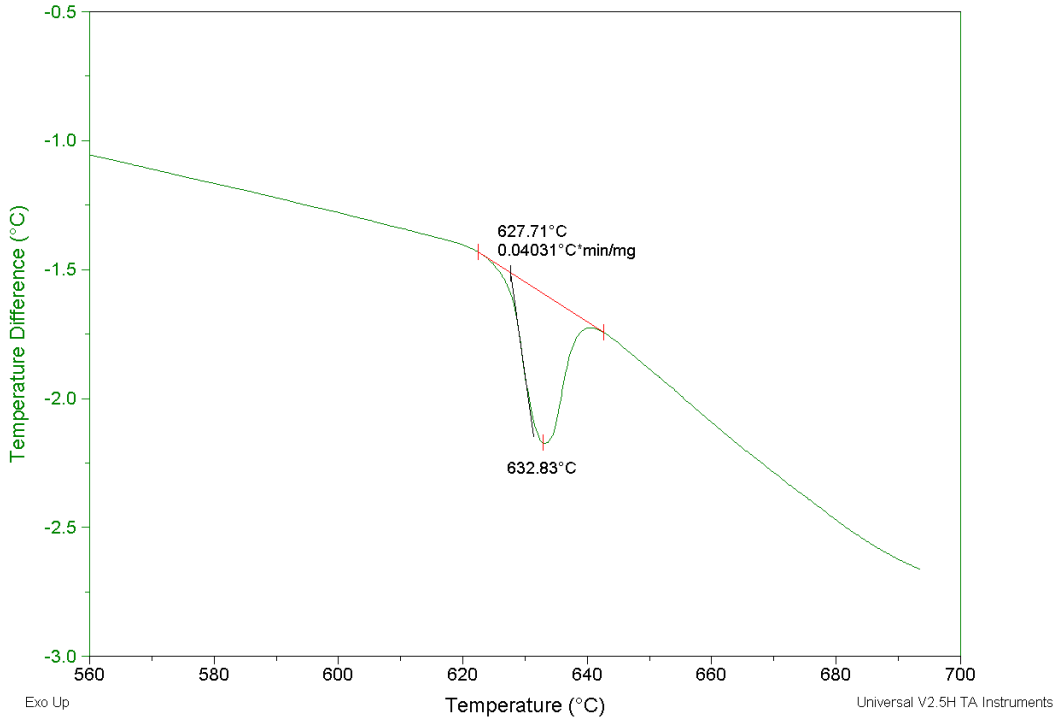

Figure S4. TGA-DTA of h*-LiZnSb sample heated from ambient to 690 °C at a rate of 5°C/min zoomed into the significant endothermic transition at 633 °C highlighting the melting of of crystalline antimony. Nitrogen gas was consistently flushed through the system at a rate of 100 mL/min.

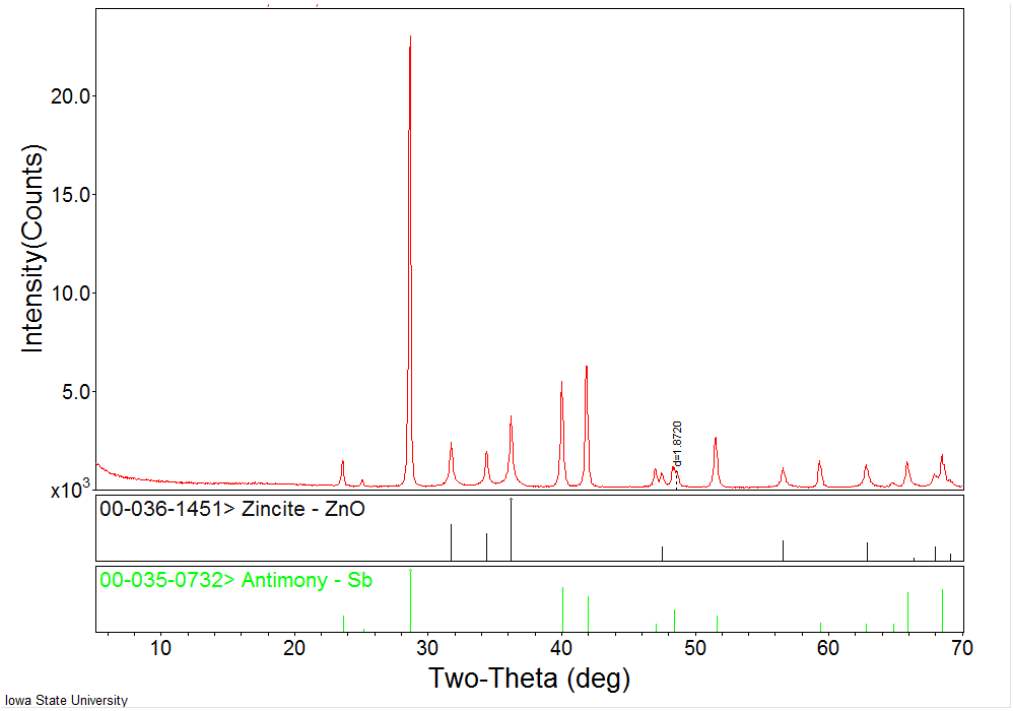

Figure S5. PXRD of h*-LiZnSb collected after heating to 690 °C for TGA-DTA and then subsequent cooling back to ambient temperature (top panel). The primary crystalline products are antimony metal (bottom panel) and zinc oxide (middle panel).

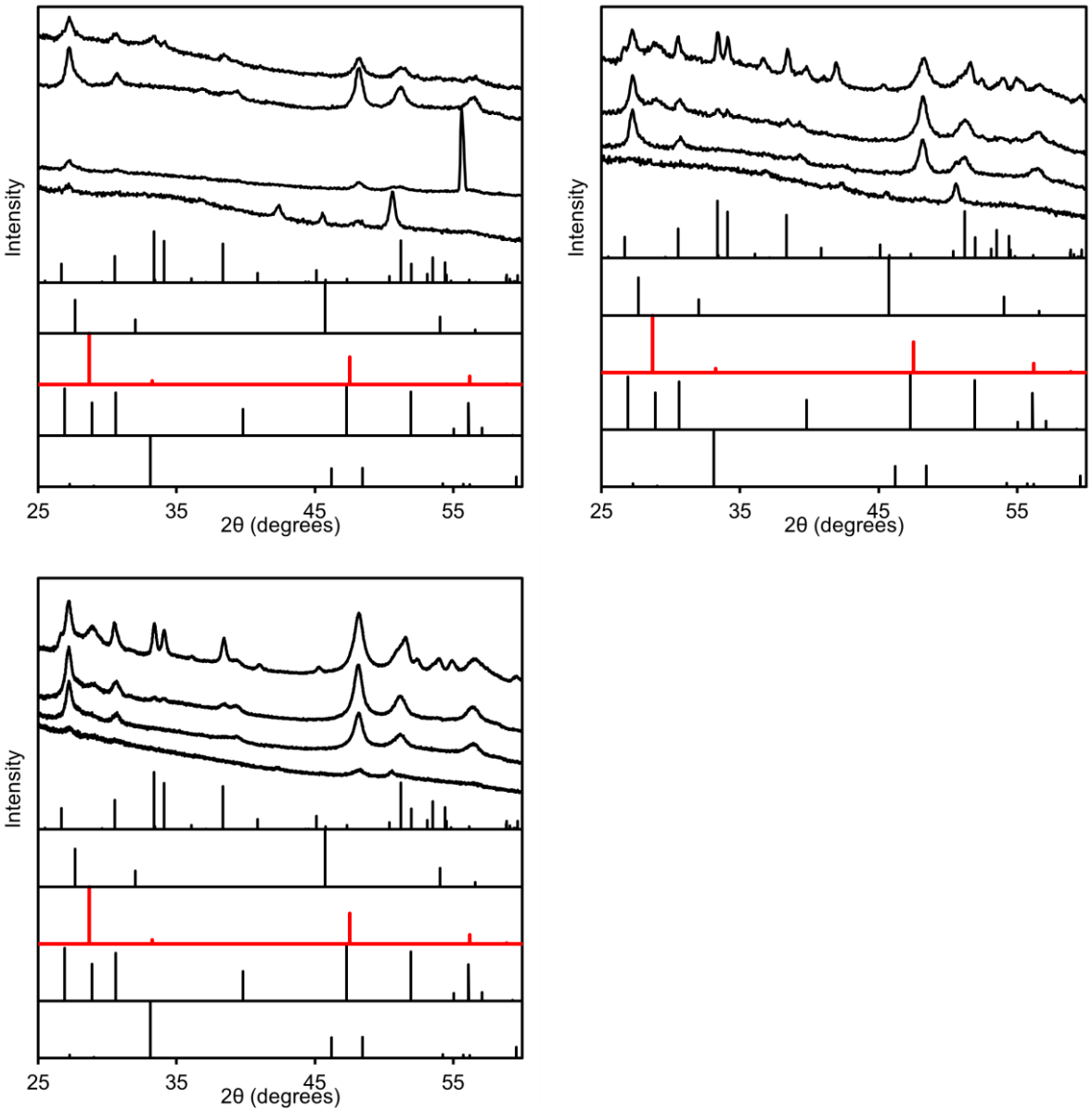

Figure S7. WANDA screening of Sb concentration effect with an injection temperature of 150 °C and grown temperature of 260 °C with aliquots taken at (from bottom to top) 30 min, 1 h, 2 h, and 4 h. Standard patterns from bottom to top are Sb, hexagonal LiZnSb, cubic LiZnSb, Li_2ZnSb , and ZnSb. The tested Sb concentrations are 2-fold excess (top left), 4-fold excess (top right), and 8-fold excess (bottom).

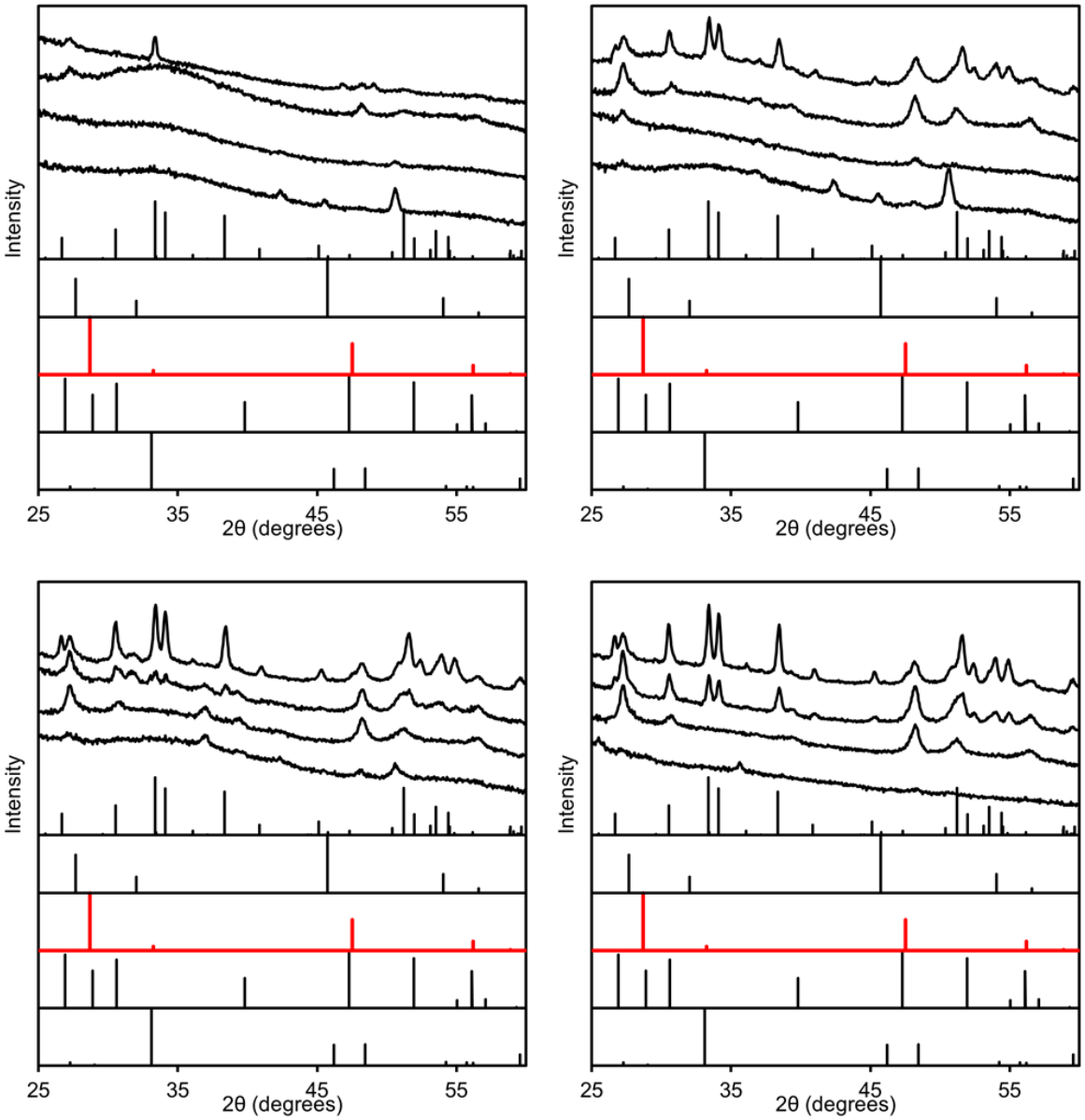

Figure S8. WANDA screening of Sb concentration effect with an injection temperature of 200 °C and grown temperature of 260 °C with aliquots taken at (from bottom to top) 30 min, 1 h, 2 h, and 4 h. Standard patterns from bottom to top are Sb, hexagonal LiZnSb, cubic LiZnSb, Li_2ZnSb , and ZnSb. The tested Sb concentrations are stoichiometric (top left), 2-fold excess (top right), 4-fold excess (bottom left), and 8-fold excess (bottom right).

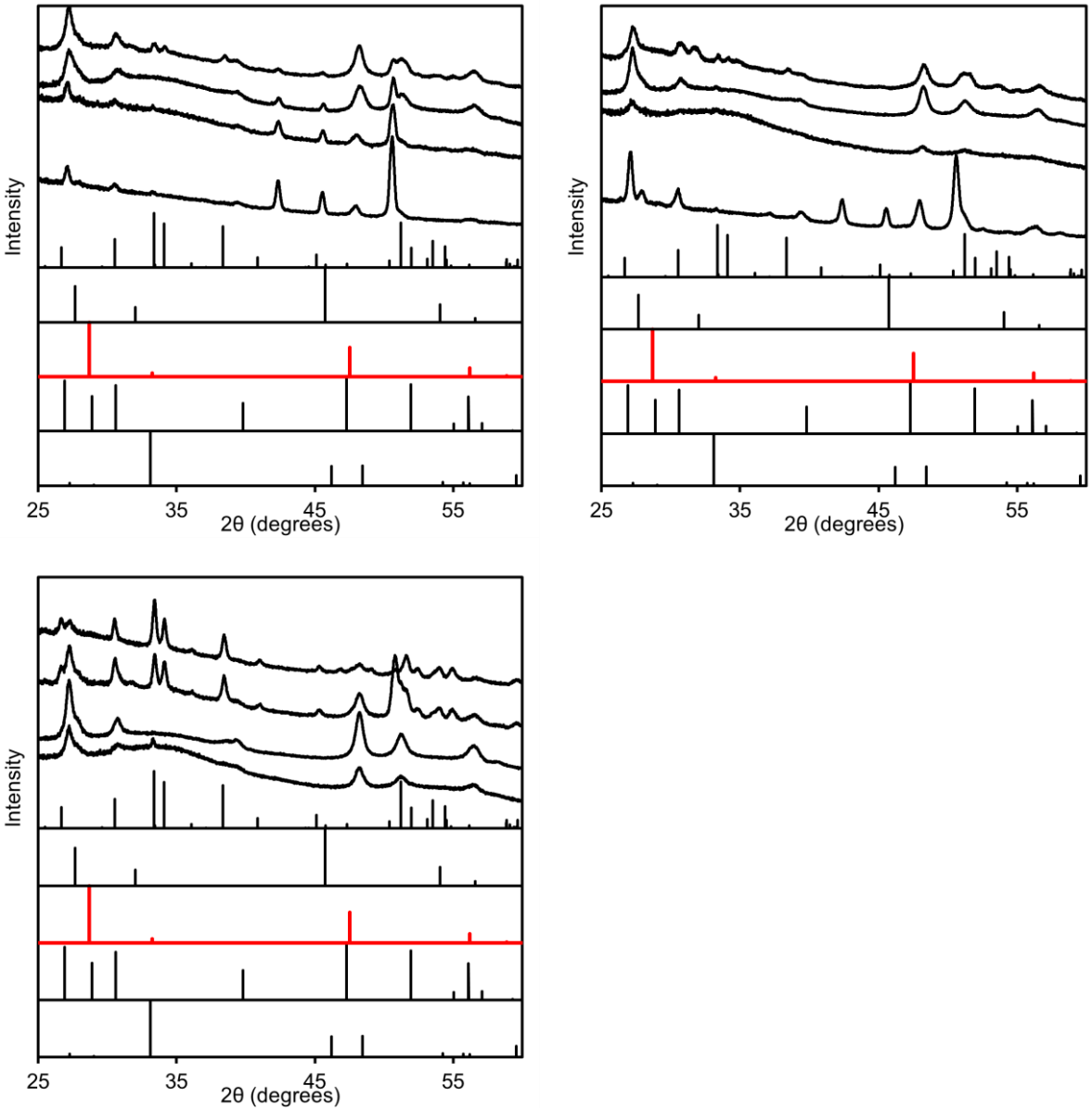

Figure S9. WANDA screening of Sb concentration effect with an injection temperature of 200 °C and grown temperature of 260 °C in the presence of TOP with aliquots taken at (from bottom to top) 30 min, 1 h, 2 h, and 4 h. Standard patterns from bottom to top are Sb, hexagonal LiZnSb, cubic LiZnSb, Li_2ZnSb , and ZnSb. The tested Sb concentrations are stoichiometric (top left), 2-fold excess (top right), and 4-fold excess (bottom).

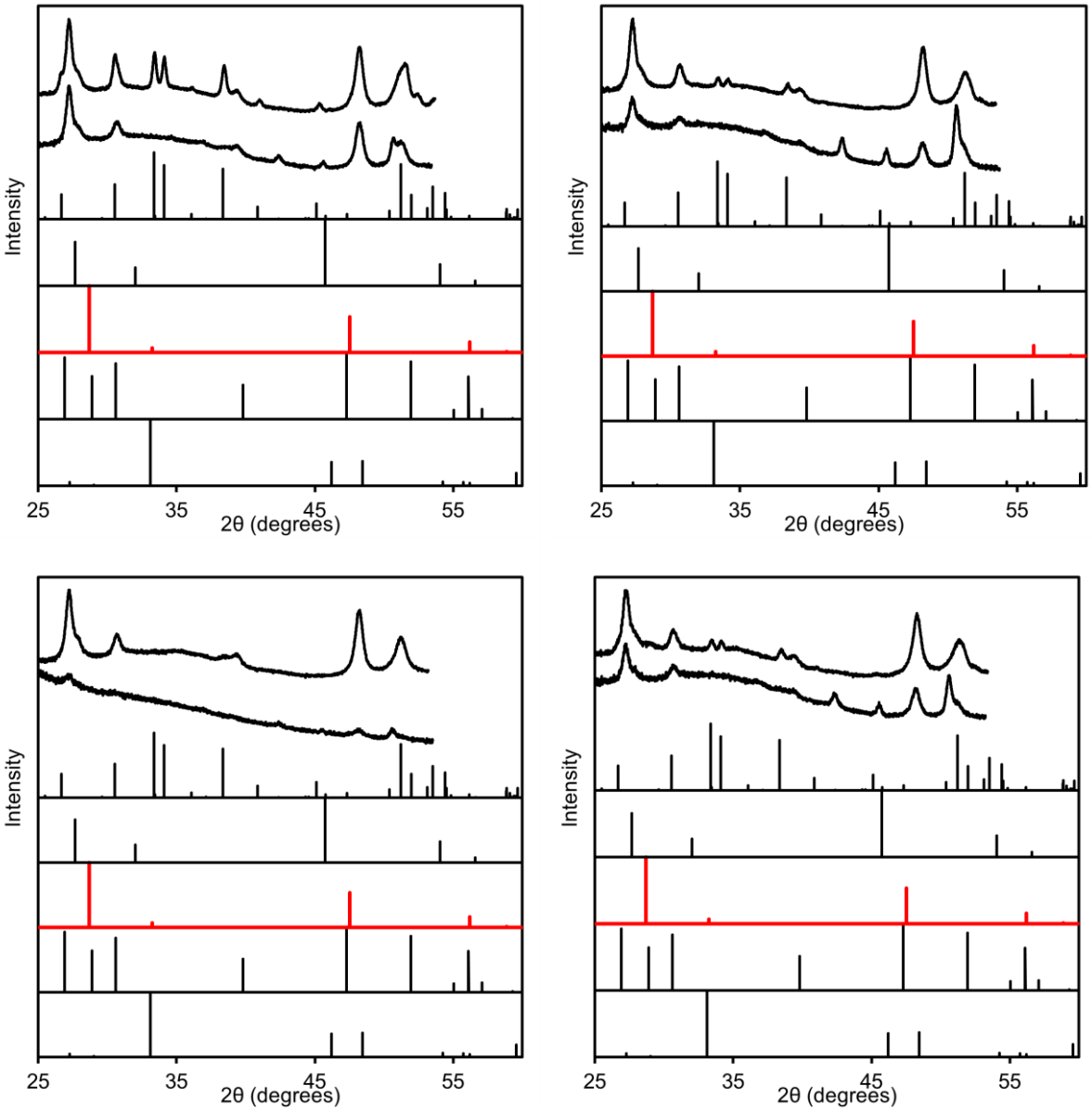

Figure S10. WANDA screening of the effect of delayed injection between the *n*-BuLi and Et_2Zn for a 2-fold excess of Sb *vs*. Li/Zn with aliquots taken at (from bottom to top) 1 h and 4 h. Standard patterns from bottom to top are Sb, hexagonal LiZnSb, cubic LiZnSb, Li_2ZnSb , and ZnSb. The tested delay times are 2 min (top left), 5 min (top right), 10 min (bottom left), and 15 min (bottom right).

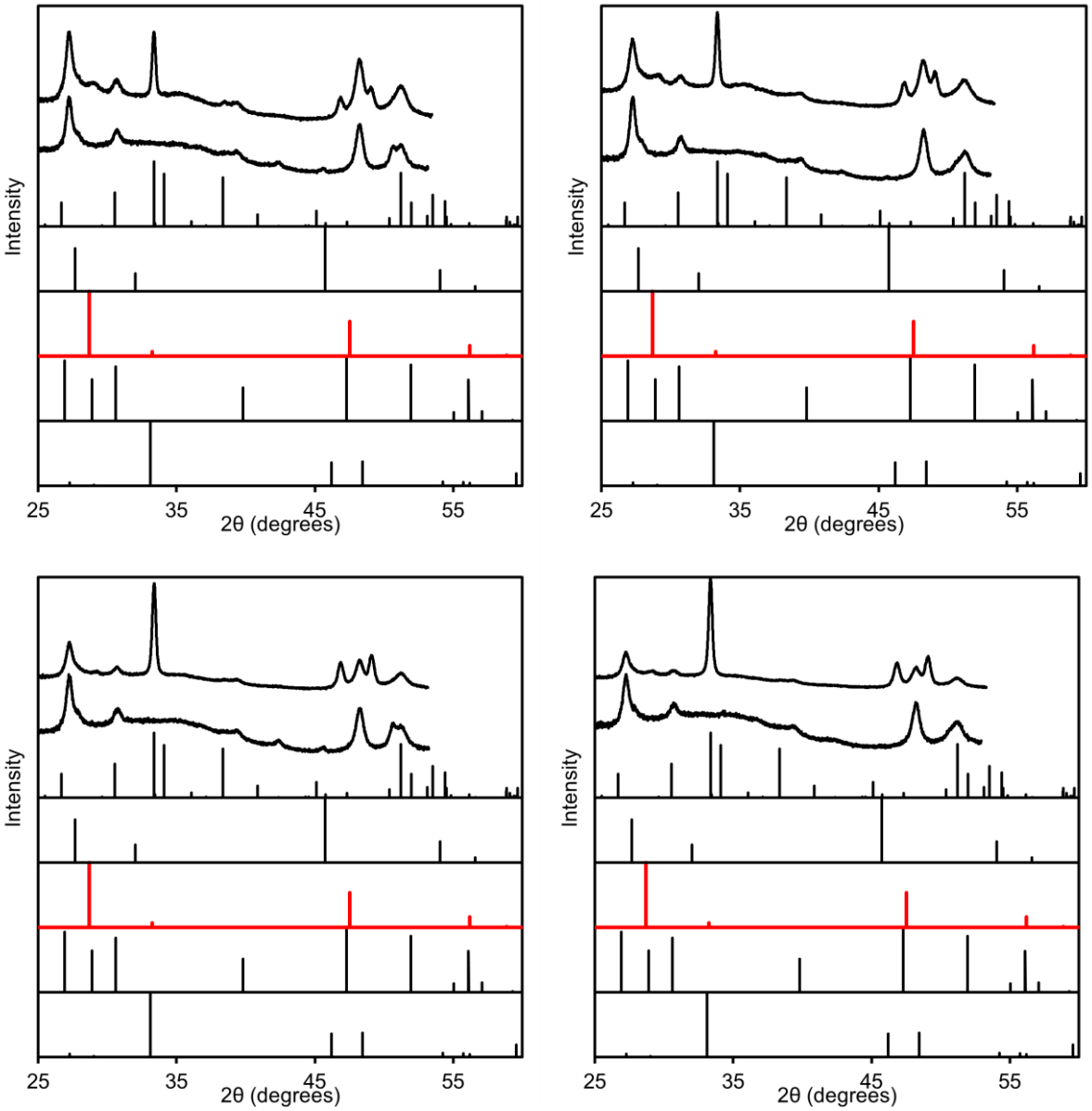

Figure S11. WANDA screening of the effect of delayed injection between the *n*-BuLi and Et_2Zn for a 8-fold excess of Sb *vs*. Li/Zn with aliquots taken at (from bottom to top) 1 h and 4 h. Standard patterns from bottom to top are Sb, hexagonal LiZnSb, cubic LiZnSb, Li_2ZnSb , and ZnSb. The tested delay times are 2 min (top left), 5 min (top right), 10 min (bottom left), and 15 min (bottom right).

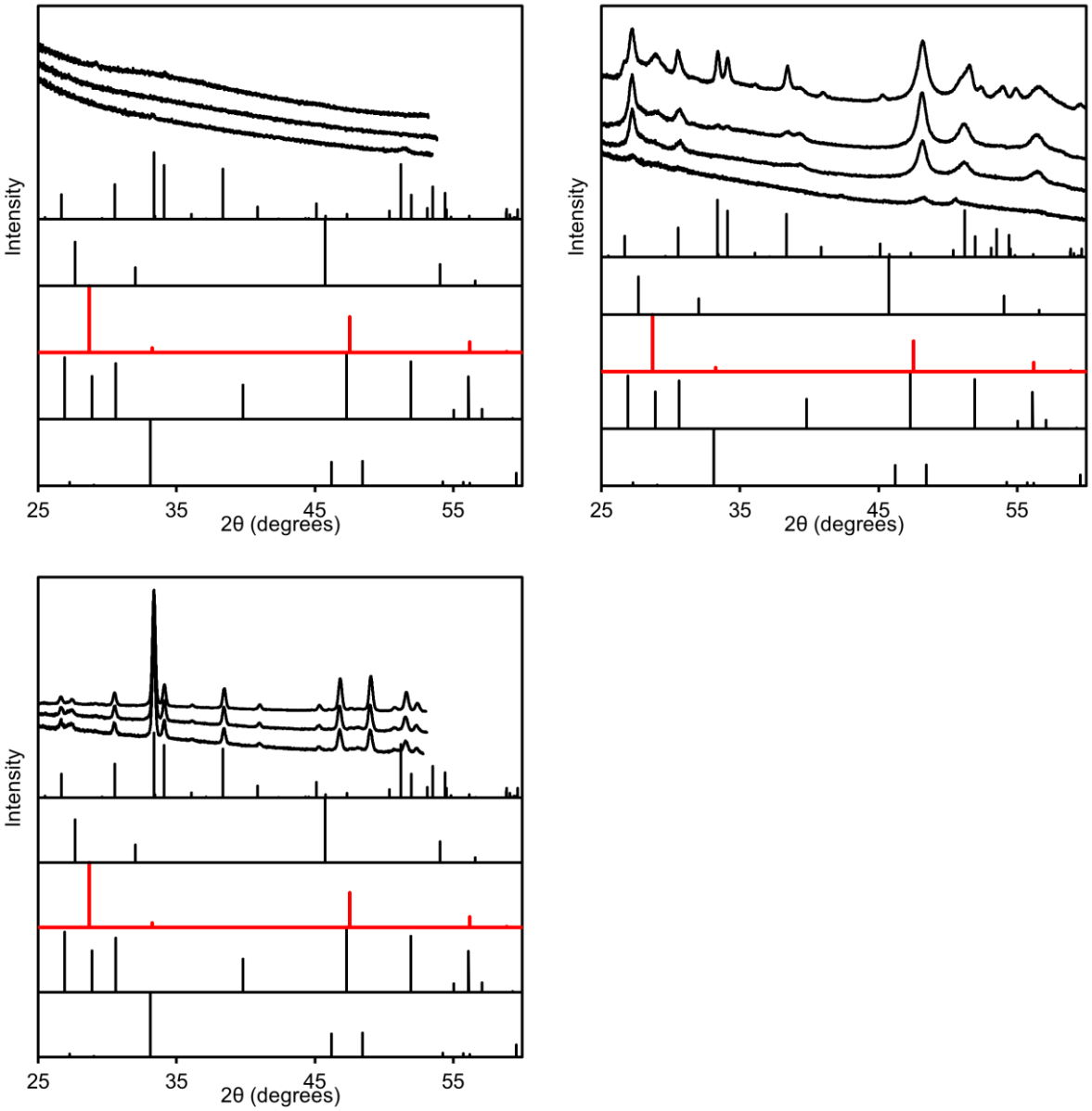

Figure S12. WANDA screening of the effect of growth temperature for a 8-fold excess of Sb *vs.* Li/Zn with aliquots taken at (from bottom to top) 1 h, 2h, and 4 h. Standard patterns from bottom to top are Sb, hexagonal LiZnSb, cubic LiZnSb, Li_2ZnSb , and ZnSb. The tested growth temperatures are 200 °C (top left), 260 °C (top right), and 300 °C (bottom).

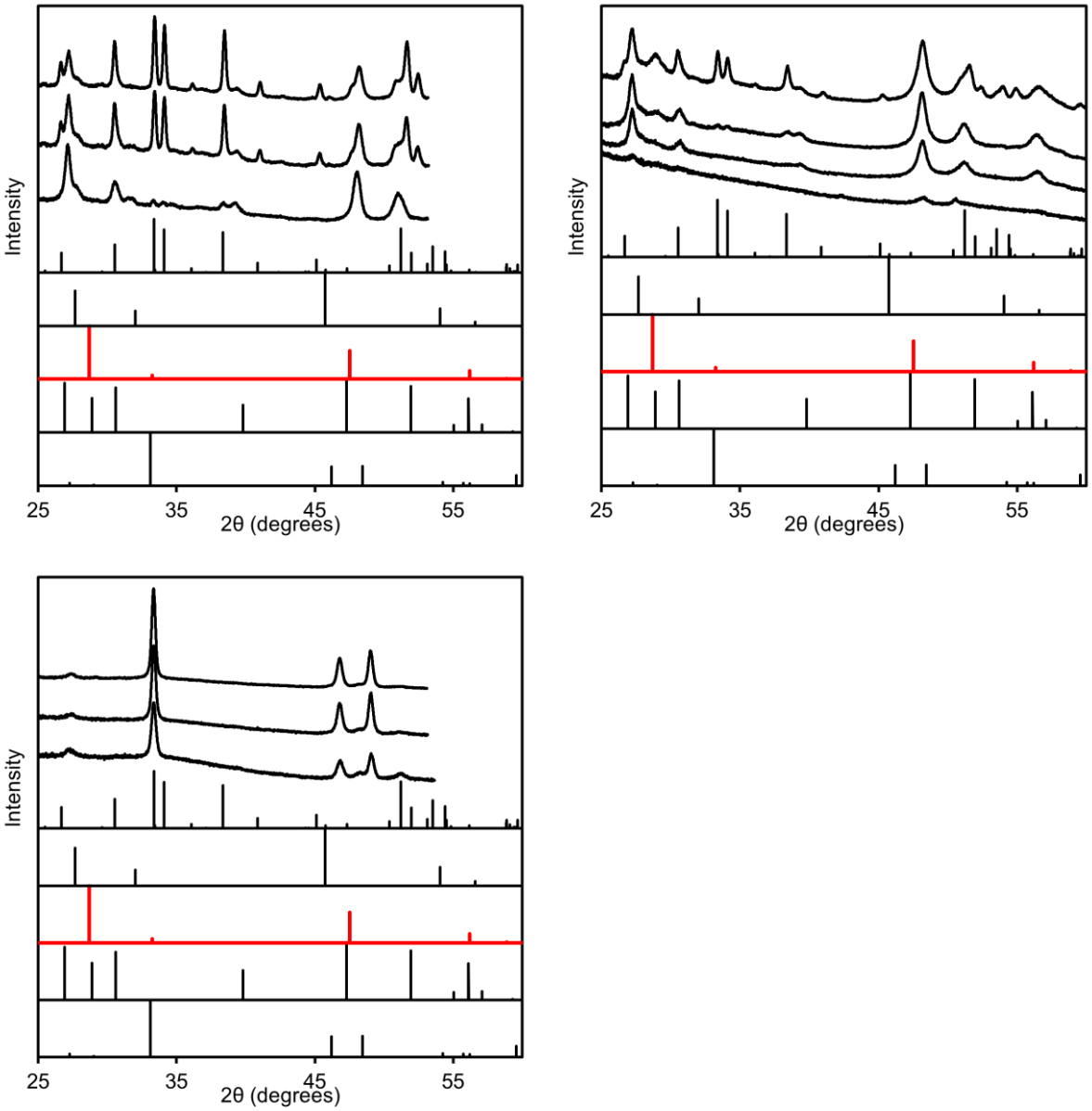

Figure S13. WANDA screening of the effect of varying concentration of Li and Zn relative to Sb aliquots taken at (from bottom to top) 1 h, 2h, and 4 h. Standard patterns from bottom to top are Sb, hexagonal LiZnSb, cubic LiZnSb, Li_2ZnSb , and ZnSb. The tested concentrations of Li:Zn:Sb are 1:2:8 (top left), 1:1:8 (top right), and 2:1:8 (bottom).

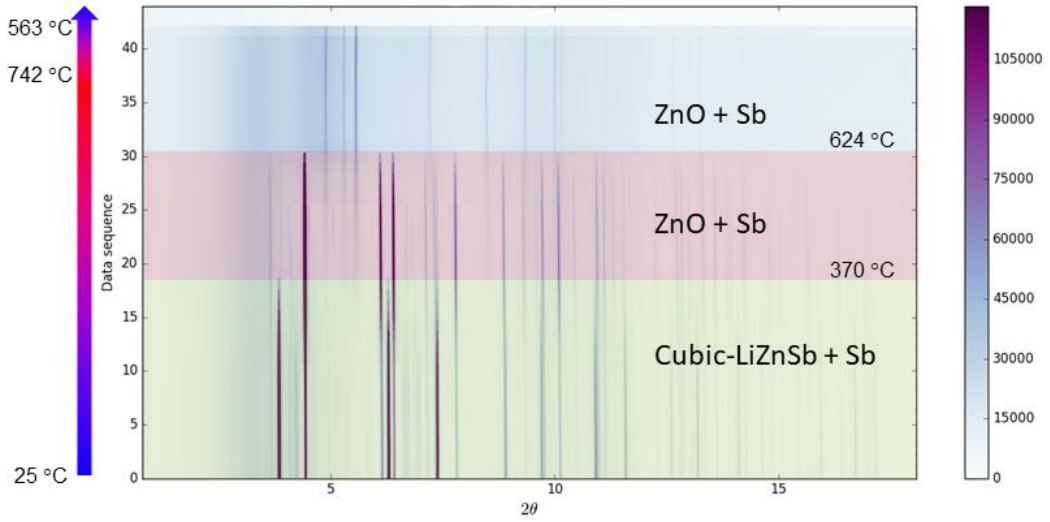

Figure S14. XRD with variable temperature of c-LiZnSb collected on 17-BM at APS from room temperature up to 742 °C. Main reflections until 370°C correspond to c-LiZnSb and elemental Sb. Between 370 °C and 624 °C both Sb and ZnO are observed. Following the melting of Sb, only ZnO reflections are seen.

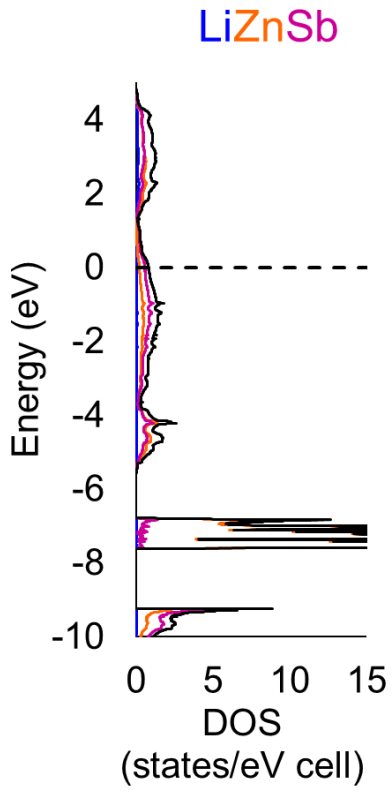

Figure S15. Density of state for h*-LiZnSb calculated using LDA. Partial density of states for Li (blue), zinc (orange), and Sb (purple) are provided. h*-LiZnSb is a metal with a peak in the DOS at the Fermi level. It is located nearby a pseudogap around 1.3 eV, indicating that a slight excess in electrons should stabilize this structure.

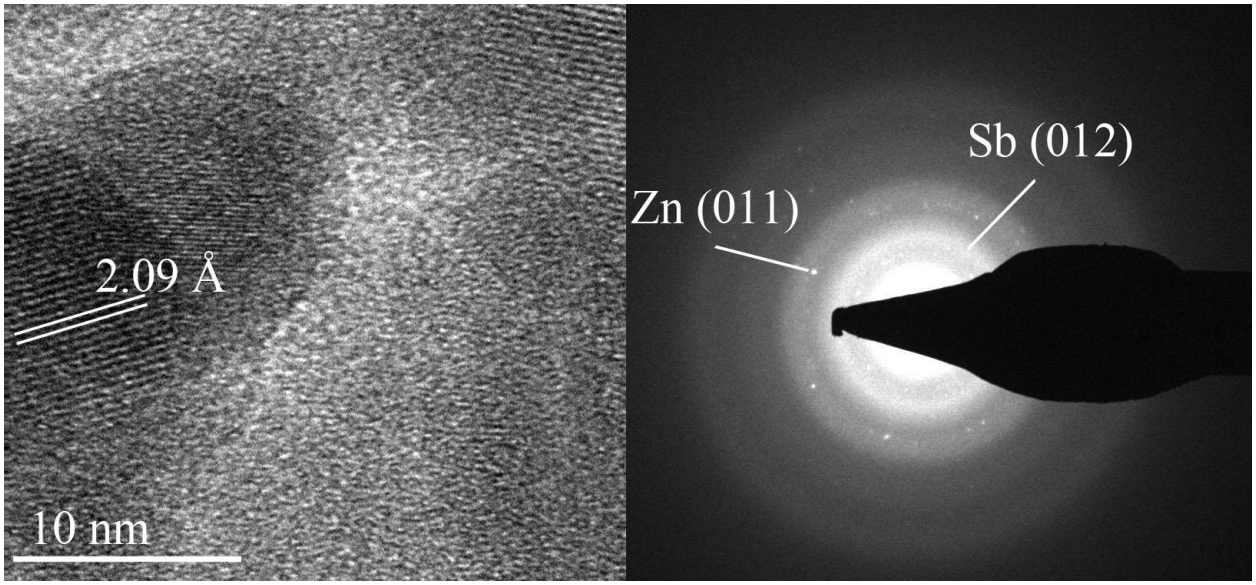

Figure S16. Representative TEM and SAED of h*-LiZnSb after 12 min at 280 °C. The TEM shows lattice fringes consistent with the most intense reflection of Zn metal (011) indicating its presence as an intermediate. SAED shows distinct crystalline reflections consistent with Zn metal and amorphous lines consistent with the most intense reflection of Sb (012).

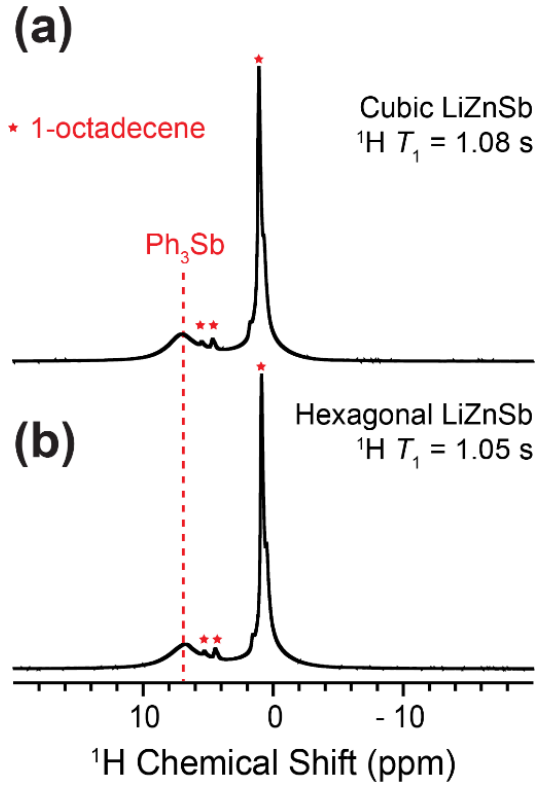

Figure S17. ^{1}H spin echo spectra of c-LiZnSb (a) and h*-LiZnSb (b).

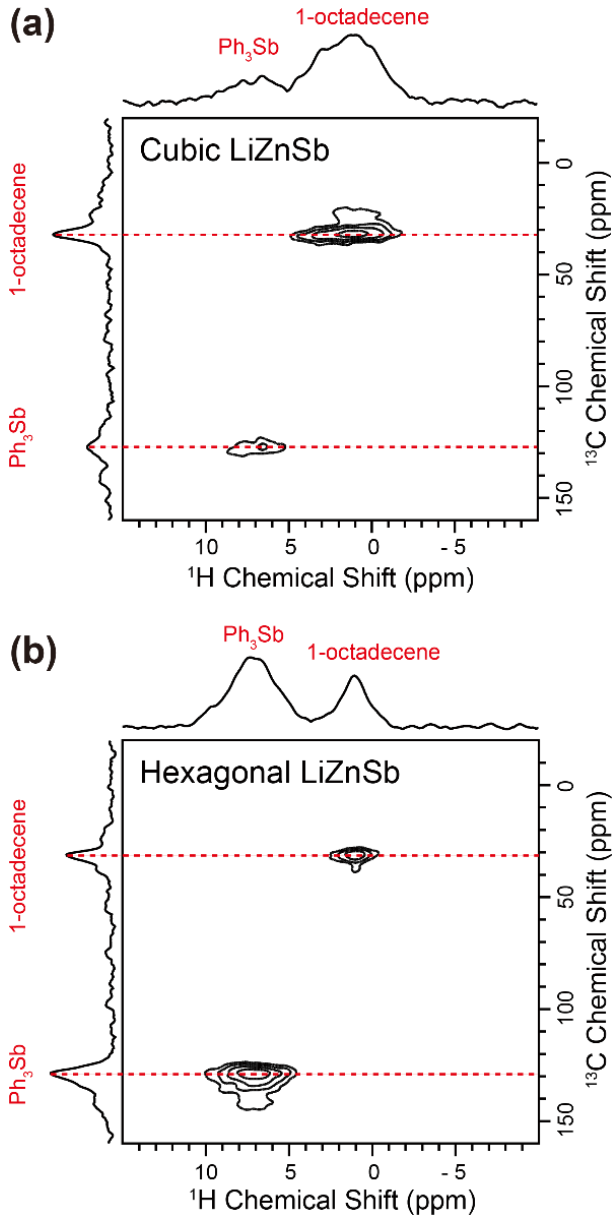

Figure S18. ^{1}H detected 2D ^{13}C→^{1}H CP-HETCOR spectra of c-LiZnSb (a) and h*-LiZnSb (b). The cross peaks shown in the spectra indicate protons bonded to carbon atoms in a given system.

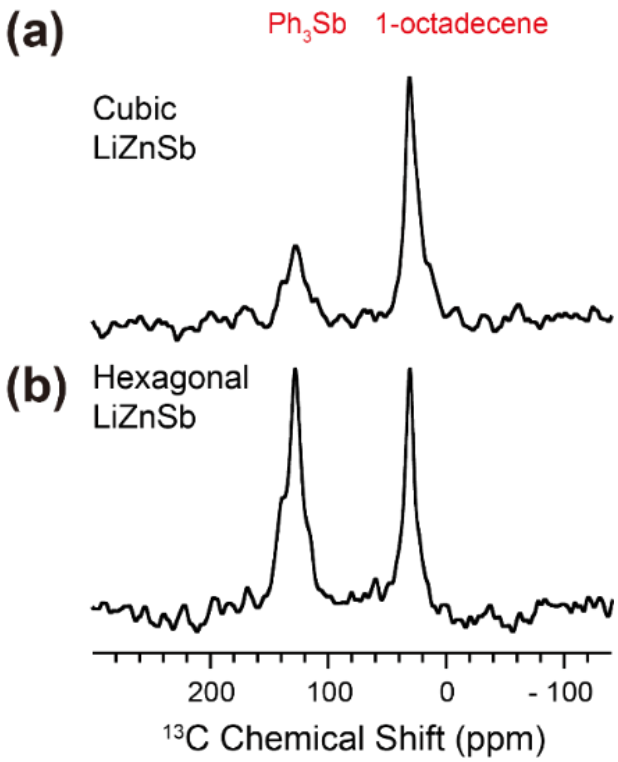

Figure S19. Comparison of direct detected $^{1}H \rightarrow ^{13}C$ CP ssNMR spectra of c-LiZnSb (a) and h*-LiZnSb (b).

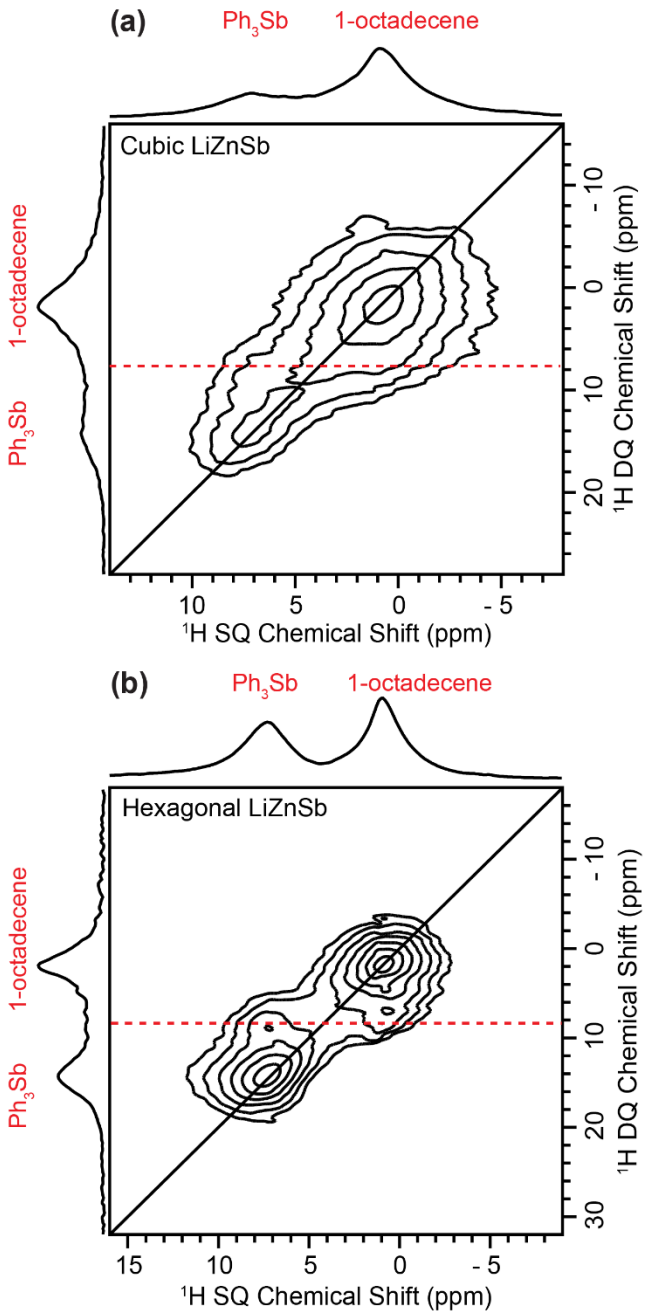

Figure S20. 2D dipolar double quantum–single quantum (DQ-SQ) correlation spectra of the c-LiZnSb (a) and h*-LiZnSb (b), respectively obtained using BABA dipolar recoupling. The DQ chemical shift corresponding to a certain DQ coherence is the sum of two SQ chemical shifts. The presence of a peak in the DQ dimension indicate two ^{1}H nuclei in close spatial proximity.

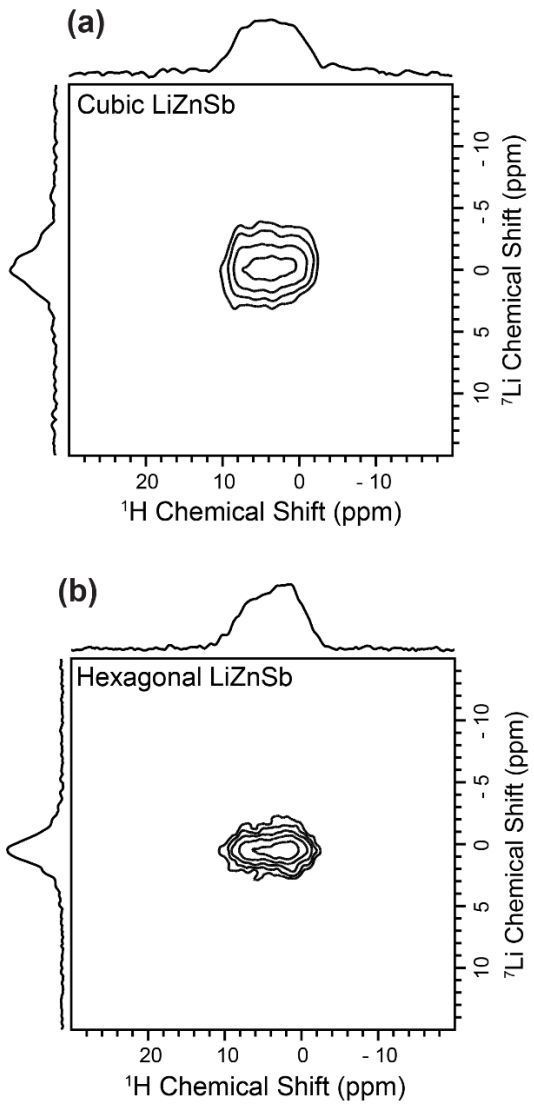

Figure S21. ^{1}H detected surface-selective 2D ^{7}Li→^{1}H D-RINEPT of c-LiZnSb (a) and h*-LiZnSb (b). The appearance of through space cross-correlation peaks between Li and H indicates the surface environment of LiZnSb.

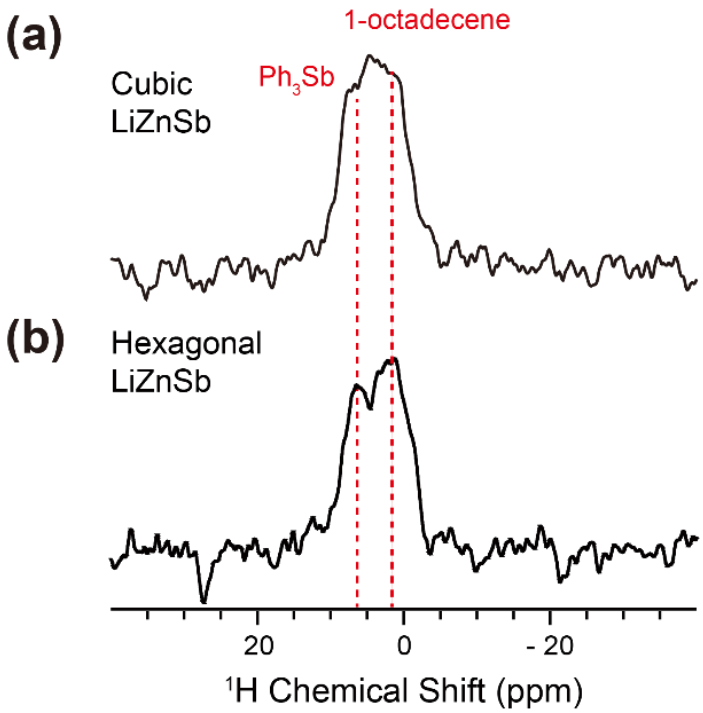

Figure S22. ^{1}H detected 1D $^{7}Li \rightarrow ^{1}H$ D-RINEPT spectra with short recoupling time. The observed proton peaks are originated from protons which are in close spatial proximity of surface lithium sites.

Table S1. Recycle delays, number of scans and indirect dimension points of solid state NMR spectra of c-LiZnSb NPs and h*-LiZnSb NPs.

	^{1}H Spin Echo	^{7}Li Spin Echo	^{1}H BABA DQ-SQ	$^{13}C \rightarrow ^{1}H$ CP-HETCOR	$^{1}H \rightarrow ^{13}C$ CP	2D $^{7}Li \rightarrow ^{1}H$ D-RINEPT
c-LiZnSb NPs						
Recycle Delay (s)	1.4	16.9	1.4	1.4	1.4	26
Scans[a]	8	2	8×138	64×204	16384	8×160
h*-LiZnSb NPs						
Recycle Delay (s)	1.4	6.5	1.4	1.4	1.8	7.0
Scans[a]	8	2	8×144	32×256	6144	4×160

[a]For 2D experiments, the first number represents the number of scans and the second number represents the number of indirect dimension points.

Table S2. Calculated EFG parameters using CASTEP.

Compound	Calculated			Reference[a]
	Vzz/a.u.	C_Q/MHz	η	
SbH_3	1.3939	178	0.07	[1]
SbF_3	-3.4984	-466	0.11	[2]
$SbCl_3$	-2.3833	-304	0.11	[3]
SbI_3	4.8809	622	0	[4]
$SbCl_5$	-0.4752	-60.6	0	[5]
c-LiZnSb	0	0	N/A	This work
h*-LiZnSb	0.546	69.6	0	This work

[a]The reference listed here showed the origin of the crystal structure.

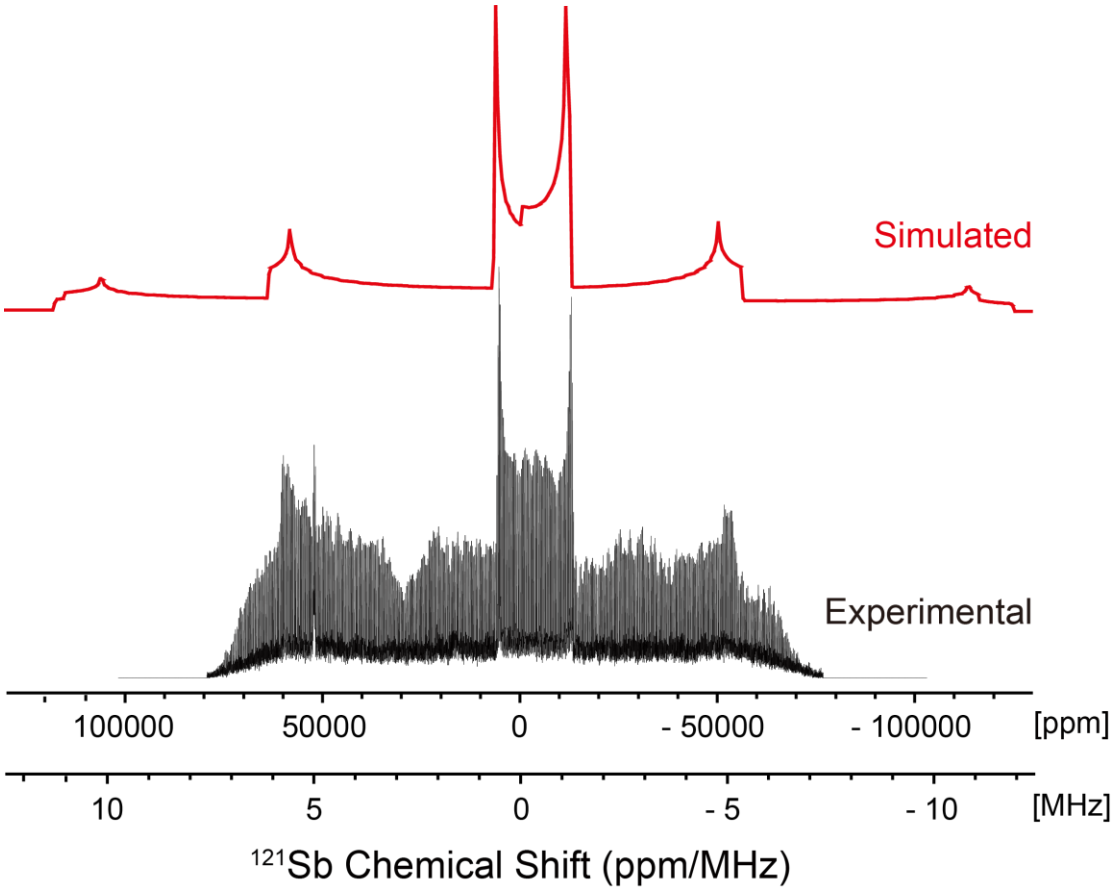

Figure S23. Experimental (lower trace) and simulated (upper trace) ^{121}Sb solid-state NMR spectra of c-LiZnSb acquired at 9.4 T. Recycle delay = 0.1 s. Number of scans for each QCPMG spectrum = 32768.

Table S3. EFG parameters using to simulate experimental spectrum.

	δ_{iso}/ppm	C_Q/MHz	η
c-LiZnSb	-500	74	0.05

Supplemental References

1. Abe, K; Ashcroft, N. W. *Phys. Rev. B* **2015**, *92*, 224109.
2. Edwards, A. J. *J. Chem. Soc.* **1970**, 2751–2753
3. Lindqvist, I; Niggli, A. *J. Inorg. Nucl. Chem.* **1956**, *2*, 345–347.
4. Trotter, J; Zobel, T. *Z. Kristallogr.* **1966**, *123*, 67–72.
5. Ohlberg, S. M. *J. Am. Chem. Soc.* **1959**, *81*, 811–813.

CHAPTER 5

CONCLUSIONS AND OUTLOOK

This thesis describes the synthesis, characterization, and computational investigation of filled tetrahedral semiconductors prepared through solution phase methods. Chapter 2 displays the first solution phase synthesis of a filled tetrahedral semiconductor through the successful synthesis of LiZnP. This result served as a springboard for the remainder of the work presented throughout this thesis. First, it presented a generalized reaction for the formation of I-II-V semiconductors using a wide range of precursors. Notably, it established triphenylpnictides, which are commercially available for all pnictides, to be effective precursors. This allowed for later (Chapter 3) synthesis of LiZnSb from triphenylstibine. Second, it established a mechanism for the formation of LiZnP through a zinc metal intermediate. This zinc metal, which was formed from the rapid reduction of diethylzinc, is quickly intercalated with phosphorus and lithium to generate the ternary. This mechanism was found to be consistent with the formation of h*-LiZnSb (Chapter 4). Following the generalization of the reaction to include various precursors, we extended to synthesis to alternative group II elements (demonstrated by the synthesis of LiCdP).

In the third chapter, we extended the generalized synthesis established in Chapter 2 to form a new polytype of LiZnSb. This phase adopts the cubic MgAgAs-type half-Heusler structure instead of the previously observed hexagonal LiGaGe-type. Motivated by this observation, we further examined the I-II-V family of structures to identify numerous other compounds that are expected to display polytypism. Additionally, c-LiZnSb was the first example of a I-II-V semiconductor having the 4c site occupied by Zn instead of the typical pnictide. Along with being interesting from a crystallographic perspective, c-LiZnSb was

calculated to be a promising thermoelectric material. In light of this new polytype being observed, we sought to better map the Li-Zn-Sb phase space.

In Chapter 4, we employed WANDA to screen the effect of reaction parameters (precursor concentrations, injection order, nucleation and growth temperatures, and reaction time) on crystalline products while keeping precursors constant (triphenylstibine, *n*-butyllithium, and diethylzinc). In total, we were able to selectively synthesize six different phases: Zn, Sb, ZnSb, Zn_8Sb_7, c-LiZnSb, and h*-LiZnSb. Most notable of these is h*-LiZnSb which adopts a previously unreported extended variant of the typical hexagonal LiGaGe-type. We identified a mechanism of formation for h*-LiZnSb by measuring phase evolution over time with PXRD, TEM, and XPS. Additionally, we found that this layered variant is less stable to heating than c-LiZnSb.

Although X-ray based techniques limit our ability to observe lithium, through the use of ssNMR, we were able to observe lithium with T_1 relaxation times consistent with being crystalline. Furthermore, ssNMR provides evidence for the existence of multiple coloring patterns within c-LiZnSb. This result is consistent with the calculations performed in Chapter 3 that placed the coloring patterns containing either zinc or antimony on the 4c site within a small energy difference. Using all of this information, we were able to construct a phase space diagram that identifies key reaction parameters responsible for different products.

The work presented in this thesis will provide a great starting point for the exploration of filled tetrahedral semiconductors from solution. Prior to this work, there was not yet an established preparation for these compounds. Some of the benefits of a soft synthesis approach to these compounds, instead of the previously utilized high-temperature routes, have already become apparent from this thesis.

I-II-V filled tetrahedral semiconductors have immense use in energy harvesting devices such as photovoltaics or thermoelectrics, as well as in energy storage. However, a critical limitation for any application is the ability to produce high performance materials at large scale. This problem can be conveniently addressed through solution processed particles. Outside of the possible applied benefits, this thesis will aid our understanding of how to synthesize complex phases that are still unknown. While considerable work has been performed with high-temperature conditions that favor thermodynamic products, a rich phase space of structures awaits to be discovered under kinetic control.